Performance Enhancement of Radiation and Scattering Properties of Circularly Polarized Antennas Using Frequency Selective Surface

Mohammad Akbari Choubar

A Thesis

in

The Department

of

Electrical and Computer Engineering

Presented in Partial Fulfilment of the Requirements

For the Degree of

Doctor of Philosophy (Electrical and Computer Engineering) at

Concordia University

Montréal, Québec, Canada

April 2018

CONCORDIA UNIVERSITY

SCHOOL OF GRADUATE STUDIES

This is to certify that the thesis prepared

By: Mohammad Akbari Choubar

Entitled: Performance Enhancement of Radiation and Scattering Properties of Circularly Polarized Antennas Using Frequency Selective Surface

and submitted in partial fulfillment of the requirements for the degree of

Doctor Of Philosophy (Electrical & Computer Engineering)

complies with the regulations of the University and meets the accepted standards with respect to originality and quality.

Signed by the final examining committee:

_____ Chair
Dr. Luis Amador

_____ External Examiner
Dr. Yahia Anter

_____ External to Program
Dr. Ali Dolatabadi

_____ Examiner
Dr. Ahmed A. Kishk

_____ Examiner
Dr. Christopher W. Trueman

_____ Thesis Supervisor
Dr. Abdel R. Sebak

Approved by _____
Dr. Wei-Ping Zhu, Graduate Program Director

Thursday, June 7, 2018 _____
Dr. Amir Asif, Dean
Faculty of Engineering and Computer Science

ABSTRACT

Performance Enhancement of Radiation and Scattering Properties of Circularly Polarized Antennas Using Frequency Selective Surface

Mohammad Akbari Choubar, Ph.D.

Concordia University, 2018

At millimetre-wave (MMW) frequencies, losses associated with wireless link and system are critical issues that need to be overcome in designing high-performance wireless systems. To compensate the overall loss in a wireless communication system, a high-gain antenna is required. Circularly polarized (CP) antennas are among preferred choices to design because they offer many advantages due to their good resistance to polarization mismatch, mitigation of multipath effects, and some phasing issues and immunity to Faraday rotation. On the other hand, frequency selective surface (FSS) technology is recently employed to enhance the performance of radiation and scattering properties of antennas used in different sectors such as aerospace, medical, and microwave industry. Therefore, it is appropriate and attractive to propose the use of FSS technology to design practical and efficient CP antennas.

CP Fabry-Perot cavity (FPC) antennas based on FSS are investigated in this thesis to fulfil the growing demand for broadband high-gain antennas with low radar cross section (RCS). The thesis investigates both characteristic improvement of CP antennas and RCS reduction issues employing FSS structures.

Initially, a high gain CP dielectric resonator (DR) antenna is proposed. Using an FSS superstrate layer, a gain enhancement of 8.5 dB is achieved. A detailed theoretical analysis along with different models are presented and used to optimize the superstrate size and the air gap height between the antenna and superstrate layer.

The second research theme focusses on developing an effective approach for mitigating the near-field coupling between four-port CP antennas in a Multiple-Input, Multiple-Output (MIMO) system. This is obtained by incorporating a two-layer transmission-type FSS superstrate based on planar crossed-dipole metal strips. Another technique for suppressing the spatially coupling

between DR antennas using a new FSS polarization-rotator wall is studied as well. The coupling reduction is achieved by embedding an FSS wall between two DRAs, which are placed in the H-plane. Utilizing this FSS wall, the TE modes of the antennas become orthogonal, which reduces the spatially coupling between the two DRAs.

The third research theme of this thesis is to enhance the purity and bandwidth of CP with the least amount of insertion loss by the use of an LP-to-CP-polarizer which is based on multilayer FSS slab. This polarizer is approximately robust under oblique illuminations. To have a high-gain CP antenna, an 8-element LP array antenna with Chebyshev tapered distribution is designed and integrated with the polarizer.

Eventually, in order to enhance the scattering property, the fourth research theme investigates on RCS reduction by the use of two different approaches which are based on FSS. Initially, a wideband FSS metasurface for RCS reduction based on a polarization conversion is proposed. To distribute the scattered EM waves and suppress the maximum bistatic RCS of the metasurface over a broad band of incident angles at both polarizations, the elements are arranged using the binary coding matrix achieved by group search optimization (GSO) algorithm. The reflective two-layer metasurface is designed in such a way to generate reflection phase difference of 180° between two elements “0” and “1” on a broad frequency band. A theoretical analysis is performed on the ratio of the “0” and “1” elements using Least Square Error (LSE) method to find the best ratio value. As the second activity of this research theme, wideband CP antenna with low RCS and high gain properties is presented. The proposed antenna is based on a combination of the FPC and sequential feeding technique.

Table of Contents

List of Tables

List of Figures

List of Abbreviations

Symbol	Definition
ACMA	Aperture-coupled microstrip antenna
ACMP	Aperture-coupled microstrip patch
ADS	Advanced design system.
AMC	Artificial magnetic conductor
BPF	Bandpass filter.
BW	Bandwidth
CP	Circularly polarization
CST	Computer Simulation Technology
CLMS	Constrained least mean square.
DRA	Dielectric resonator antenna.
DGS	Defected ground structures.
DWM	Dielectric waveguide model
EBG	Electromagnetic band-gap
FSS	Frequency selective surface
FPCA	Fabry-Perot cavity antenna
FPR	Fabry-Perot resonator
HFSS	High frequency structural simulator.
LW	Leaky-waves

LP	Linear polarization
MMW	Millimetre wave
MIMO	Multiple-input multiple output
NGMN	Next generation mobile networks
PRS	Partially reflective surface.
SIW	Substrate integrated waveguide
SLL	Side lobe level
WLAN	Wireless local area networks
LP	Linear polarization
MMW	Millimetre wave
MIMO	Multiple-input multiple output
NGMN	Next generation mobile networks
PRS	Partially reflective surface.
SIW	Substrate integrated waveguide
SLL	Side lobe level

List of Symbols

Symbol	Definition
ε_r	Relative permittivity of dielectric
σ	Electric conductivity
Zs	Surface Impedance
Ω	Ohm
Dr	Antenna Directivity
G	Antenna Gain
λ	Wavelength
λ_0	Free-Space Wavelength
η_0	Intrinsic impedance of free-space
S	S-parameter
Γ	Reflection Coefficient

Chapter 1. Introduction

Millimetre-wave and Ka-Bnad

Millimetre-wave (MMW) electromagnetic spectrum (30-300 GHz) is essential for realizing the next generation 5G wireless cellular networks and Internet-of-Things (IoT) technology. This is because this region of the electromagnetic spectrum can offer data rate transmission in order of multi-Gbit/s due to larger available bandwidth, which satisfies the huge demand for increasing system capacity, ubiquitous super-fast connectivity and seamless service delivery several. In fact, the large available bandwidth will enable 'real-time' video streaming, Internet-of-Things (IoT) and Machine-to-Machine (M2M) communications. Meanwhile, the Ka-band as a small part of MMW spectrum is ranged from 26.5 GHz to 40 GHz, i.e. wavelengths from slightly over one centimetre down to 7.5 millimetres. The 30/20 GHz band is used in communications satellites, uplink in either the 27.5 GHz and 31 GHz bands, and high-resolution, close-range targeting radars aboard military airplanes. In satellite communications, the Ka-band permits greater bandwidth communication. Lately, the wireless community has conceived the notion of 5G as a new generation of mobile wireless technology that will deliver the higher data rates up to 10 Gbps, with orders of mount further capacity and lower latency than today's wireless systems. The 5G will also partially overlap with Ka-band (28, 38, and 60 GHz). However, one of the major disadvantages of the MMW systems is high atmospheric attenuation, which reduces the range and strength of the waves. Due to its short range of about a kilometre, millimetre wave travels by line of sight, so its high-frequency wavelengths can be blocked by physical objects like buildings and trees [1]-[3]. On the other hand, due to the advanced signal propagation properties, CP technology offers significant performance benefits over traditional linear technologies, particularly in modern satellite and communication systems. The use of CP is the best solution for addressing challenges associated with adverse weather conditions, polarization mismatch, non-line-of- sight applications, phasing issues, and multipath effects [4]-[7].

Polarization of Electromagnetic (EM) Wave

The antenna polarization in a stated orientation is defined as "the polarization of the wave transmitted by the antenna. Practically, the polarization of the radiated energy changes with the

direction from the antenna centre, so that diverse sections of the pattern can have various polarizations. Polarization of a radiated wave is defined as "that property of an EM wave explaining the time-changing direction and relative magnitude of the electric-field vector; particularly, the figure traced as a function of time by the extremity of the vector at a fixed location in space, and the sense where it is traced, as observed along the direction of propagation. Polarization then is the curve traced by the end point of the arrow indicating the instantaneous electric field. The field should be seen along the propagation direction. A typical trace as a function of time is depicted in Figures 1-1 (a) and (b) [8].

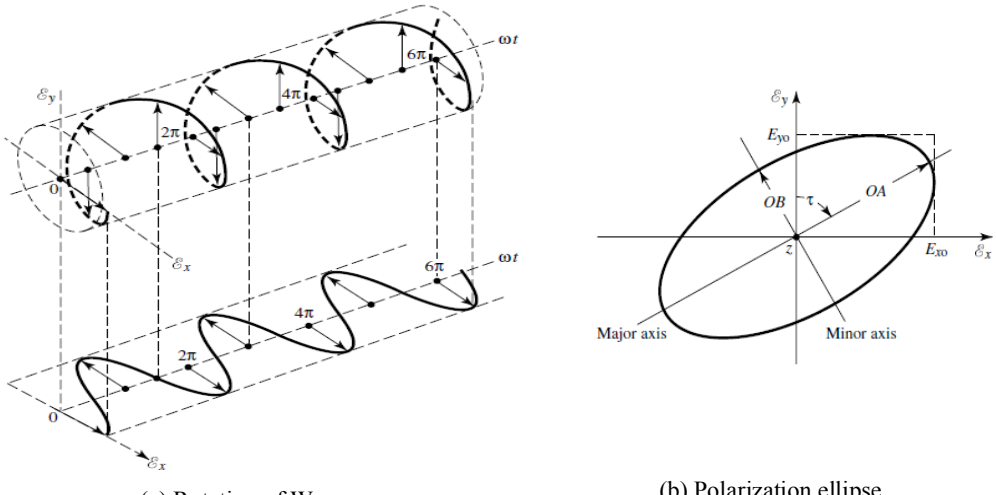

(a) Rotation of Wave

(b) Polarization ellipse

Figure 1-1: Rotation of a plane electromagnetic (EM) wave and its polarization ellipse at z = 0 as a function of time [8].

The wave polarization can be expressed in terms of a wave transmitted or received by an antenna in a particular direction at a point in the far field. Polarization is categorized as linear, circular, or elliptical. If the vector that describes the electric field at a point in space as a function of time is always directed along a line, the field is named linearly polarized (LP). Although, the figure that the electric field traces is an ellipse, and the field is called elliptically polarized (EP). Note that, linear and circular polarizations are specific cases of elliptical, and they are acquired once the ellipse becomes a straight line or a circle, respectively. The figure of the electric field is traced in a clockwise (CW) or counter-clockwise (CCW) sense. Clockwise rotation of the electric-field

vector is also designated as right-hand polarization and counter-clockwise as left-hand polarization [8].

1.1.1 Linear, Circular, and Elliptical Polarizations

The instantaneous field of a plane wave, traveling in the negative z direction, can be written as

$$\vec{E}(z,t) = E_x(z,t)\hat{x} + E_y(z,t)\hat{y} \tag{1-1}$$

The instantaneous components are related to their complex counterparts by

$$E_x(z,t) = E_{xo}\cos(\omega t + kz + \phi_x) \tag{1-2}$$

$$E_y(z,t) = E_{yo}\cos(\omega t + kz + \phi_y) \tag{1-3}$$

In which E_{xo} and E_{yo} are, respectively, the maximum magnitudes of the x and y components.

• Linear Polarization

For the wave to have linear polarization, the time-phase difference between the two components must be

$$\Delta\varphi = \varphi_y - \varphi_x = n\pi, \qquad \text{n=0, 1, 2, ...} \tag{1-4}$$

• Circular Polarization

Circular polarization can be achieved only when the magnitudes of the two components are the same and the time-phase difference between them is odd multiples of π/2. That is,

$$|E_x| = |E_y| \Rightarrow E_{x0} = E_{y0} \tag{1-5}$$

$$\Delta\varphi = \varphi_y - \varphi_x = \begin{cases} +(\frac{1}{2} + 2n)\pi, & \text{n = 0,1,2,... for CW} \\ -(\frac{1}{2} + 2n)\pi, & \text{n = 0,1,2,... for CCW} \end{cases} \tag{1-6}$$

If the direction of wave propagation is reversed (i.e., +z direction), the phases in (2-60) and (2-61) for CW and CCW rotation must be interchanged.

• Elliptical Polarization

Elliptical polarization can be attained only when the time-phase difference between the two components is odd multiples of π/2 and their magnitudes are not the same or when the time-phase difference between the two components is not equal to multiples of π/2 (irrespective of their magnitudes). That is,

$$\left|E_x\right| \neq \left|E_y\right| \Rightarrow E_{x0} \neq E_{y0} \tag{1-5}$$

$$\Delta\varphi = \varphi_y - \varphi_x \neq \pm\frac{n\pi}{2}, \mathrm{n} = 0,1,2,... \tag{1-6}$$

To summarize, a time-harmonic wave is circularly polarized at a given point in space if the electric (or magnetic) field vector at that point traces a circle as a function of time. The necessary and sufficient conditions to accomplish this are if the field vector (electric or magnetic) possesses all of the following:

a. The field must have two orthogonal linear components and

b. The two components must have the same magnitude and

c. The two components must have a time-phase difference of odd multiples of 90◦.

The rotation sense is always examined by rotating the phase-leading component toward the phase-lagging component and observing the field rotation as the wave is viewed as it travels away from the observer. If the rotation is clockwise, the wave is right-hand (or clockwise) circularly polarized; if the rotation is counter clockwise, the wave is left-hand (or counter clockwise) circularly polarized.

1.1.2 Advantages of Circular Polarization

A. Immunity to Faraday rotation

Faraday rotation happens once an LP signal passes through the ionosphere. When the EM wave interacts with the charged particles and the Earth's magnetic field, its plane of polarization is rotated. The rotation is proportional to the magnetic flux density in the propagation path and it is further problematic in higher sections of the atmosphere because of stronger magnetic fields

produced by highly ionized plasma [9]. The magnitude of the effect varies since the density of electrons in the ionosphere changes greatly on a daily basis. Although, the rotation amount of the polarization angles is always inversely proportional to the square of the frequency. Consequently, there is a polarization mismatch for LP antennas. On the other hand, CP is immune as it has two equal orthogonal components and any rotation will be on both components, in the same manner, hence, the wave will still be CP.

B. Mitigation of multipath propagation

Multi-path is caused when the primary signal and the reflected signal reach a receiver at nearly the same time. This creates an "out of phase" problem. The receiving radio must spend its resources to distinguish, sort out, and process the proper signal, thus degrading performance and speed. Linear Polarized antennas are more susceptible to multi-path due to increased possibility of reflection.

C. Polarization mismatch loss

The polarization mismatch happens because of misalignment of the transmit and receive antennas. For LP antennas, the transmit and receive antennas must be aligned to avoid polarization losses. However, a CP antenna receive an LP wave whatever its orientation is [10]. This is because a CP wave propagates in both horizontal and vertical planes and the planes in between so for an arbitrarily oriented LP antenna, there will always be a component of the CP wave that will be aligned with it.

Periodic Structures

The periodic structure is considered as a traditional concept in the EM field of investigation. The periodicity of the structure adds some features for the propagation inside. Furthermore, utilizing the periodicity of the structure to achieve some requirements in the device itself is a well-known procedure in microwaves (see Figure 1-2).

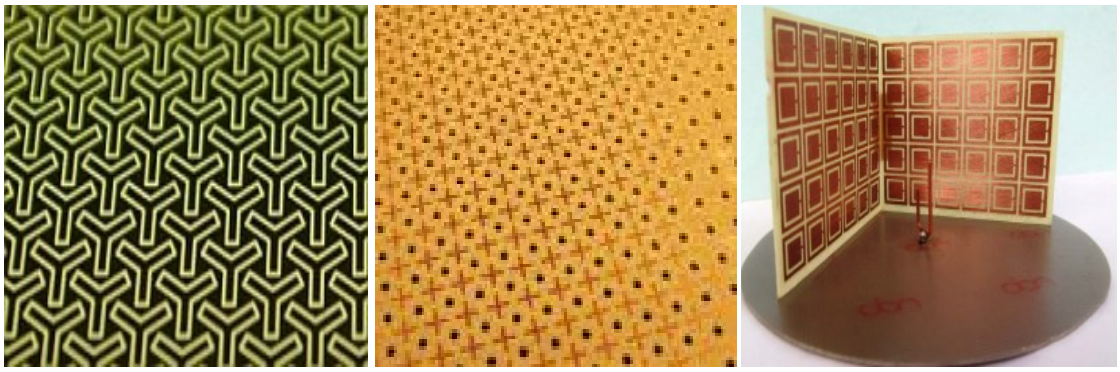

Figure 1-2: Shematic of different periodic stuctures

One of the most famous examples is frequency selective surface (FSS) which functions as a frequency filter. There are many applications based on the concept of periodic structures. Some of the periodic structures are given a special name based on their configuration, behaviour or basic operation. In the next chapter, a literature review and basic principles governing the operation and analysis of frequency selective surfaces (FSS) will be provided. A brief history along with an overview of the FSS basic characteristics and the different types of element shapes will be shown as well.

Motivation

One basic component in any communication system is the antenna, which is governing the characteristics of the communication transponder. Recently, there have been enormous research and development in antenna design and optimization.

The Ka-band as a small part of MMW spectrum is ranged from 26.5 GHz to 40 GHz. Recently, the wireless community has conceived the notion of 5G, a new generation of mobile wireless technology that will deliver the higher data rates up to 10 Gbps, with orders of magnitude further capacity and lower latency than today's wireless systems. Although, one of the main drawbacks of the MMW is high atmospheric attenuation, which limits the range and strength of the waves. In order to enhance the total sensitivity and signal-noise ratio in systems, antenna designers are currently interested in designing highly gain antennas [11]-[12].

On the other hand, polarization is one of the fundamental characteristics and critical issues in wireless communication systems. Recently, because of the advanced signal propagation properties, systems using CP antennas offer considerable performance advantages over systems utilizing traditional LP antennas, particularly in modern satellite and communication systems. The use of CP is considered as a solution for addressing challenges associated with polarization mismatch, none-line-of- sight applications, phasing issues, and multipath effects [8]-[10].

Frequency selective surface (FSS) technology has many applications in various sectors such as aerospace, medical, and microwave industries. One of the practical applications of FSS is in aerospace industries, where FSS is mainly employed to enhance the performance and suppress the radar cross section (RCS) of different devices such as radom, reflector antennas, microwave circuits, etc.

Consequently, to fulfil the growing demand for the broadband high-gain antenna with low radar cross section (RCS), CP Fabry-Perot cavity (FPC) antenna based on FSS is found to be an appropriate choice. Furthermore, rigorous designs of FPC antennas always involve challenging procedures; especially where high performance of radiation and low RCS are expected from both the antenna and FSS superstrate. The lack of accurate and realistic modelling of FPC antennas while enhancing both properties of radiation and RCS reduction are yet a missing key point in the FPC antennas. In addition, there are series drawbacks such as narrow bandwidth, low purity in axial ratio and radiation efficiency, and large size. In other words, to the author's best knowledge, as compared with previously published works in the open literature, it is not observed yet an FPC antenna satisfying all requirements of broadband CP, impedance matching, low RCS, high gain and small profile (one-layer metasurface), simultaneously. Ultimately, the idea of using FPC to enhance gain, suppress RCS, generate and conserve CP feature, and expand bandwidth is of great research potential. Therefore, different antenna designs with FSS layer can be exploited to satisfy the above-mentioned conditions.

Objective

The focus in this thesis is based on four major aspects that assist to adequately characterize and design the antennas along with FSS layer. These aspects are:

- Providing an accurate modelling scheme to the Fabry-Perot Cavity (FPC) antennas for estimating the superstrate size and air gap and also to address the main drawback of FPC antennas, with expanding the 3-dB gain bandwidth using effective medium method.
- Suppressing spatially coupling in multiple-input multiple output (MIMO) antenna using FSS layers.
- Enhancing the CP purity and bandwidth with the least amount of insertion loss employing multilayer FSS slab.
- In order to enhance scattering property, two approaches for reducing RCS based on FSS are proposed.

For each one of above sections, different approaches and designs will be presented, eventually, the purpose of this thesis is to design a wideband CP antenna with properties low RCS and high gain, simultaneously.

Thesis Outline

This thesis is organized into seven chapters including this introduction chapter as follows.

Chapter 2 provides a literature review and basic principles governing the operation and analysis of FSS. This contains a primary discussion, and brief history and background along with different practical applications.

In chapter 3, in order to enhance the antenna gain, two different FPC antennas base on FSS are designed. The goal of this chapter is to enhance gain and expand the 3-dB gain bandwidth at the same time. To reach these, a few accurate modelling schemes such as transmission line circuit model, diffraction and transmission rays, and effective medium method will be presented.

In chapter 4, two effective approaches for mitigating the near-field coupling between adjacent antennas are suggested. These approaches are based on FSS metasurface.

In chapter 5, in order to enhance the purity and bandwidth of CP with the least amount of insertion loss, one LP-to-CP polarizer is introduced which based on multilayer FSS slabs. To have a high-gain CP antenna, an 8-element LP array antenna with Chebyshev tapered distribution is designed and integrated with the polarizer.

Chapter 6 presents two different methods to reduce RCS including coding FSS metasurface using group search optimization (GSO) algorithm and the combination of the FPC and sequential feeding technique.

Chapter 7 concludes the thesis with suggested future work.

Moreover, this thesis presents one additional appendix including details about group search optimization (GSO) algorithm.

Chapter 2. Literature Review

Frequency Selective Surface (FSS)

This section provides a literature review on basic principles governing the operation and analysis of frequency selective surfaces (FSS). This contains a primary discussion on brief history and background along with different practical applications. A short overview of the FSS basic characteristics with the different types of element shapes are presented, as well.

2.1.1 FSS Background and Applications

Filters play a fundamental role in most electronic or RF circuits. Once being incorporated into a design, the filter acts as a device that controls the frequency content of the signal for mitigating noise and unwanted interference. Once exposed to the electromagnetic radiation, an FSS acts like a spatial filter; some frequency bands are transmitted and some are reflected. In such a way, an FSS can be a cover for hiding communication facilities. This is probably the first potential application of FSS structures, as they have actually been used as covers named radomes. Radomes are band-pass FSS filters that are used to reduce the radar cross-section (RCS) of an antenna system. Since the early 1960's, because of potential military applications, FSS structures have been the subject of intensive study [13-15]. Marconi and Franklin, however, are believed, [13] to be the early pioneers in this area for their contribution of a parabolic reflector made using half-wavelength wire sections in 1919 [16]. FSS is now employed in radomes, missiles, and electromagnetic shielding applications. FSSs as frequency-selective materials have been used traditionally in stealth technology for reducing the RCS of communications systems. The concept of stealth or being able to operate without the knowledge of the enemy has always been a goal of military technology. In order to minimize the detection, FSS layers cover the facilities to reduce the RCS. FSSs most commonly take the form of planar, periodic metal-dielectric arrays in two- dimensional space. Frequency behaviour of an FSS is entirely determined by the geometry of the surface in one period (unit cell) provided that the surface size is infinite. Although taking different shapes, conventional FSSs have similar operation mechanisms that can be explained by the phenomenon of resonance. Consider an array of elements on a planar surface. Upon contact with a plane-wave, the elements of the periodic surface resonate at

frequencies where the effective length of the elements is a multiple of the resonance length, λ/2 [14]. Corresponding to the phase front of the wave, these elements have a certain phase delay. As a result, the scattered radiations of individual elements add up coherently. An example of such arrangement of elements is Marconi and Franklin's reflector. This reflector is very much similar to the most famous FSS design, an array of half-wave dipoles. The resonance characteristics of an FSS usually depend on the way the surface is exposed to the EM wave. Another practical application of FSS is related to secure buildings [17], as shown in Figure 2-1. A collaborative project to design FSS for wireless propagation control within buildings between the Universities of Kent and Manchester in the UK and Auckland in New Zealand has been done. The rationale for the project was to find solutions to the pervasive problems of spectral overcrowding, interference, and security while at the same time allowing the emergency services to use their radio systems (TETRA in Europe) when they need to enter a building [18]. In addition, FSS building structures can also be three-dimensional wallboard-based structures, as suggested in a research conducted by Ofcom [19]-[20] which offer greater selectivity and performance than their two-dimensional wall paper like counterparts. Furthermore, the signal isolation capability of a small FSS screened enclosure has been studied in [21].

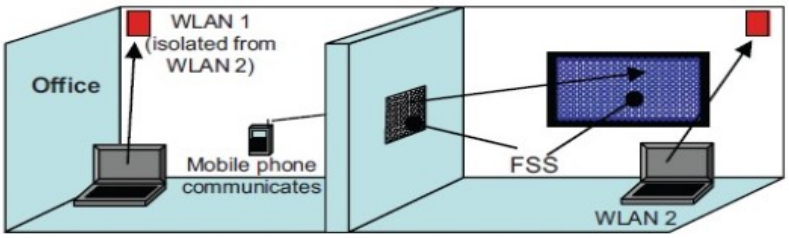

(a) A civil office environment

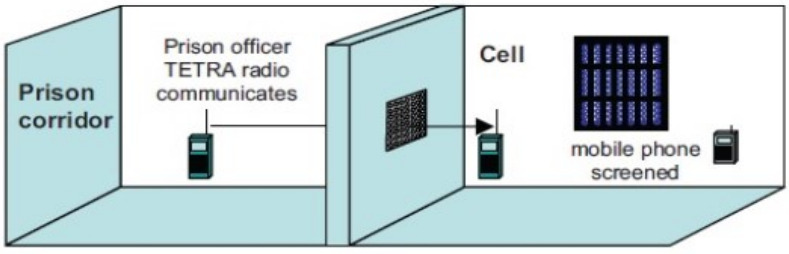

(b) A prison building

Figure 2-1: Example of finite FSS panel usage in different scenarios. In both cases it is assumed that the surrounding walls, floors, and ceilings are screened with thermally insulating metal sheeting [17].

There are other practical examples which have already beeing done and presented in the literature for further security (see Figure 2-2) [22]. It is observed that FSS walls can be applied in conference rooms and investigate areas such as the library to have more isolation.

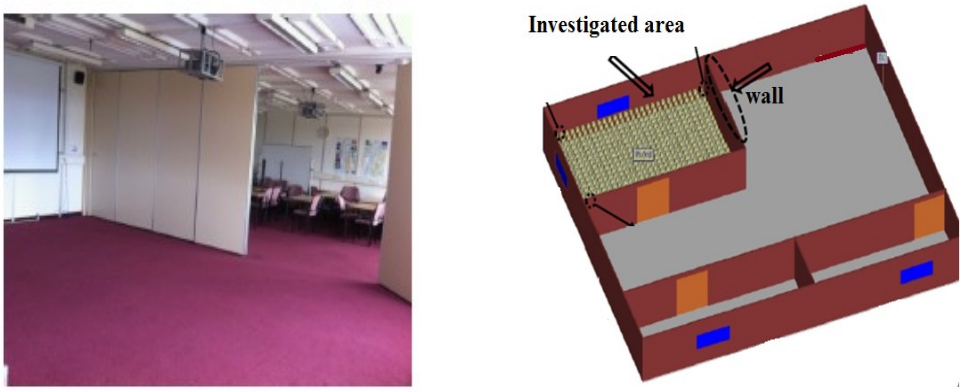

(a) FSS wall inside conference Room **(b) Investigated area surrounded by FSS wall**

Figure 2-2: Examples of finite FSS walls used in (a) conference room and (b) investigated room [22].

One of other practical application of FSS is used as low emittance windows, as shown in Figure 2-3 [23]. The standard type of window pane is made of non-magnetic glass with a typical conductivity of $\sigma = 10^{-12}$ S/m, a relative permittivity $\varepsilon r \simeq 4$, and a thickness of $d \simeq 4$ mm. The pane presents no major obstacles to microwave radio propagation since it is thin compared to the wavelength and its conductivity is extremely small. The panes are transparent for more or less all radiation with frequencies below UV light [23]. Thus a window pane is a transparent to visible light (390 to 770 nm), infrared (IR) light (770 to 2100 nm) as well as microwaves. The transparency of IR light is during summer and winter unfavourable. By using energy saving windows, one can improve thermal response leading to an economically viable solution. One drawback with these energy saving windows is the degrading of the radio channel properties [23].

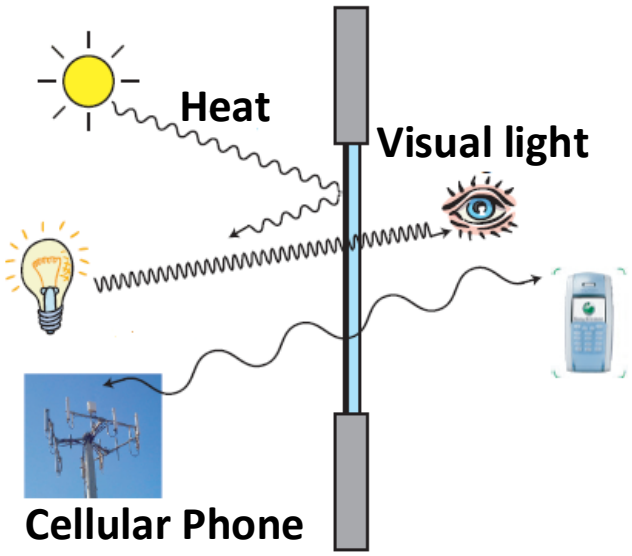

Figure 2-3: Illustration of a frequency selective window. The infrared radiation (heat) is blocked by the window, but the indoor outdoor communication is possible. The visible part of the spectrum remains unchanged [23].

2.1.2 FSS Overview

FSSs are planar periodic structures which show reflection and/or transmission features as a function of frequency. The surface consists of thin conducting elements, usually printed on dielectric substrates for support. In general, the FSS structures can be divided into patch-type or aperture-type metallic elements, being periodic in either a one or two-dimensional array. FSS behaviour can be divided into four frequency response types: low pass, high pass, band pass and band stop as shown in Figure 2-4. The low pass FSS and the high pass FSS are complementary surfaces in the sense that they together cover the entire surface. According to Babinet's principle, the transmission and reflection coefficients of one surface will be the reflection and transmission coefficients of the other. That implies that a high pass FSS is obtained from a low-pass FSS by exchanging the conductive parts with the non-conductive parts. This applies also to the band-pass FSS and band-stop FSS. However, the surface must meet certain requirements. Initially, screen thickness should be less than 1/1000λ (infinitely thin) and there should be no dielectric layer. When a layer of dielectric is added to a metallic FSS, the resonant frequency decreases. Figure 2-4 (a), depicts a periodic array of conducting elements (gray squares) that attains a low-pass characteristic.

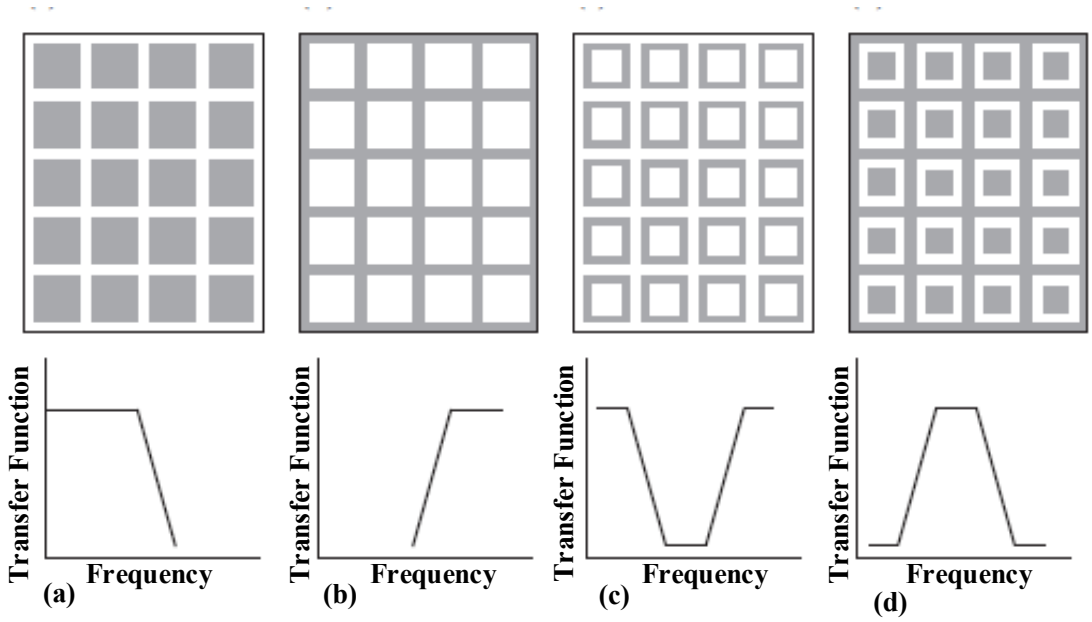

Figure 2-4: Typical FSS types and their responses. The gray surface represents a metallic surface. (a) array of metallic patches and respective low pass behavior, (b)apertures on the conductive medium and ideally high pass transfer function. Figures (c) and (d) show the loop elements that have resonant characteristics (c) metallic loop and (d) aperture loop.

By using Babinet's principle, the characteristic in Figure 2-4 (b) is obtained by simply reversing the materials. Using the same principle, the band-pass filter is shown in Figure 2-4 (d) has a structure that is the complement of the structure for the band-stop filter in Figure 2-4 (c).

2.1.3 Types of FSS

There are many types of FSS elements with each shape having its unique transmission / reflection characteristics, sensitivity to oblique angle of incidence, polarization type, and bandwidth. FSS arrays are grouped into 4 classified according to [13]:

2.1.3.1 Centre connected or n-poles

Centre connected elements including simple straight element such as dipoles, Cross dipoles [24], unloaded tripoles, anchor elements, and Jerusalem cross, as shown in Figure 2-5 (a).

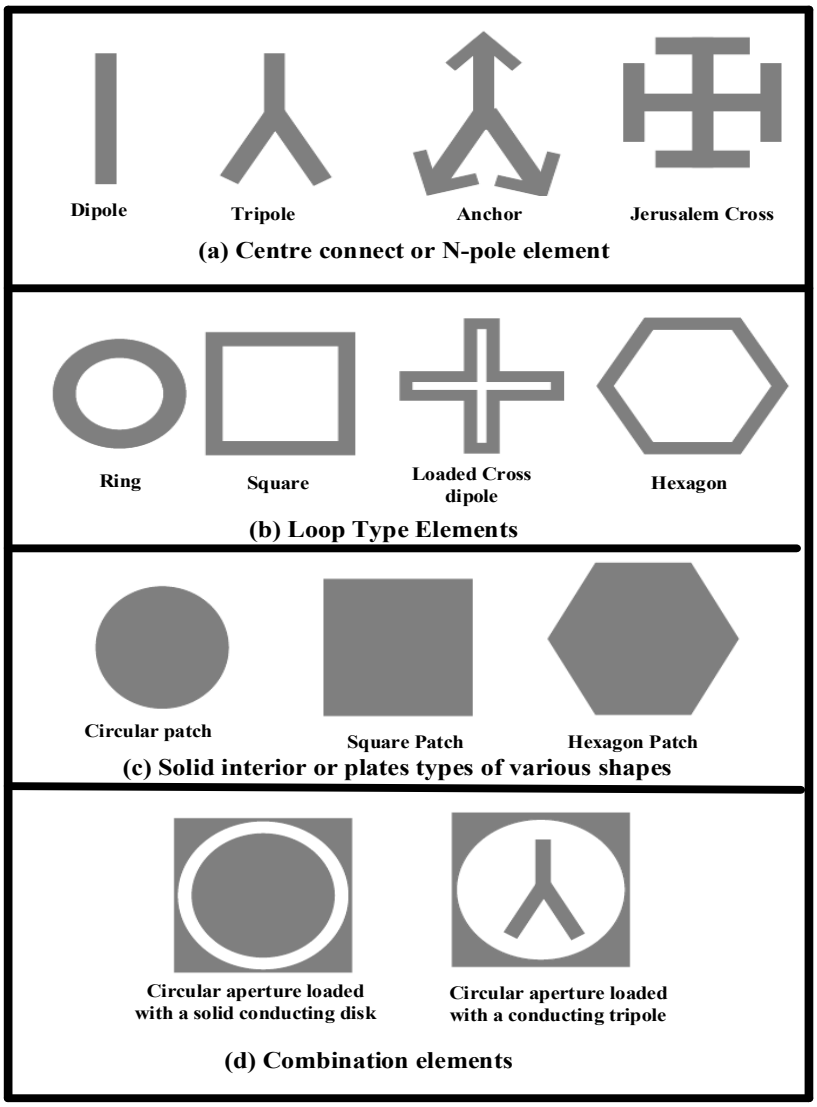

Figure 2-5: Common FSS element types [29], [30].

2.1.3.2 Loop Type Elements

The most common loop elements are the square [25] and circular loops (rings) [26], [27], as well as three and four-legged loaded elements, as shown in Figure 2-5 (b).

2.1.3.3 Solid interior or plate elements of various shapes

This group includes simple squares, and hexagonal and circular conducting plates [28], as shown in Figure 2-5 (c) and (d).

2.1.3.4 Combination Elements

In this group, various combinations of elements are possible in order to take advantage of specific characteristics in order to enhance, for example, the array frequency response, independencies to oblique incidence, reflection bandwidth, or lowering the resonant frequency. The dipole elements are shown in Figure 2-5 (a), are singly polarized structures, while dual polarised structures can be created with, for example, cross dipoles. The unloaded tripole arrays have very good dual polarisation and they can be packed tightly. However, the anchor elements have greater bandwidth and out of band grating response due to the end capacitance [13], [14], [24].

Antenna Gain Enhancement by FSS Layer

Highly-efficient high-gain antennas have been at the centre of interest for various millimetre-wave (MMW) wireless applications. Parabolic reflector and array antennas are known as strong candidates aiming for high-gain radiation, at such high frequencies, accompanying their advantages and disadvantages for the desired application. For example, reflector antennas are bulky and in a need of mechanical motors for beam steering applications. Array antennas can be planar structures with the capability of beam steering using an optimized phase distribution over the array elements; however, this type of antenna suffers from structural losses due to its feeding network/circuitry (especially for high-gain arrays which require a large number of elements). On the other hand, planar FPC antennas are also known for their ability to produce highly-efficient directive radiation pattern using a single excitation point, as shown in previous works [31]-[48]. These cavities are formed by placing a partially-reflective surface (PRS) on top of a ground plane [31]-[48]. Reviews of FPC antennas can be found in [38]-[39]. These antennas have been designed using various types of PRS superstrates made of periodic metallic patches or slots [40]-[42], single-layer [32] or multilayer dielectric slab superstrates [43]-[44]. In various detailed studies, as in [45]-[46], the radiation behaviour of these antennas was studied through excited leaky-waves (LW) inside these cavities similar to that of a general LW antenna as well described by Tamir [47] and Oliner [48]. The radiation behaviour of these antennas relies on the excitation of leaky-waves (LW) inside the cavity [45]-[46]. Based on LW explanation [45]-[46], a high-gain FPC antenna produces a broadside directive radiation beam (i.e. a pencil beam),

perpendicular to the antenna plane (or FSS and ground plane), in the proximity of its resonance frequency. For frequencies larger than the resonance frequency of the cavity, the beam starts opening in the middle and steers to the sides of the antenna. For a highly reflective inductive or capacitive FSS, slight changes in the resonance height of the cavity (e.g. either by using a mechanical displacement or slight change in the relative permittivity of the material inside the cavity) can steer the main beam of the antenna around its centre frequency. One of the main constraints of such cavities is their 3dB gain/power bandwidth so that FPC antennas are resonance based that is why those suffer from the limited bandwidth. The lack of a theoretical model to estimate the FSS layer size is considered as other imperfection in FPC antenna‘s vicinity. Therefore, in this thesis, finding the alternative to address these drawbacks has been main contribution in this research area.

Coupling Reduction between Antennas by FSS Layer

Mutual coupling refers to the interactions between electromagnetic (EM) fields of the adjacent antenna elements. It can degrade the antenna array performance in terms of impedance and radiation characteristics [70]. Depending on the shape of antennas (i.e., planar or nonplanar), fabrication technologies, arrangement type, and distance between them, mutual couplings are categorized as follows: (i) the signal leakage via surface wave propagating along substrate dielectric and air interface [71], [72], (ii) the conducting current due to the existence of continuous metallic ground plane [73], (iii) the mutual coupling between the feeding lines [74], and (iv) the coupling due to the spatial electromagnetic fields [75]. Multiple-input multiple output (MIMO) systems in millimetre-wave (MMW) frequency band have become an emerging technology for future indoor and outdoor communications because they permit the next generation mobile networks (NGMN) to provide high data rates in order to improve the link performance [76]. Improvement in throughput and radiation efficiency of MIMO wireless systems demands a lower envelope correlation and further degree of isolation between the adjacent antennas [77]. Therefore, mutual coupling reduction between closely spaced antennas in MIMO systems has been studied by various authors [78]–[79]. Mutual coupling affects the MIMO system performance through varying the impedance and radiation characteristics, which degrades the side-lobe level and radiation pattern shape [80]. In order to increase the signal-to-

noise ratio and enhance the channel capacity of MIMO systems, the inter-element spacing should be minimum (a half wavelength) [80]. However, the space left for antenna elements and fabrication restrictions are usually heavily restricted in the highly integrated wireless communication systems. One should note that such a limited inter-element spacing results in a strong mutual coupling, radiation efficiency reduction, and functional deterioration of the system [75]. Isolation approaches are extensively reported in the literature to reduce mutual coupling effects [71]-[89]. Lumped elements connected in shunt are adjusted to decouple the isolation between two adjacent patch antennas [80]-[81]. At low-frequency 2.45 GHz, a new narrow-band decoupling technique has been proposed with a considerable compact decoupling network [80]. It is an effective technique for coupling reduction but typically results in a narrow-band behaviour and is considered as a complex structure to be utilized in antenna arrays. In a dielectric substrate, the parasitic cross coupling is achieved by surface modes and further improved when high permittivity and thick substrate are utilized. As a result, electromagnetic band-gap (EBG) structures are formed to prevent the surface-waves propagation toward the next antenna at the bandgap frequencies [78], [82]-[83]. Changing the radiation pattern and the occupied space by EBG are major drawbacks of these structures. Defected ground structures (DGS) methods by means of various slots etched off metallic background to increase isolation were presented in [84]-[85]. The disadvantage of DGS is related to a backward signal leakage. Eigen-mode decomposition approach is utilized based on a 180° coupler [86]. Decoupling networks based on coupled resonators in array structures was studied [87]. These resonators are able to produce high-order resonance and broadband coupling reduction solution. However, both the Eigen-mode and decoupling network structures are inconvenient using complex structures [87]. A coplanar strip wall between two antennas was reported in [89]. However, such a technique deteriorates the antenna's radiation pattern. This is because of the fact that the coplanar strip wall is not matched. Metamaterials have been widely analysed in the recent years to improve many antenna radiation characteristics due to their unusual electromagnetic properties [90]-[91]. In order to suppress the mutual coupling of the spatial electromagnetic fields, improving at the same time, the radiation performance of the antennas, metasurface, and frequency selective surface (FSS) as the superstrate of the antennas were proposed [75], [92]-[94]. Note that, depending on the antenna's radiation pattern shape, the spatially mutual coupling is generated in near-field area. However, the decoupling designs operate on the basis of coupling reduction of either E or H-Fields

between linearly polarized (LP) antennas. Recently, due to factors such as polarization mismatch, multipath phenomenon, and phasing subjects, the trend to design the circularly polarized (CP) antennas is expanding [4], [66]. As mentioned before, the most of the studies in the literature apply the similar principle to reduce the coupling among LP antennas. In [92]-[93] a new technique has been observed based on metasurface layer on the top of MIMO planar dipoles with the inter-element spacing 0.3 λ and 0.5 λ. However, it functions for linear structures and also the coupling reduction is not tangible, so that the improvement of 3dB and between 8 to 14 dB in different cases in the orientation of H-plane is obtained, whilst in the E-plane coupling is not significant as compared with the air coupling (without superstrate).

In this thesis, two different approaches which based on FSS layer are presented. Initially, coupling reduction behaviour on MIMO-CP antenna systems based on a two-layer transmission-type FSS is investigated. Correspondingly, the FSS layers transmit the large proportion of incident EM wave on the preferable frequency band. Therefore, the antenna's radiation pattern is slightly concentrated upward, ending up a spatially mutual coupling reduction between the antennas. However, due to this fact that each FSS element with different phases is illuminated, insignificant reflections are scattered from the FSS layers which is considered as the main drawback of this approach. To solve this drawback, considering the FSS layers as a uniform planar array, the authors have determined the near-field behaviour of FSS layers on the backside toward the radiating antennas. It is realized that by tuning few design parameters, the phase of reflections can be controlled. As a result, the insignificant reflections can easily be redirected along the nulls and away from the radiating antennas to prevent any interference.

In this thesis for suppressing the spatially coupling between DR antennas, another technique using a new FSS polarization-rotator wall is studied as well. The coupling reduction is achieved by embedding an FSS wall between two DRAs, which are placed in the H-plane. Utilizing this FSS wall, the TE modes of the antennas become orthogonal, which reduces the spatially coupling between the two DRAs. The proposed FSS wall approximately has no influence on the DRA characteristics with respect to input impedance and radiation pattern. The radiation pattern is approximately unchanged as compared with a DRA MIMO antenna array without FSS wall.

Enhancing the CP Bandwidth and Purity Using an FSS-type Polarizer

Polarization properties play a critical role in wireless communication systems. Recently, due to the advanced signal propagation properties, systems using CP antennas offer significant performance benefits over systems using traditional LP antennas. The use of CP is considered as a solution for addressing challenges associated with adverse weather conditions, and polarization mismatch, none-line-of- sight applications, phasing issues, and multipath effects [4], [8-10]. Various CP antennas have been presented in the literature in the last few decades. An appropriate way of creating a CP wave is to radiate an LP wave to a polarizer plane. This method has become attractive in situations where the radiating structure contains a planar array. For this case, the polarizer is placed on top of the antenna to transmit CP waves. Basically, the polarization converter decomposes the LP incident plane wave into two orthogonal components of nearly equal amplitude with a phase difference of 90° to generate a CP transmitted plane wave. A transmission-type polarizer have been extensively investigated by researchers in the open literature for several applications [102-111]. For example, some polarizers were designed utilizing FSS structures [102-105], and others are based on traditional hybrid meander line and loop configuration [106-108]. In [102] a multilayer FSS was designed using square patches with truncated corners to obtain 90° phase difference between orthogonal linear components. The polarizer presented in [103] employs a miniaturized-element FSS composed of arrays of subwavelength capacitive patches and inductive wire grids separated by dielectric substrates. The polarizer in [104] uses a double-sided partially reflective surface (PRS), which controls independently the reflection and transmission coefficients. The work in [105] suggests a CP converter utilizing a four-layer FSS consists of split rings bisected by a metal strip, in which distance between different layers is a quarter wavelength, but the layers' dimensions are different. Despite structures suggested in [102-105] are broadband, they consist of multilayer structures with different configurations and dimensions for each layer, ending up with complicated geometry and configuration for the polarizers. In [107] single layer polarizer based on hybrid meander line and loop geometry are proposed. This structure can cover the AR bandwidth of 46.8%. However, the peak insertion loss is 3dB. In order to achieve a CP in [108], a meander line polarizer has been employed with the linear SIW antenna, while the structure does not have broadband behaviour. Another approach used in [109] included rotating FSS structure that was implemented using the substrate integrated waveguide (SIW) technology. The

rotating FSS in [110] utilizing a triple-mode SIW cavity resonator resulted in improving the transmission bandwidth. Meta-surface and metamaterial have been applied in [110]-[111]. A meta-surface of 16 rectangular loop unit cells each with a diagonal microstrip line is positioned above a source antenna in [110]. An ultra-compact chiral metamaterial (CMM) using triple-layer twisted split-ring resonators (TSRRs) structure was suggested in [111]. Despite the benefits proposed by these designs, the majority of them employ resonant elements that tend to be narrowband.

In this thesis, a Ka-band transmission–type polarizer based on multilayer FSS slab to transform LP incident EM wave into a CP transmitted wave is proposed. To simplify the structure, a unit cell is used in all dielectric layers. In addition, in order to illuminate the polarizer, an 8-element LP array antenna with Chebyshev tapered distribution to control the radiated pattern side lobe level (SLL) is also designed. In the configuration, the antenna is placed at a half free space wavelength from the polarizer with a 45° rotation. The size of the polarizer is determined using a diffraction and transmission rays' model. The benefits of the proposed structure include wide CP bandwidth, high CP purity, robust under broad-angle oblique incident waves, the least amount of insertion loss, and design simplicity using same unit cell in all layers.

RCS Reduction to Enhance Scattering Property

In the past decade, FSSs have received substantial attention in wireless communication systems so that researchers have dedicated extensive efforts to investigation community due to their potential applications in the commercial and industrial sectors [126]. FSSs are typically periodic (2-D) array structures of suitably arranged metal patches or apertures that function as band-stop or band-pass spatial filters depending on the features of associated the unit cells [127-128]. They have been extensively employed in many areas, such as electromagnetic capability [129-130], polarizers [131], high gain antennas [66], absorbers [132], and radar cross section (RCS) reduction [133]. Broadband RCS and manipulating the characteristics of scattered electromagnetic (EM) fields, have always been challenging objectives to designers [134]. Simultaneously, easy integration of FSSs with objects is another critical design issue [135]. Various traditional methods have been suggested in the literature to redirect the scattered waves away from the backscatter direction. They relied on loading the object with radar absorbing

materials (RAM) and/or passive or active cancellation [136]. The principal benefits of employing RAM are convenience, efficiency, and flexibility at the expense of overall thickness [134]. However, this technique increases the weight and air drag. In addition, the ground plane with RAM is angle and frequency sensitive and as such it is a narrow frequency band [134-137]. Another technique is to shape the target geometry [138] as an effective alternative approach. However, this technique increases the design complexity in terms of the engineering aspects of the vehicle. In addition, it only functions well at high frequencies with potential adverse effects at low frequencies [134-137]. Another approach of achieving RCS reduction is based on a combination of perfect electric conductors (PEC) and artificial magnetic conductors (AMC) in a chess board [139]. The low profile and simple planar structure are the major advantages of this configuration. In this structure, AMC unit cells produce a 0° phase difference to the scattered waves whilst PEC reflects incident waves with a 180° phase difference. Using the contribution of the PEC and AMC cells, a 180° phase difference is obtained, resulting in destructive interference and creating a null in the specular angle [135-139]. The main drawback of the approach reported in [138] is the narrowband behavior of the AMC cells so that the chess board provides a 10-dB RCS reduction (normalized to a PEC surface) over a bandwidth of nearly 5%. In [135], two Jerusalem Cross AMCs with different sizes were applied. The chess board that combines two kinds of AMC is able to obtain a realized bandwidth of nearly 40%. Simulated results of RCS using chess board showed approximately 58% bandwidth for normal incidence but no experimental results were reported [140]. In [141] by modifying the blended checkerboard design, the 10-dB, RCS reduction covered 91% fractional bandwidth. It is clear that bandwidth expansion is still one of particular interests. On the other hand, polarization is the main feature of EM waves, and researchers have made considerable efforts to manipulate it. Recently, structures for RCS reduction that rely on the principle of polarization conversion have been presented in the literature [142-144]. However, the narrow bandwidth has restricted the practical application of the polarization converters. For example, reference [142] has suggested a polarization conversion metasurface (PCM) based on fishbone-shaped arrays that produces some separate narrow bands. In [143] a polarization rotation reflective surface (PRRS) is presented. It is based on connecting a square patch with the ground using two non-symmetric vias. A 49% bandwidth is obtained. In [144] a rotator is suggested which it can carry out 90° polarization rotation at

three frequencies and maintains a 56% polarization conversion efficiency. It is obvious that bandwidth extension of these kinds of designs is still in need of further critical studies.

In this thesis, in order to reduce RCS two different designs will be presented. Initially, a super-wideband reflective metasurface for both monostatic and bistatic RCS suppression with different incident angles is presented. The design consists of a two-layer substrate with the identical material and thickness. The main metasurface is arranged by the binary elements “0” and “1”. Each of the Elements is composed of 4×4 FSS cells. The elements are formed by the binary coding matrix to distribute the scattered EM waves and reduce the maximum bistatic RCS of the metasurface over a wide band of incident angles at both polarizations. In order to achieve the binary coding matrix, group search optimization (GSO) algorithm is employed. The element arrangement on metasurface leads to a significant RCS reduction on frequency range from 5.1 GHz to 22.1 GHz (approximately 125%) at normal incidence for both polarizations. Meanwhile, a theoretical analysis is performed on the ratio of the “0” and “1” elements using Least Square Error (LSE) method to find the best ratio value so that the optimum value of the ratio as a new constraint is added to GSO algorithm to attain a new coding matrix in another process of the optimization algorithm. As the second act of this part, a wideband CP antenna with low RCS and high gain properties is presented. The proposed antenna is based on a combination of the FPC and sequential feeding technique. The purpose of this antenna is to produce CP with the high directive level on wide bandwidth preserving low RCS.

Chapter 3. Gain Enhancement of CP Antenna Based on FSS

Introduction

Next generation of wireless systems needs broader bandwidths, higher speeds, and lower latency. As such, designers of fifth generation (5G) systems are seeking to use the MMW bands. In addition, the 5G systems look for high-gain and wideband antennas operating in the MMW band. One challenge of the MMW is the high free-space path loss. Thus, some designs have been proposed to address the radiation characteristics at MMW [31]-[48]. One method to enhance the radiation characteristics (3-dB gain bandwidth) of antennas is applying a FPC approach in which an FSS superstrate or partially reflective surface (PRS) is embedded at approximately a half wavelength from a metallic ground plane, this generates an air-filled cavity. By illuminating the FPC by a source antenna, a considerable enhancement in the antenna radiation characteristics can be achieved [35]–[39]. These antennas have been designed using various types of PRS superstrates made of periodic metallic patches or slots [40]-[42], single-layer [32] or multilayer dielectric slab superstrates [43]-[44]. One of the main constraints of such cavities is their 3 dB gain/power bandwidth as it will be discussed in the second section of this chapter. In this chapter, initially, aiming for the minimum size of PRS superstrate, we are presenting a simple model of the diffraction and transmission rays. The limitation of the 3-dB gain bandwidth is one of the critical disadvantages of FPC antenna. Therefore, to expand the 3-dB gain bandwidth, an investigation in the next section of this chapter is given that relies on an image theory and effective medium method.

Gain Enhancement of Dielectric Resonator Antenna (DRA) Using FSS Layer

In this section, a high gain circularly polarized (CP) dielectric resonator antenna (DRA) is proposed. The radiating DR is coupled to a 50-ohm microstrip line through an X-shaped slot etched off the common ground plane. Using an FSS superstrate layer, a gain enhancement of 8.5 dB is achieved. A detailed theoretical analysis is given and used to optimize the superstrate size and the air gap height between the antenna and superstrate layer. Meanwhile, the proposed DRA is designed, simulated, implemented, and measured. The high gain CP DRA has the potential to be used for millimetre wave wireless communication and imaging systems.

3.1.1 Dielectric Resonator Antenna (DRA) Design

The geometry of the DRA with the FSS superstrate layer is depicted in Figure 3-1. The proposed FPC design consists of two substrate layers. The first layer is a 0.254 mm thick Rogers 3006 substrate with relative permittivity of 6.15. The 50- microstrip feed line is printed on the bottom of the first layer. The second layer is a 0.787 mm thick substrate with dielectric constant of 2.2. An x-shaped slot is etched off the ground plane on the upper side of the lower substrate. The slot is coupled to a low-loss and high-efficiency rectangular DRA. The dimensions of DRA and x-shaped slot are given in Figure 3-1 (b). The photographs of the implemented DRA are shown in Figure 3-2.

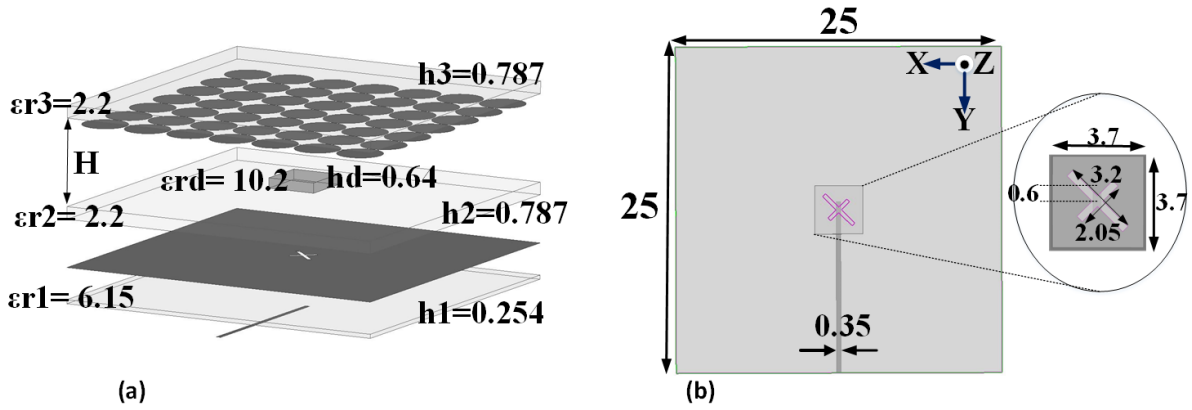

Figure 3-1: The geometry of the FPC antenna with radiating DR and an FSS superstrate layer (a) 3D view and (b) top view (measurements are in millimetre).

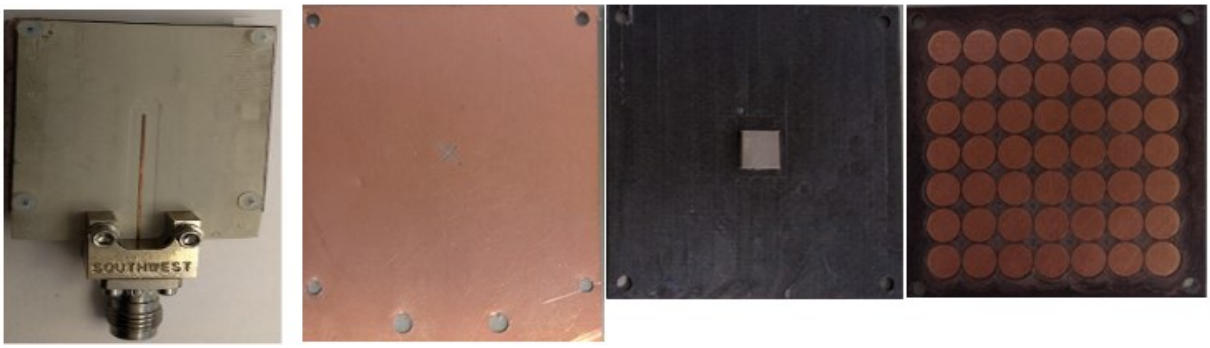

(a) (b) (c) (d)

Figure 3-2: Photos of the fabricated antenna (a) the bottom surface of first layer (feedline), (b) top surface of the first layer (ground plane), (c) top surface of the second layer (DR), and (d) the bottom surface of the third layer (FSS elements).

A simple dielectric waveguide model (DWM) has been used to evaluate the resonant frequencies in the DR. The resonant frequency for rectangular DRA can be computed as follows [49], [50]:

$$f_r = \frac{c}{2\pi\sqrt{\varepsilon_r}}\sqrt{\left(\frac{m\pi}{a}\right)^2 + k_y^2 + \left(\frac{l\pi}{2d}\right)^2} \tag{3-1}$$

$$k_y \tan\left(\frac{k_y b}{2}\right) = \sqrt{(\varepsilon_r - 1)k_o^2 + k_y^2} \qquad \text{(n=1)} \tag{3-2}$$

$$\left(\frac{m\pi}{a}\right)^2 + k_y^2 + \left(\frac{l\pi}{2d}\right)^2 = \varepsilon_r k_0^2 \tag{3-3}$$

Where c is the speed of light in vacuum, k_0 and k_y are the wavenumbers in free space and inside the DR in the y-direction, respectively. Parameters a, b and d are the length, width, and height of the DRA, respectively. Utilizing the DWM and Rogers 6010 substrate with dielectric constant 10.2, a DR with a = 3.7 mm, b = 3.7 mm, and d = 0.64 mm is selected. This results in the dominant mode at the resonant frequency of 30 GHz. An FSS of 7×7 cells is printed on the rear side of the superstrate (the third layer). The superstrate is separated from the DRA by an air gap (H). Generally speaking, parameters such as the characteristics of the DR (dielectric constant, shape, and dimension), length and width of the coupling aperture, the height of the superstrate from radiator, dimensions and period of the FSS elements are key parameters to control different resonance frequencies for wideband applications.

In this thesis, all simulation results, except for RCS, were obtained using Ansys HFSS. The simulated results for the reflection coefficient, axial ratio, total gain, and radiation efficiency of the antenna without superstrate layer are depicted in Figure 3-3. It can be observed that the antenna's impedance bandwidth is from 25 GHz to 31.4 GHz (22.7%), CP bandwidth from 26.9 GHz to 34.8 GHz (25.6%), and total gain of 6.4 dB at 30 GHz. Impedance and CP bandwidths correspond to S11< -10 dB and AR< 3 dB. As can be seen in Figure 3-3, the radiation efficiency of the DRA alone is above 90% on the desirable bandwidth, but the gain of the antenna is not high enough for MMW applications. Therefore, the directivity must be enhanced, and this can be done using the technique that is described in the following section.

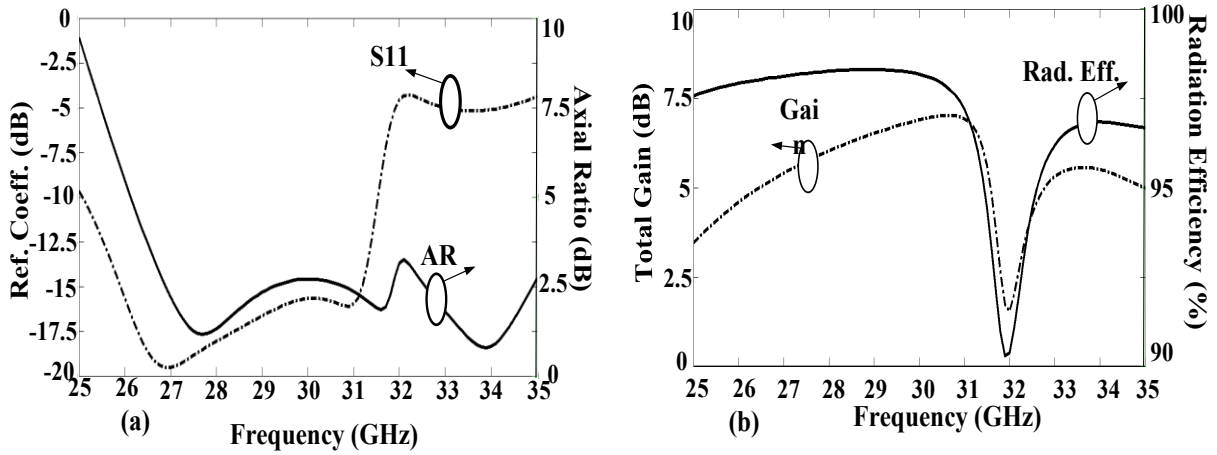

Figure 3-3: The simulated results of (a) reflection coefficient and axial ratio, and (b) total gain and radiation efficiency of the DRA without the FSS layer.

3.1.2 Design of FSS Superstrate Layer

To improve the antenna gain, this thesis proposes an FSS superstrate on the top of a basic aperture coupled DRA with a separating air gap. Furthermore, using one or more FSS superstrates, various resonant frequencies can be achieved, although there is a limitation due to the required compact antenna size. It should be noted that an FSS superstrate will reduce the impedance bandwidth significantly.

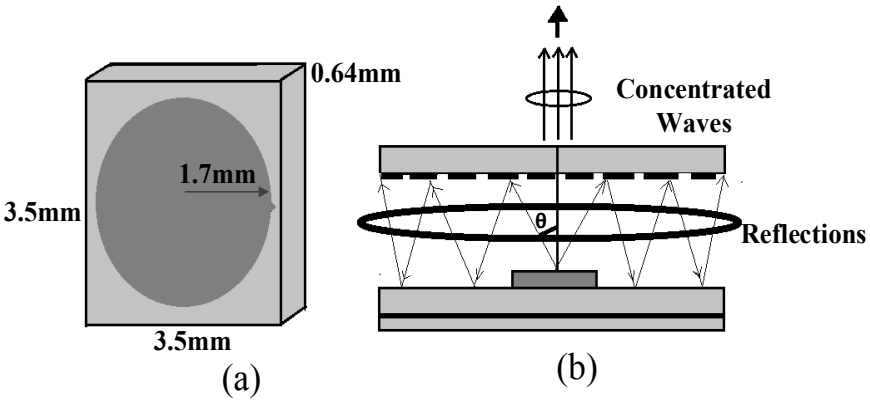

Figure 3-4: (a) The dimensions of the FSS unit cell and (b) illustration of multiple reflections and leaky waves.

The dimensions of the FSS unit cell are shown in Figure 3-4 (a). Figure 3-4 (b) illustrates a sketch of multiple reflections inside the cavity and the EM wave leakage through the FSS superstrate. It

can be seen that waves reflected inside the air gap will be partially transmitted through the superstrate in the antenna broadside direction when the reflection and transmission wave phases of the DRA, air gap, and FSS superstrate are precisely tuned. Accordingly, a considerably directive beam is created at the desired frequency. Figure 3-5 depicts a transmission line circuit model of the suggested structure (shown in Fig. 3.1).

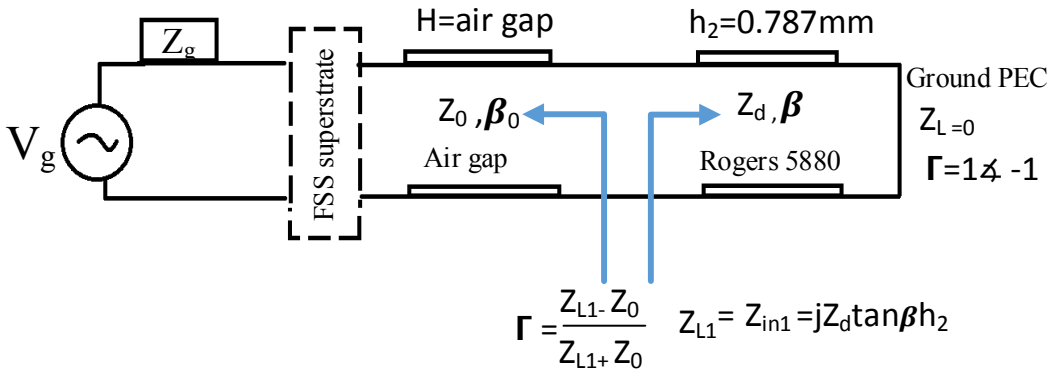

Figure 3-5: Transmission line circuit model for mismatched load and generator.

It consists of two cascaded transmission lines with lengths H and h_2, characteristic impedances Z_0 and Z_d, and arbitrary generator and load impedances Z_g and Z_L, respectively. In this case, the input impedance is given by [52]:

$$z_{in} = z_0 \frac{z_L + jz_0 \tan \beta h_2}{z_0 + jz_L \tan \beta h_2} \tag{3-4}$$

Z_{in} is the input impedance of a transmission line of length h_2 terminated with Z_L. When a PEC ground plate is used as a terminating load as shown in Figure 3-5, we have

$$z_{l1} = z_{in1} = jz_d \tan \beta h_2 \tag{3-5}$$

Where $Z_d = (Z_0/\sqrt{\varepsilon_r})$ and $\beta = \left(\frac{2\pi\sqrt{\varepsilon_r}}{\lambda_0}\right)$. As shown in Figure 3-5, the reflection coefficient at the Z_{L1} as the terminating load is given by

$$\Gamma = \frac{jz_d \tan \beta h_2 - z_0}{jz_d \tan \beta h_2 + z_0} \tag{3-6}$$

From (3-6) the phase of reflection coefficient for the ground and substrate 5880 can be estimated as below

$$\varphi_{\Gamma}(ground, sub) = \pi - 2\tan^{-1}(\frac{z_d}{z_0}\tan(\beta h_2)) \tag{3-7}$$

Hence

$$\varphi_{\Gamma}(ground, sub) + \varphi_{FSS} - \frac{4\pi H}{\lambda} = 2N\pi \tag{3-8}$$

Note that, "H" is air gap between antenna and superstrate and "N" is the integer number. It is concluded, based on (3-8) that the DRA bandwidth can be enhanced if the FSS reflection phase decreases gradually. The directivity can be obtained from the magnitude of the reflection coefficient on the broadside direction (θ=0) as [53], [66]:

$$Directivity = \frac{1+|\Gamma_{FSS}|}{1-|\Gamma_{FSS}|} \tag{3-9}$$

It can be seen from (3-9) that the DRA directivity increases with the higher magnitude of the reflection coefficient. Thus, in order to have a perfect FSS superstrate, it must satisfy requirements of flat reflection phase and high reflection magnitude versus frequency [53]. The FSS was simulated and optimized utilizing commercial full-wave EM simulation software HFSS 15.0. The periodic boundary conditions (PBCs) and Floquet port are used to simulate the infinite periodic cells. Each FSS is printed on a Rogers 5880 with relative permittivity 2.2 and thickness of 0.787mm. The FSS structure shown in Figure 3-4 (a) is a simple circle with a 1.7mm radius within a 3.5×3.5mm unit cell. The height of the unit cell is calculated for the centre frequency of 30 GHz. The phase of the reflection and transmission coefficients, as well as the reflection magnitude of the FSS, are depicted in Figure 3-6.

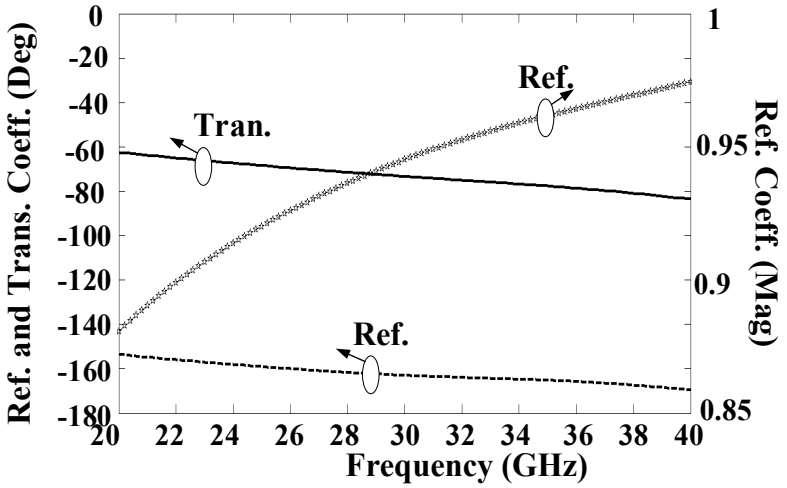

Figure 3-6: The phase and magnitude of reflection and transmission coefficients of the FSS unit cell

It can be seen that reflection magnitude is higher than 0.9 in the frequency range from 20 to 40GHz and the reflection phase is decreasing steadily with frequency resulting in high directivity. One of the challenges in these antenna structures is to determine the size of the superstrate including the number of FSS units. In order to overcome this challenge, we apply and extend, as shown in Figure 3-7, a method to approximate a square superstrate.

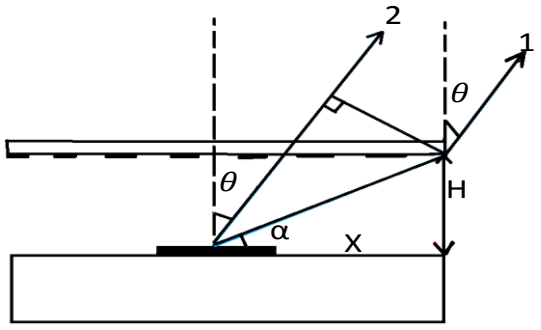

Figure 3-7: Model of the diffraction and transmission rays.

The model demonstrates diffraction and transmission rays from the superstrate that will lead to the same phase of the transmitting and diffracting waves resulting in a further directivity enhancement. In Figure 3-7, rays 1 and 2 are the first diffracted and transmitted rays and their respective phase angles are given as

$$(phase)_1 = e^{-j(\frac{2\pi H}{\lambda \sin\alpha})} \tag{3-10}$$

$$(phase)_2 = e^{-j((\frac{2\pi H \cos(\frac{\pi}{2}-\alpha-\theta)}{\lambda \sin\alpha}) + \varphi_{tr})} \tag{3-11}$$

where α and θ are the elevation angles from the radiating centre to the edge of the superstrate and rays 2, respectively. In additon, φ_{tr} is the transmission phase of the FSS. Using (3-10) and (3-11), the phase angles of diffraction and transmission rays are equal when,

$$\frac{2nH}{\lambda \sin\alpha} = \frac{2\pi H \cos(\frac{\pi}{2}-\alpha-\theta)}{\lambda \sin\alpha} + \varphi_{tr} \tag{3-12}$$

Here "θ" is suppoesed so small, hence, (3-12) can be re-written as

$$\frac{H}{\lambda}(\frac{1}{\sin\alpha}-1) - \frac{\varphi_{tr}}{2\pi} = N \tag{3-13}$$

In order to obtain the optimum size of the superstrate including the number of FSS unit cells, (3-4) to (3-8) are applied and result in φ(ground, sub) is 128° and air gap (H) equals 4.5mm. Parametric studies using HFSS, as depicted in Figure 3-8, are used to maximize the total gain while also adjusting the CP band over the desired bandwidth. Various parameters in (3-4) through (3-13) are summarized in Table 3-1.

Table 3-1: Parameter values of equations of (3-4) to (3-13)

Parameter	**values**	**Parameter**	**values**	**Parameter**	***values***
fr (GHz)	30	β	0.9	$\varphi_{(FSS)}$ (deg)	-163
$Z_{0\ (ohm)}$	377	d (mm)	0.787	φ_{tr} (deg)	-73
ε_r	2.2	Z_{d} (ohm)	254.7	α (deg)	22
N	1	$\varphi_{\Gamma(ground,\ sub)}$	128	X (mm)	12

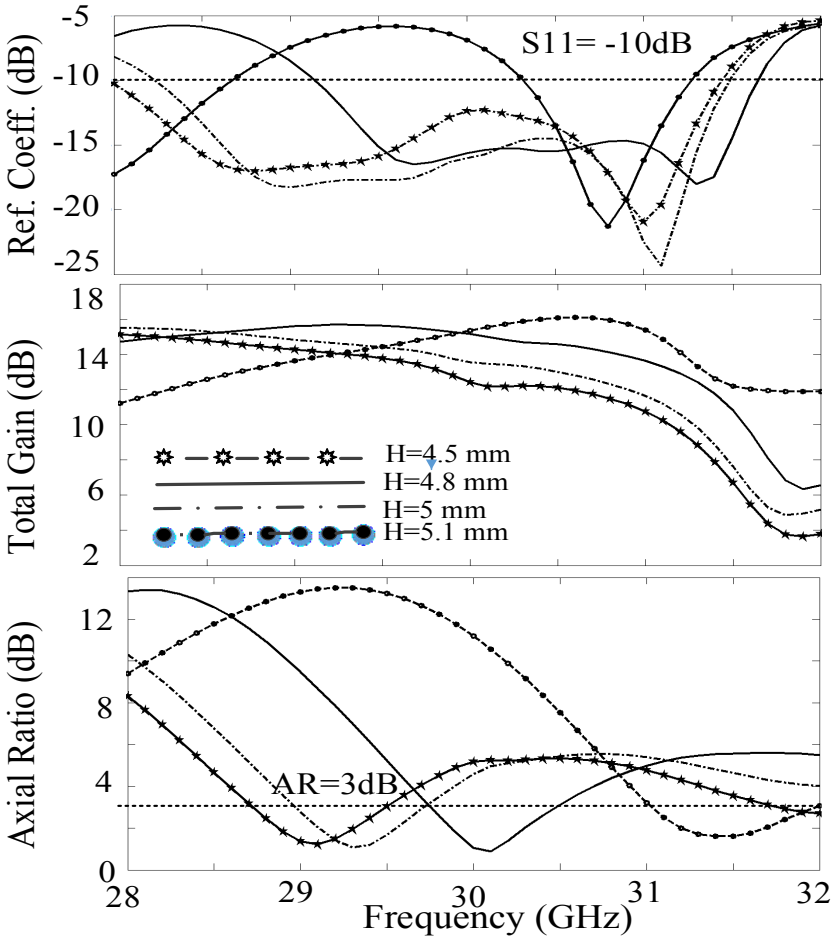

Figure 3-8: The simulated results of the reflection coefficient, total gain, and axial ratio for different values of the airgap heigh H.

It can be seen that the air gap "H" is 4.8 mm which is slightly different from the corresponding value of 4.5mm obtained from the theoretical analysis. Note that as shown in Figure 3-8, the parameter X is defined as the radius of the circular superstrate. Theoretically, the estimated size of the square FSS superstrate is acquired 24 mm×24 mm. Since the dimension of the unit cell is 3.5 mm×3.5 mm, the minimum size for the (7×7) FSS superstrate is 25 mm×25 mm. Figure 3-9 shows the 3D radiation patterns of the aperture coupled DRA for three cases at 30 GHz. It can be observed that the simulated gain of single DRA, DRA with the only superstrate without FSS elements, and the proposed antenna have 7 dB, 9.27 dB, and 15.5 dB, respectively. There is an 8.5 dB increase in the gain for the case of the proposed DRA with the FSS superstrate in comparison with the DRA alone.

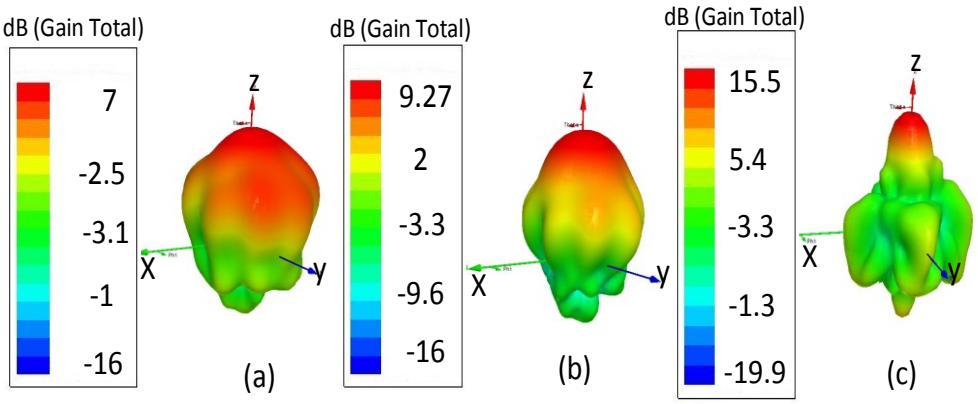

Figure 3-9: 3D radiation patterns of the aperture coupled DRA at 30 GHz for three cases: (a) the basic DRA, (b) the DRA with the only superstrate, and (c) DRA with the FSS superstrate.

The E-field vector variations at a wavelength distance for various phases are shown in Figure 3-10.

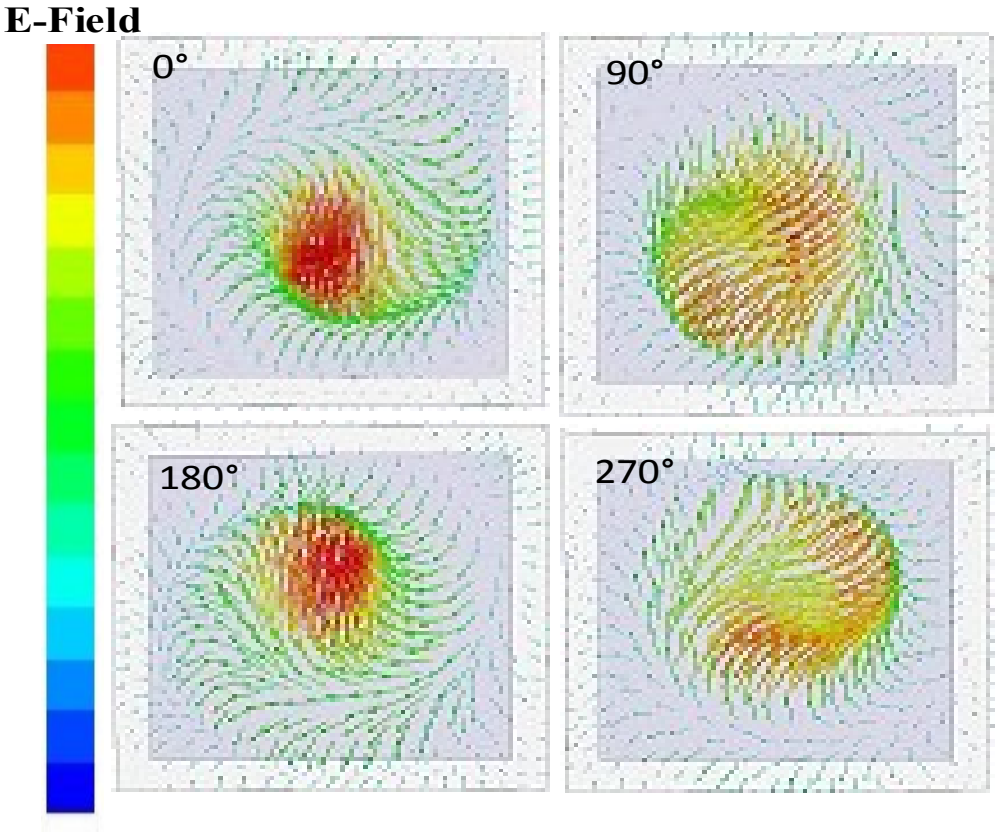

Figure 3-10: RHCP E-field variations at different phases (a) 0°, (b) 90°, (c) 180°, and (d) 270 °at the centre frequency 30 GHz.

It can be observed that the radiated field from the antenna rotates in clockwise direction, indicating it is right-hand circular polarization. The proposed DRA with superstrate and FSS unit cells were fabricated and measured. The measurements of the reflection coefficient (S11) for the proposed antennas were done utilizing an Agilent N5227A PNA Network Analyzer (10MHz-67GHz). A linearly polarized (LP) probe was used to sequentially measure the electric field in two orientations during the radiation pattern measurements. The left and right-hand fields and AR of the antenna were then calculated from the measured electric fields, with both amplitude and phase [55]:

$$\vec{E}_{\theta} = \left|E_{\theta}\right| \square \qquad \vec{} \qquad \left| \right| \square \tag{3-14}$$

$$\vec{E}_{RH} = \frac{1}{\sqrt{2}}(\vec{E}_{\theta} + j\vec{E}_{\varphi}), \vec{E}_{LH} = \frac{1}{\sqrt{2}}(\vec{E}_{\theta} - j\vec{E}_{\varphi}), \tag{3-15}$$

$$AR(dB) = 10\log\left(\left|\frac{\left|\vec{E}_{RH}\right| + \left|\vec{E}_{LH}\right|}{\left|\vec{E}_{RH}\right| - \left|\vec{E}_{LH}\right|}\right|\right) \tag{3-16}$$

The measured and simulated results of total gain, axial ratio, and reflection coefficient are depicted in Figure 3-11. It is obvious that both the simulation and measurement results have an acceptable agreement. The fabricated antenna is able to cover an impedance bandwidth from 29 GHz to 31.5 GHz (8.26%) with an axial ratio bandwidth from 29.7 to 30.6 GHz (2.97%), and a total gain of 15.5dB at the central frequency of 30GHz. Figure 3-12 illustrates the radiation pattern of the proposed DRA at the operating frequency (30GHz) on the x-z and y-z planes. It is observed that the side lobe level (SLL) is nearly -13 dB on both planes. In addition, the simulations and measurements have an acceptable agreement with each other.

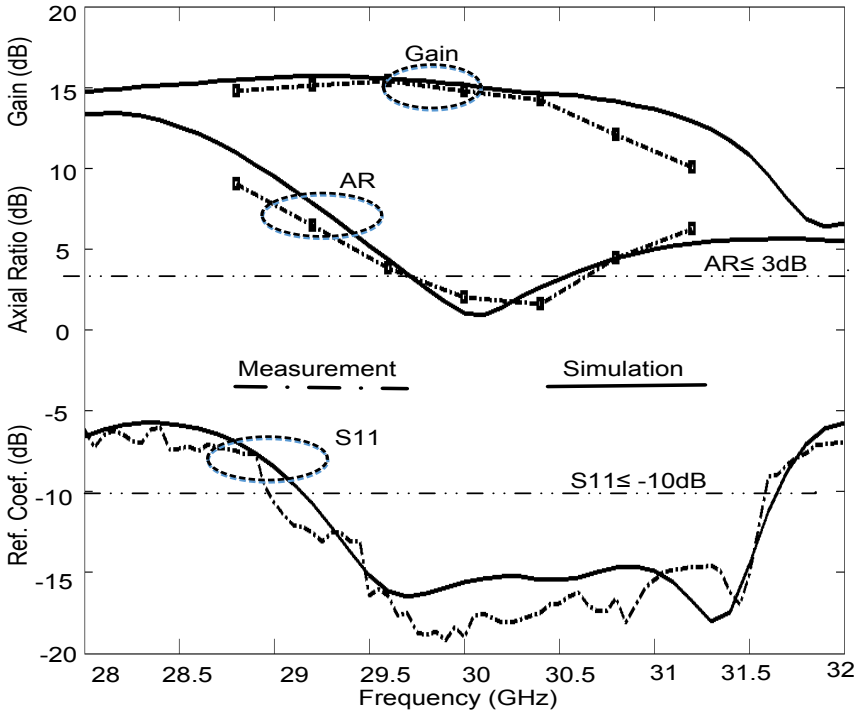

Figure 3-11: Measured and simulated curves of the total gain, axial ratio, and reflection coefficient of the proposed antenna.

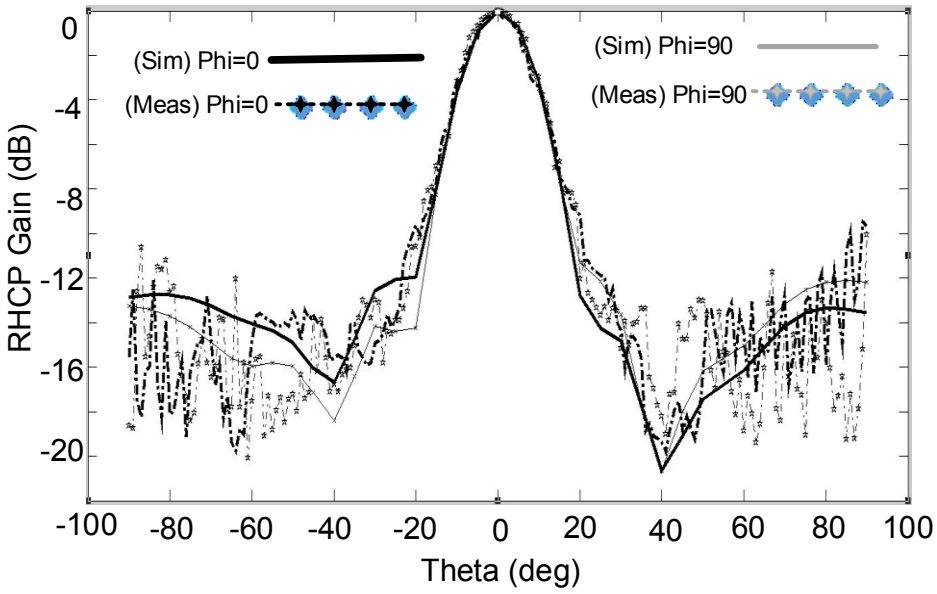

Figure 3-12: The normalized gain of the proposed antenna at 30GHz on both planes phi=0 and phi=90.

Conclusion

As the first design in this chapter, theoretical analysis has been used to design and optimize a high gain CP Fabry-Perot DR antenna for MMW applications. The antenna gain has been improved using a superstrate layer configured as a 7×7 FSS structure. The CP has been achieved by etching an X-shaped slot off the ground plane of the aperture coupled antenna. The measured results of the fabricated antenna have shown that it is able to cover the impedance and axial-ratio bandwidths 8.26% and 2.97%, respectively. Furthermore, it has a total gain of 15.5dB on broadside at 30GHz. There is an acceptable agreement between simulation and measurement results. These characteristics make the proposed antenna a suitable candidate for millimetre-wave wireless communication systems.

Chapter 4. Spatially Coupling Reduction in MIMO Antennas Using FSS

Introduction

The interactions between EM fields of the adjacent closely spaced antennas is defined mutual coupling. It can degrade the antenna array performance in terms of impedance and radiation characteristics [70]. Depending on the shape of antennas (i.e., planar or nonplanar), fabrication technologies, arrangement type, and distance between them, mutual couplings are grouped as follows: (i) the signal leakage via surface wave propagating along substrate dielectric and air interface [71], [72], (ii) the conducting current due to the existence of continuous metallic ground plane [73], (iii) the mutual coupling between the feeding lines [74], and (iv) the coupling due to the spatial electromagnetic fields [75].

Multiple-input multiple output (MIMO) systems in MMW frequency band have become an emerging technology for future indoor and outdoor communications because they permit the next generation mobile networks (NGMN) to provide high data rates in order to improve the link performance [76]. Enhancement in radiation efficiency of MIMO wireless systems demands a lower envelope correlation and a further degree of isolation between the adjacent antennas [77]. Hence, mutual coupling reduction between adjacent antenna elements in MIMO systems has been investigated by different authors [89]–[91]. A coplanar strip wall between two antennas was studied in [89]. Although, such a technique deteriorates the antenna's radiation pattern. This is due to the fact that the coplanar strip wall is not matched well. Metamaterials have been extremely analyzed recently to enhance many antenna radiation characteristics because of their unusual EM features [90]-[91]. In order to reduce the mutual coupling of the spatial EM fields, improving simultaneously, the radiation performance of the antennas, metasurface, and FSS as the superstrate of the antennas were proposed [75], [92]-[94]. Note that, depending on the antenna's radiation pattern shape, the spatially mutual coupling is generated in near-field areas. However, the decoupling designs operate on the basis of coupling reduction of either E or H-Fields between linearly polarized (LP) antennas. Recently, due to factors such as polarization mismatch, multipath phenomenon, and phasing subjects, the trend to design the circularly polarized (CP) antennas is expanding [4], [66]. As mentioned before, the most of the studies in the literature apply the similar principle to reduce the coupling among LP antennas. In [92]-[93] a new technique has been observed based on metasurface layer on the top of MIMO planar

dipoles with the inter-element spacing 0.3 λ and 0.5 λ. However, it functions for linear structures and also the coupling reduction is not tangible, so that the improvement of 3 dB and between 8 to 14 dB in different cases in the orientation of H-plane is obtained, whilst in the E-plane coupling is not significant as compared with the air coupling (without superstrate).

In this chapter, coupling reduction behaviour on MIMO-CP antenna systems based on a two-layer transmission-type FSS is investigated. Correspondingly, the FSS layers transmit a large proportion of incident EM wave on the preferable frequency band. Thus, the antenna's radiation pattern is slightly concentrated upward, leading to a spatially coupling suppression between the adjacent antennas. However, due to the fact that each FSS element with different phases is illuminated, insignificant reflections are scattered from the FSS layers which is the main drawback of this approach. To address this imperfection, considering the FSS layers as a uniform planar array, the author has determined the near-field behaviour of FSS layers on the backside toward the radiating antennas. It is realized that by tuning few design parameters, the phase of reflections can be controlled. As a result, the insignificant reflections can easily be redirected along the nulls and away from the radiating antennas to prevent any interference. As the second design of this chapter, an effective approach for reducing the spatially coupling between DR antennas using a new FSS polarization-rotator wall is presented. The coupling reduction is obtained by embedding an FSS wall between two DRAs, which are placed in the H-plane. Using this FSS wall, the TE modes of the antennas become orthogonal, which suppresses the coupling between the two DRAs. The proposed FSS wall approximately has no influence on the DRA characteristics with respect to input impedance and radiation pattern. The radiation pattern is approximately unchanged compared to a DRA MIMO antenna array without FSS wall.

Spatially Decoupling of CP-MIMO Antennas Based on FSS

In this section of this chapter, an effective approach for mitigating the near-field coupling between four-port circularly polarized (CP) antennas in a 30GHz Multiple-Input, Multiple-Output (MIMO) system is suggested and investigated. This is obtained by incorporating a two-layer transmission-type frequency selective surface (FSS) superstrate based on planar crossed-dipole metal strips. The study presents a comparison between the mutual coupling when the patches are radiating in free space and in the presence of the FSS layers. The simulated results,

when the FSS layers are applied, show an average of 6 to 12dB improvement in the isolation between four adjacent CP-MIMO antennas. In addition, an accurate study is carried out on the insignificant reflections produced by FSS layers to redirect those and also prevent any interference. The proposed 2×2 CP-MIMO antenna along with the superstrate is implemented and tested to validate the simulation results. Experimental results of coupling and reflection coefficients, and axial ratio show an acceptable agreement with the corresponding simulated ones.

4.1.1 Unit Cell Model of FSS Layers

The transmission-type FSS layer topology is shown in Figure 4-1, where it consists of two identical dielectric boards, insulating Rogers 5880 with relative permittivity 2.2 and thickness 0.787 mm, with the same cross dipole metal traces on each layer. The proposed FSS layer is able to transmit most of the CP incident wave within the desired frequency band without significant influence on its phase, magnitude and rotation orientation, as shown in Figure 4-1. Note that, in order to cover the broad bandwidth, the two dielectrics are attached to each other.

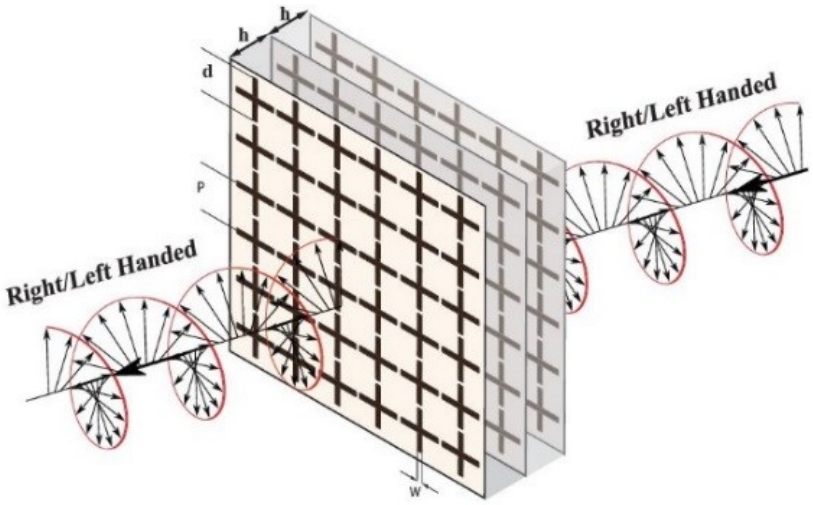

Figure 4-1: The schematic model of the transmission-type FSS superstrate illuminating by CP wave (h=0.787mm, d=2.7mm, P=3mm, and W=0.3mm)

Figure 4-2 shows the equivalent circuit of FSS layer including inductive and capacitive elements, and transmission lines. The cross dipole traces can be separated into vertical and horizontal conducting strips and are modelled as inductive and capacitive elements, respectively.

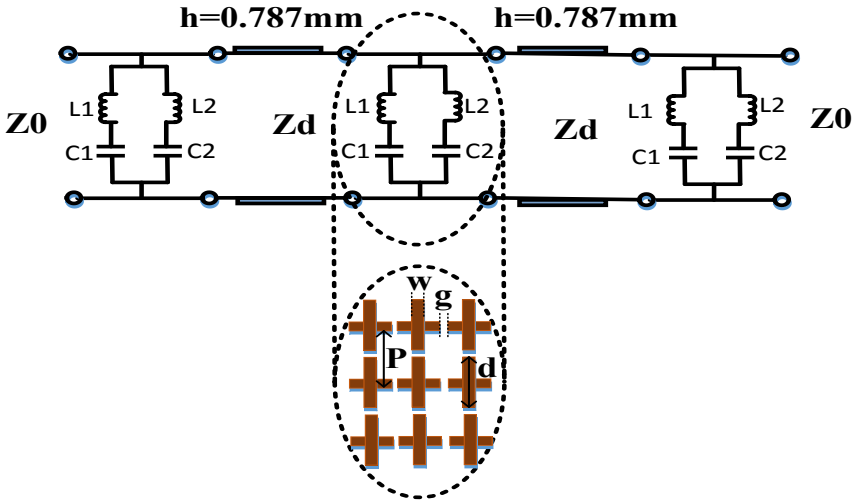

Figure 4-2: The equivalent circuit of FSS layers including inductive and capacitive elements [95].

For an array of thin, continuous, infinitely long and perfectly conducting narrow strips, the shunt impedance is either inductive or capacitive, depending on the incident wave, whether it is polarized parallel to or perpendicular to the edge of the strips [95]. The vertical strips, parallel to the electric field in the case of TE-wave, are modelled as a shunt inductive reactance in the equivalent circuit. One should note that cross dipoles are symmetric in horizontal and vertical orientations. Also, a CP wave is considered as a superposition of two orthogonal LP waves. Meanwhile, detailed expression of equivalent circuit inductive and capacitive reactances are given in [95]. Different design parameters for the FSS unit cell of a crossed dipole is exhibited in Figure 4-3.

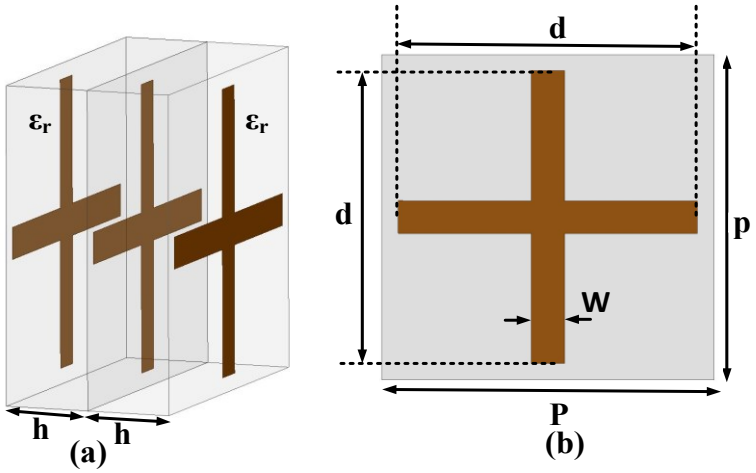

Figure 4-3: The unit cell model of crossed dipole FSS (a) side view and (b) top view (d=2.7mm, P=3mm, W=0.3mm and εr=2.2, and h=0.787mm,).

It is observed that the same crossed dipole FSS traces are printed on the top, middle, and bottom of two substrate layers, Rogers 5880 with relative permittivity 2.2 and thickness 0.787mm. Once "P" is much lower than the wavelength, by the equivalent LC circuits in both directions of horizontal and vertical, not only the different resonances can easily be produced, but also the capability of phase control is yielded on the frequency band, contributing to a broader bandwidth. In order to observe the behaviour of the crossed dipole FSS with infinite elements, the unit cell model of Ansys HFSS, which is a Finite-Element-Method (FEM) based on a full-wave simulator, is applied. In this model, two Floquet ports to excite along with master/slave boundaries are utilized. As shown in Figure 4-4, the impedance bandwidth of the proposed design for $S_{11} \leq$ -10dB is from 28.5GHz to 34.5 GHz (19%). The transmission behaviour of the crossed strip FSS elements can be determined by magnitude and phase of transmission coefficient. It is observed in Figure 4-4 that on the impedance bandwidth (28.5-34.5GHz), amplitude and phase difference of two orthogonal transmitted field components for the incident CP wave is insignificant. As a result, the FSS layers nearly have an ideal transmission characteristic for the input CP wave.

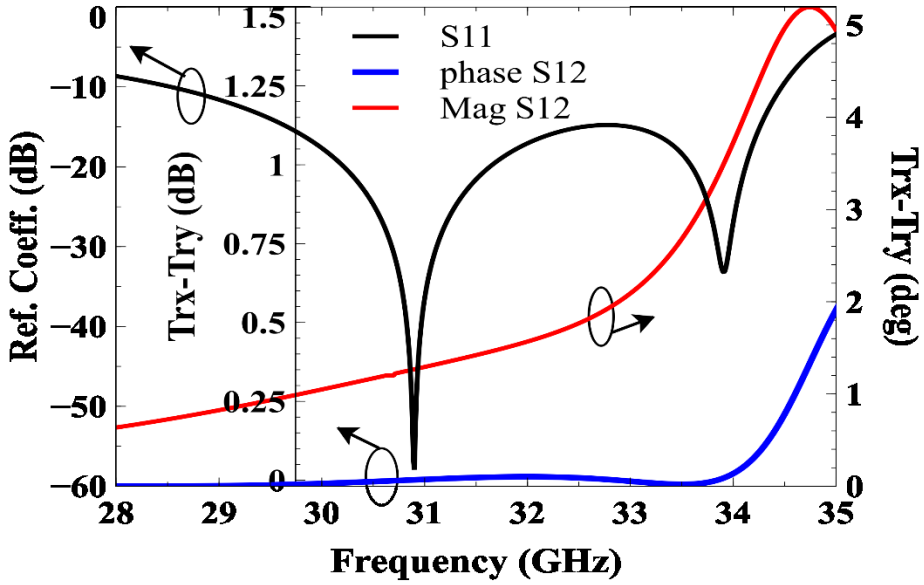

Figure 4-4: simulated results of S-parameter for the unit cell model of FSS

4.1.2 Single-Element Antenna Design

In order to contribute to the wide frequency band and broadside pattern, a single aperture coupled microstrip antenna (ACMA) is presented. As depicted in Figure 4-5, the ACMA with the capability of circular polarization consists of two different dielectrics as substrates: A Rogers 3006 (ε_r=6.15, H_1=0.254mm) substrate in the bottom while the top one is Rogers 5880 (ε_r=2.2, H_2=0.787mm). On the middle of the ACMA, a conductive plate as a ground plane along with cross slot etched off its centre is used to provide the required coupling.

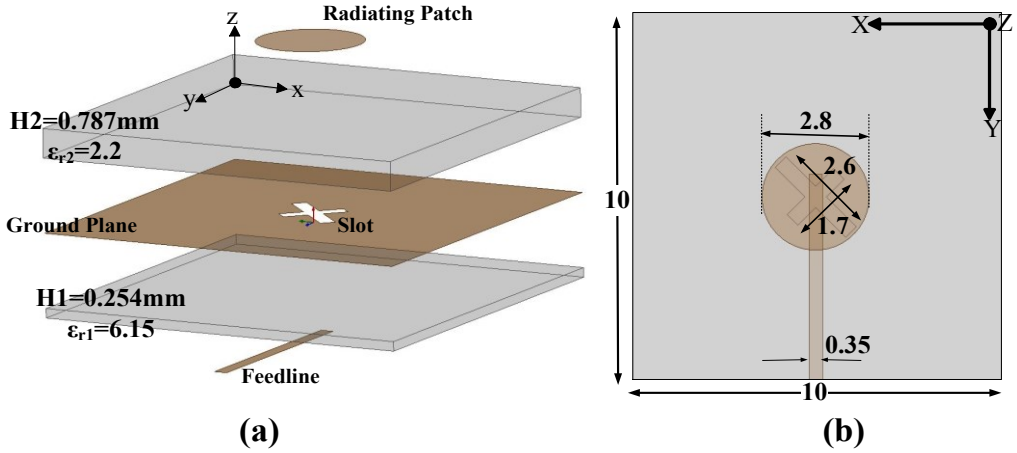

Figure 4-5: Geometry of single CP-ACMA (a) side view and (b) top view

Besides, a 50-ohm microstrip feed line and a circle-shaped patch are printed on the lower and upper layers of the ACMA, respectively. The antenna is designed to operate at the centre frequency 30GHz. Figure 4-6 shows the equivalent circuit of the single ACMA. It consists of the input port and a quarter-wave impedance transformer from the centre of the cross-shaped slot to the end of the line to represent the open circuit behaviour. The simulated results of the reflection coefficient and axial ratio are shown in Figure 4-7, in which exhibits that the ACMA covers impedance and CP bandwidths from 28 GHz to 34 GHz (19.3%) and 30.2 GHz to 32 GHz (6%), respectively.

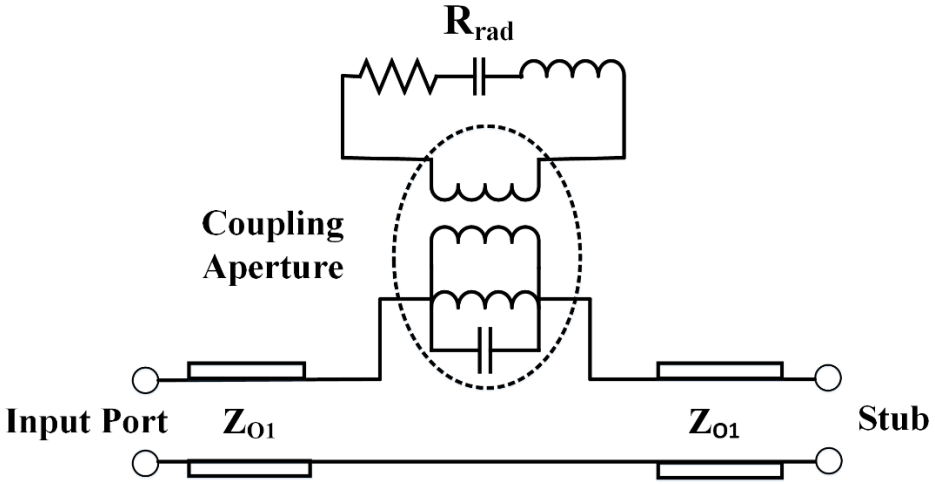

Figure 4-6: The equivalent circuit model of the ACMA [51]

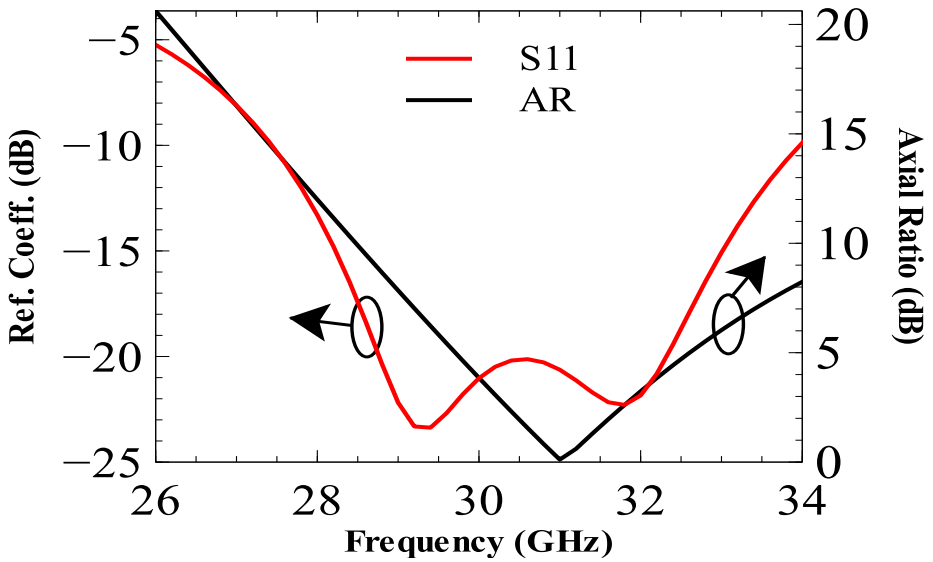

Figure 4-7: Reflection coefficient and axial ratio of a single element CP patch.

4.1.3 MIMO - ACMA Design: Reflection Array Factor

A Multiple-Input and Multiple-Output (MIMO) system is considered as a technique for multiplying the capacity of a radio link utilizing multiple transmit and receive antennas to exploit multipath propagation [96]. Using this concept, the proposed approach in this thesis aims to determine the influence of the coupling between elements of the MIMO-ACMA. To achieve this goal, four elements of the ACMA are formed in two by two array to illuminate the FSS layers. The schematic diagram of the MIMO-ACMA is exhibited in Figure 4-8, where the coupling coefficients in different directions and distance between the ACMAs are defined with parameters "C_d", "C_v", "C_h" and "di", respectively. One of the main disadvantages of this approach is to scatter insignificant reflections from the FSS layers as compared with ones without FSS superstrate. These negligible reflections occur due to the fact that the antenna sources illuminate the FSS elements with different oblique incidence angles. However, when the FSS elements are formed as a uniform planar array, it can deteriorate radiation levels of the antenna elements and degrades the mutual coupling between the radiating elements as well. Therefore, to overcome this problem, the reflection power density in the near-field region is applied. Since the array radiation pattern is always dominated by the AF, which has a scalar factor representing how the fields emitted from the many elements either in the near-field or far-field region.

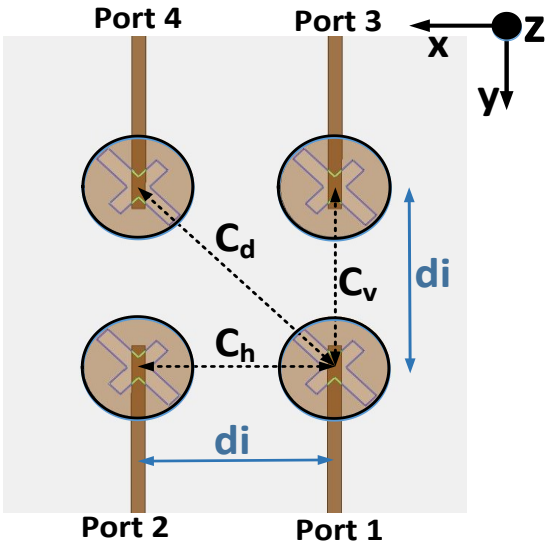

Figure 4-8: The schematic diagram of the MIMO-ACMAs with coupling coefficients (Cd, Ch, and Cv) and the inter-ACMA element spacing (di)

Therefore, the reflection effect is dominant when the number of FSS elements on the superstrates is increased. As shown in Figure 4-9, the schematic of transmission-type FSS superstrate with transmission and reflection gains with respect to the S- parameters and AF is observed. It is apparent that the transmission gain at broadside is greater than reflected one at backside which demonstrates that the FSS layer is a transmission–type superstrate.

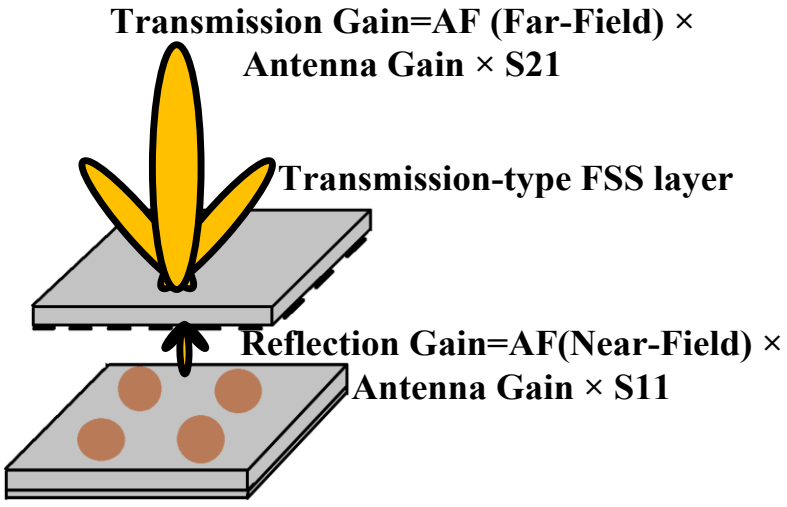

Figure 4-9: The schematic of the transmission-type FSS layer with transmission and reflection gains in two directions with respect to AF and S-parameters

As a result and as shown in Figure 4-9, it is able to transmit a large proportion of the incidence wave and reflects a small part at the backside. In order to address the reflection drawback, some design parameters of the proposed structure should be tuned, so that the radiation pattern of the reflection AF be redirected along the radiation nulls of the external antenna sources. These design parameters prevent any interference and deterioration in the radiation performance of external antenna sources. To address the above issues, the near-field reflection array factor is investigated. Figure 4-10 shows the sketch of 9×9 FSS elements on the superstrate along with the 2×2 MIMO ACMA below the FSS superstrate. The FSS array to be considered is uniform and planar in the x-y plane, as shown in Figure 4-10. The air gap between the external antenna sources and FSS layer is 2.5mm ($\lambda_0/4$ at 30GHz). Therefore, the induced current amplitude on each FSS element is assumed to be identical and isotropic. Therefore, to formulate the array factor, the phases of FSS elements' excitation currents when illuminated by a 2×2 MIMO antenna system should be computed. Figure 4-11 shows the geometry of a uniform planar array including 81 FSS elements above 2×2 MIMO-ACMA system with an air gap λ/4 at 30GHz (2.5mm) to compute the AF in the near-field region. Each FSS element occupies an identical area of 3×3mm^2 on the x-y plane. Referring to Figure 4-11, $R_s(n)$ represents the location of each antenna element, n=1, 2, 3, 4, and the centre position of the FSS unit cell is given by $R_{cell}(m)$, where m=1, 2, 3, …, 81.

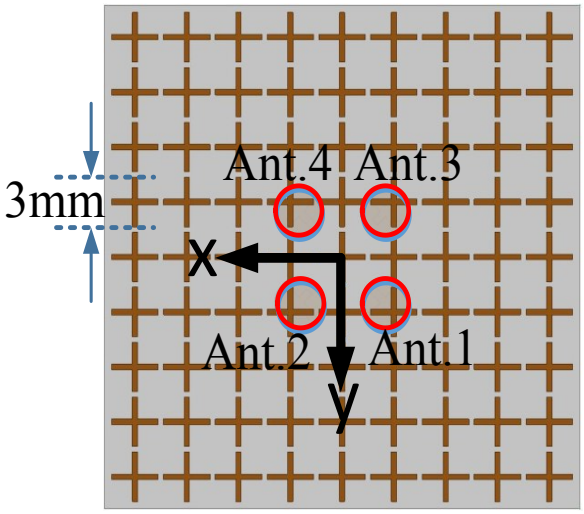

Figure 4-10: The formation schematic of FSS superstrate including 9×9 FSS elements, and the precise position of a 2×2 MIMO-ACMA below the superstrate in the x-y plane (the inter-element spacing di= λ/2).

Therefore, the electric field at the centre of the mth FSS unit cell when illuminated by the nth antenna element can be calculated as

$$\vec{E}_t(n,m) = E_0\left(e^{-\alpha R_t(n,m)} \times e^{-j\beta R_t(n,m)}\right)\hat{\alpha}_r \tag{4-1}$$

Where

$$\vec{R}_t(n,m) = \vec{R}_{cell}(m) - \vec{R}_s(n) \tag{4-2}$$

and α is the propagation loss in the air gap, and it is negligible and almost zero, and β is the corresponding propagation phase.

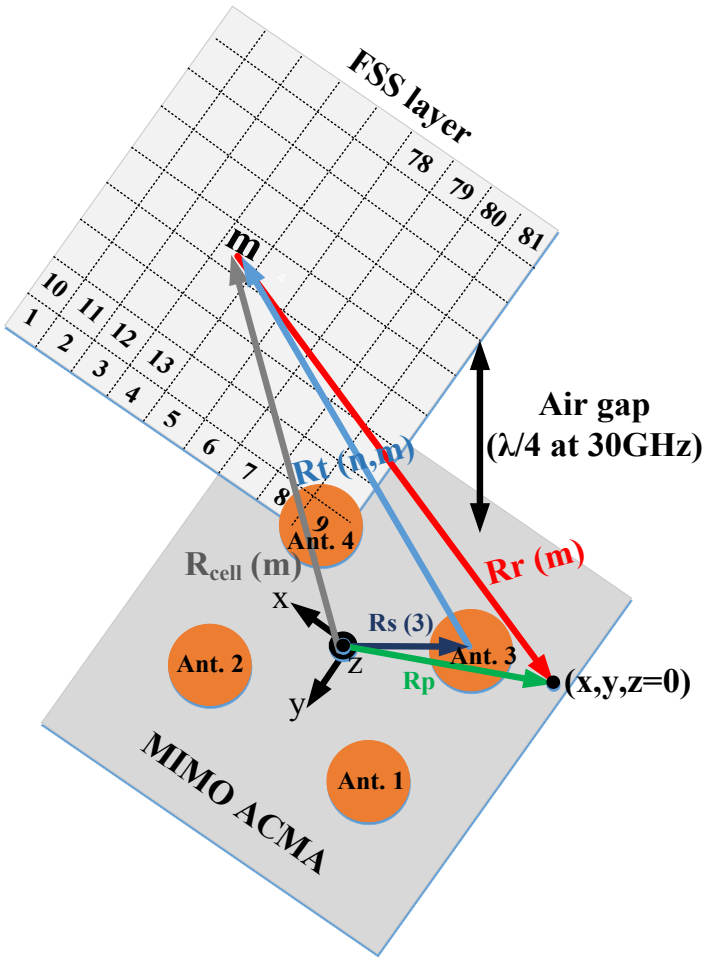

Figure 4-11: The sketch of a uniform rectangular array of 81 FSS elements with spacing 3mm along the x and y-axis above 2×2 MIMO-ACMA with an air gap 2.5mm along z-axis.

In addition, E_0 is the magnitude of the electric field which is assumed to be a constant. Thus, it can be simplified as

$$\vec{E}_t(n,m) = E_0 e^{-j\beta R_t(n,m)} \hat{\alpha}_r \tag{4-3}$$

Meanwhile, R_p and $R_r(m)$ can be defined as

$$\vec{R}_P = x\hat{\alpha}_x + y\hat{\alpha}_y \tag{4-4}$$

$$\vec{R}_r(m) = \vec{R}_p + \vec{R}_{cell}(m) \tag{4-5}$$

When the nth antenna element is illuminating the FSS layer, the reflected electric field at point (x, y, z=0) can be calculated as

$$\vec{E}_r(x, y, z = 0, n) = E_0 \sum_{m=1}^{81} \Gamma(n, m) \times e^{-j\beta R_t(n,m)} \times e^{-j\beta R_r(m)} \hat{\alpha}_r \tag{4-6}$$

where $\Gamma(n, m)$ is the reflection coefficient at the centre of the mth unit cell, when the wave is radiated by the nth antenna element. Note that, $\Gamma(n, m)$ is calculated using the unit cell simulation model by Ansys HFSS, as shown in Figure 4-4. The antenna has circular polarization, so the vector $\widehat{a_r}$ in (4-1) is rotating with an angular speed of $\omega_o = 2\pi f_o$, where f_o is wave frequency. Since CP wave is considered as superposition of two orthogonal LP waves, therefore, the normalized reflection power density at a point (x, y, z=0) when the nth antenna is radiating can be calculated as

$$\vec{E}_r(x, y, z = 0, n) = \sum_{m=1}^{81} \Gamma(n, m) \times e^{-j\beta R_t(n,m)} \times e^{-j\beta R_r(m)} \hat{\alpha}_r \tag{4-7}$$

Figure 4-12 shows the simulated 2D normalized reflection power density at z=0, when individual antenna elements is radiating. As a result, it is observed that the air gap between FSS superstrate and the antenna plane is considered as a key design parameter. For the proposed structure, the air gap with value 2.5mm (λ/4 at 30GHz) is a reasonable choice to redirect the reflection power density away from the MIMO-ACMA in order to prevent interference and deterioration in the antenna radiation characteristics.

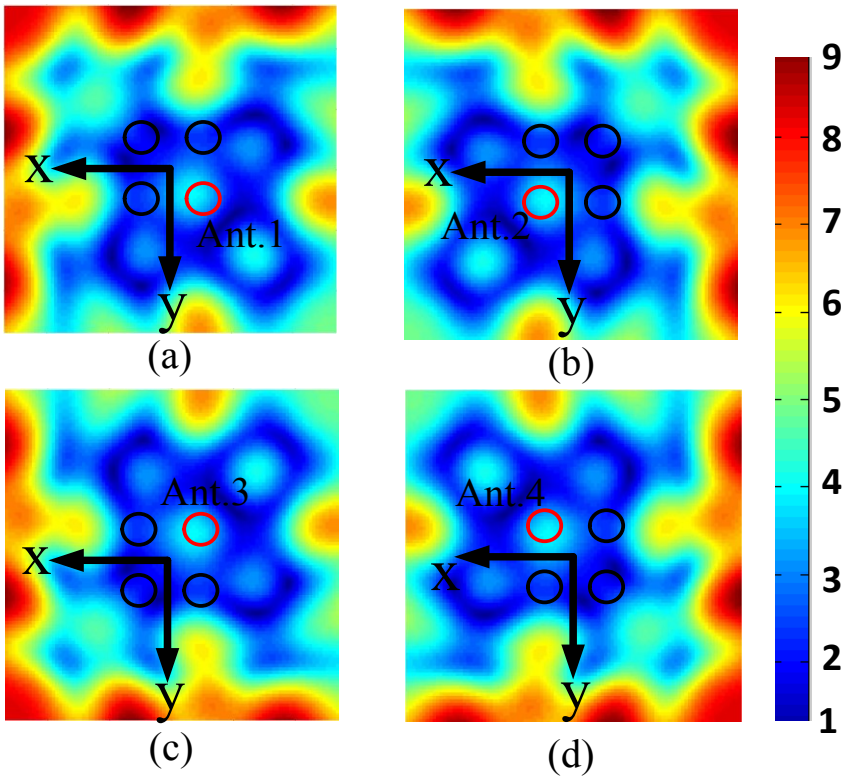

Figure 4-12: The 2-D reflection power density of the FSS elements on the antenna plane (the x- and y-axis) when those are illuminated separately by (a) Ant. 1, (b) Ant. 2, (c) Ant. 3, and (d) Ant. 4.

4.1.4 Simulated Results of the MIMO-ACMAs

In this section, the simulated results of 2×2 MIMO-ACMA for air and FSS couplings using the full-wave simulator Ansys HFSS are presented. One should note that in order to prevent enlarging the structure size and redirect reflected power density away from the MIMO antennas, the air gap between ACMA elements and FSS layer is considered to be 2.5mm (λ/4 at 30GHz). The simulated results of the axial ratio and S-parameters of the proposed structure for the two cases of air and FSS couplings, when the inter-element spacing varies from 0.5λ to 0.7λ, are presented in Figure 4-13. It is observed that the impedance bandwidth (s11≤ -10dB) for all cases is nearly identical, covering a band from 28GHz to 33GHz (16.4%). Therefore, it is noticed that the inter-element spacing and FSS layer do not significantly affect the impedance characteristics. On the other hand, the axial ratio is determined when the inter-element spacing is changed for the two cases of air and FSS couplings.

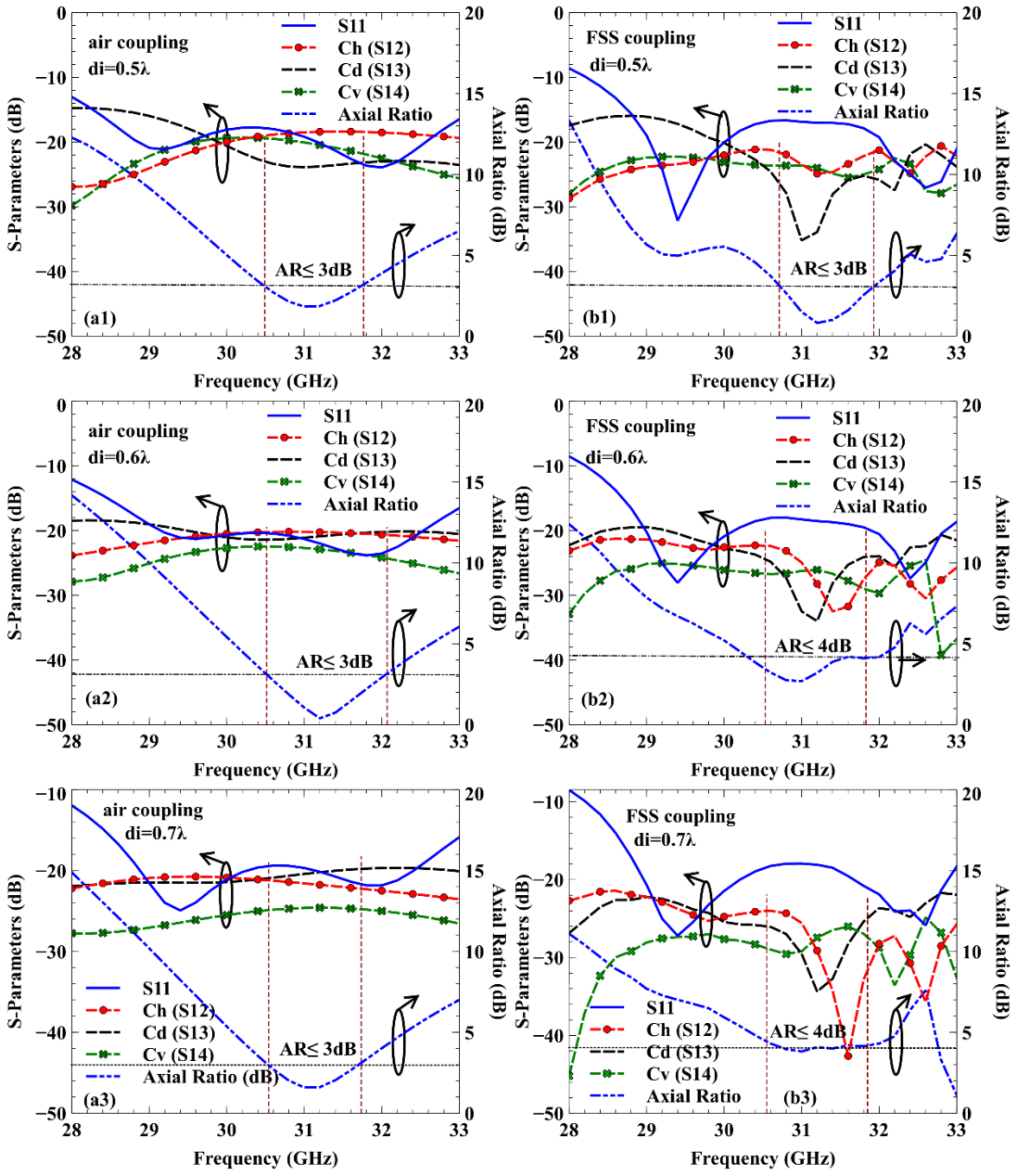

Figure 4-13: Simulated results of axial ratio and S-parameters for different cases of (a) Air coupling and (b) FSS coupling; including (a1) and (b1) (di = 0.5λ), (a2) and (b2) (di = 0.6λ), and (c1) and (c2) (di = 0.7λ).

It is seen that in the case of air coupling by varying antenna distance from 0.5λ to 0.7λ, the axial ratio magnitude has a negligible change without any frequency shift. However, the axial ratio is degraded in terms of magnitude and frequency shift when FSS layer is employed. It is believed that the air gap (2.5mm) between FSS element and MIMO antenna changes the phase of two

electric field components (E_θ , $E_\emptyset$). The left and right-hand fields and AR of the antenna were then calculated from the measured electric fields, with both amplitude and phase which is given as (3-14) to (3-16) [55]. Thus, in order to satisfy the requirement of the 3dB-axial ratio in the case of FSS coupling, the inter-element spacing 0.5λ has an acceptable response as compared with 0.6λ and 0.7λ spacing as shown in Figure 4-13 (a_2)-(c_2). It is worthwhile to mention that coupling reduction is higher when the inter-element spacing is considered 0.7λ in comparison to the other 0.5λ and 0.6λ spacing. However, the priority here is to maintain the 3dB-AR bandwidth and then coupling reduction. Table 4-1 summarizes the maximum coupling coefficients in the two cases of air and FSS couplings for different inter-element spacing values on the CP bandwidth.

Table 4-1: The maximum coupling coefficients on CP bandwidth

di	Without superstrate (air coupling) (dB)	With superstrate (FSS Coupling) (dB)
0.5λ	C_h=16 C_v=18 C_d=24	C_h=24 (AR≤3dB) C_v=24 C_d=36
0.6λ	C_h=20 C_v=24 C_d=20	C_h=32 (AR≤4dB) C_v=27 C_d=34
0.7λ	C_h=23 C_v=25 C_d=20	C_h=43 (AR≤4dB) C_v=30 C_d=34

As it is apparent, in spite of the further coupling suppression when the antenna distance is 0.7λ or 0.6λ, the CP bandwidth does not meet the AR≤3dB. Consequently, in order to satisfy the AR≤3dB, the inter-antenna spacing 0.5λ is considered for the implementation. The simulated electric field distribution for two cases of air and FSS couplings at 31.2 GHz using Ansys HFSS is shown in Figure 4-14. Note that the reason to select 31.2 GHz is that the best value of the axial ratio for both cases is obtained at that frequency. It can be found out that in the case of FSS coupling, the field leakage through adjacent antennas in the xz- and yz- planes is less than the one in the case of air coupling.

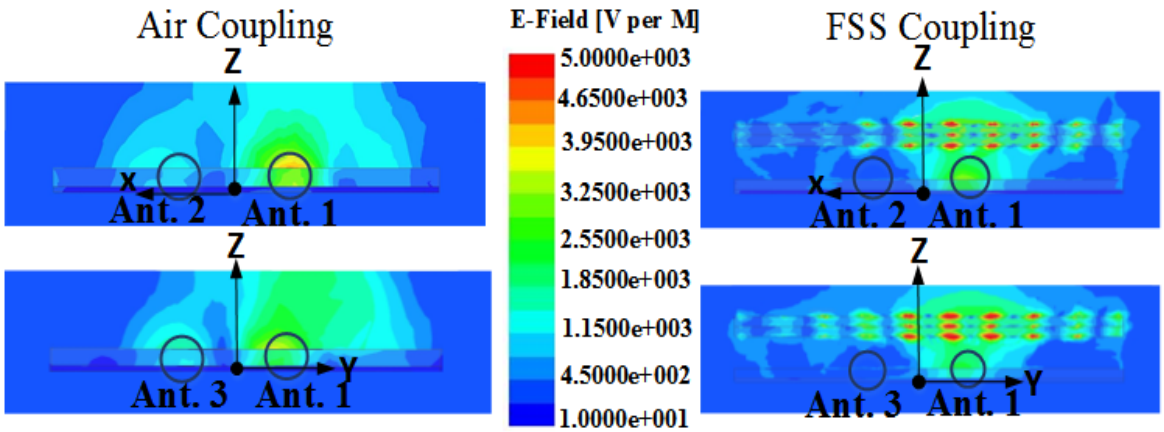

Figure 4-14: Simulated E-Field distribution on the 2×2 MIMO-ACMA for both cases air and FSS couplings in the xz- and yz- planes at frequency 31.2GHz.

4.1.5 Fabrication and Measurements

Finally, the proposed 2×2 MIMO-ACMA system with the inter-antenna spacing λ/2 for both cases of air and FSS coupling are fabricated and measured. The photographs of the implemented 2×2 MIMO-ACMA are shown in Figure 4-15. For the sake of comparison, the coupling coefficients without and with the FSS layers were measured. The coupling between 2×2 MIMO-ACMA is measured with a two-port Agilent N5227A PNA Network Analyzer (10MHz - 67GHz). For all structures, the coupling amounts are achieved by normalizing the experimental results with the radiated power [92]. Thus, the coupling coefficient can be expressed as [92]:

$$c(dB) = 10\log\left(\frac{|s_{21}|^2}{(1-|s_{11}|^2)(1-|s_{22}|^2)}\right) \tag{4-8}$$

Using (4-8) and the measured s-parameters, the coupling coefficients "C_h", "C_v", and "C_d" can be computed. The photography of the implemented structure and also the measurement setup are observed in Figure 4-16(a) and (b).

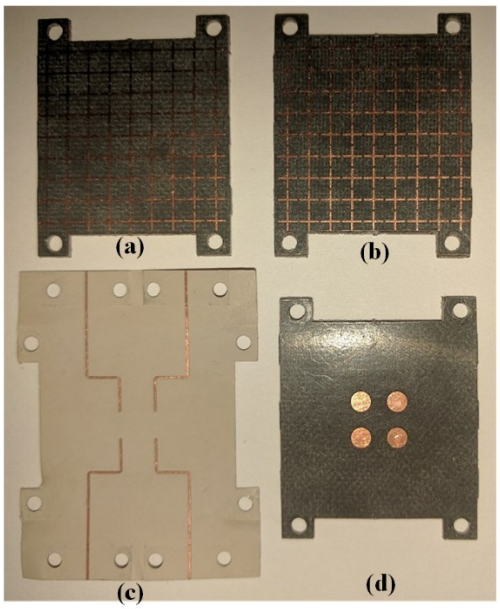

Figure 4-15: Photos of the fabricated 2×2 MIMO-ACMA: (a) and (b) FSS layers, (c) feedlines, and (d) patches.

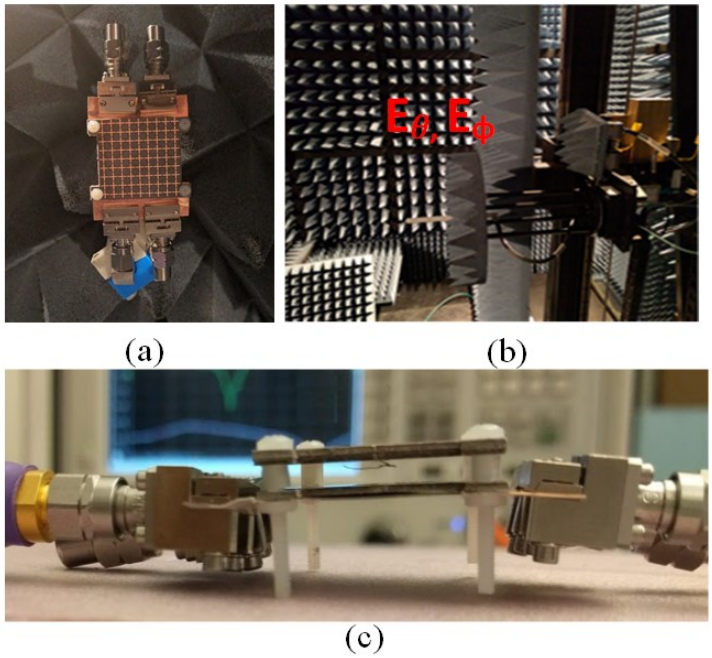

Figure 4-16: (a) The photography of the fabricated 2×2 CP-MIMO antennas under test as transmitter, (b) the photo of open-ended waveguide (NSI RF WR28) as receiver in the far-field anechoic chamber, and (c) side view of the proposed 2×2 MIMO-ACMA under test by network analyzer

A side view of the configuration is shown in Figure 4-16(c). It should be noted that the simulated results for the coupling coefficients S_{21}, S_{31}, and S_{41}, are computed directly using HFSS without applying (4-8). Figure 4-17 shows the simulated and experimental s-parameters and axial ratio for the proposed design for the two cases of air and FSS couplings.

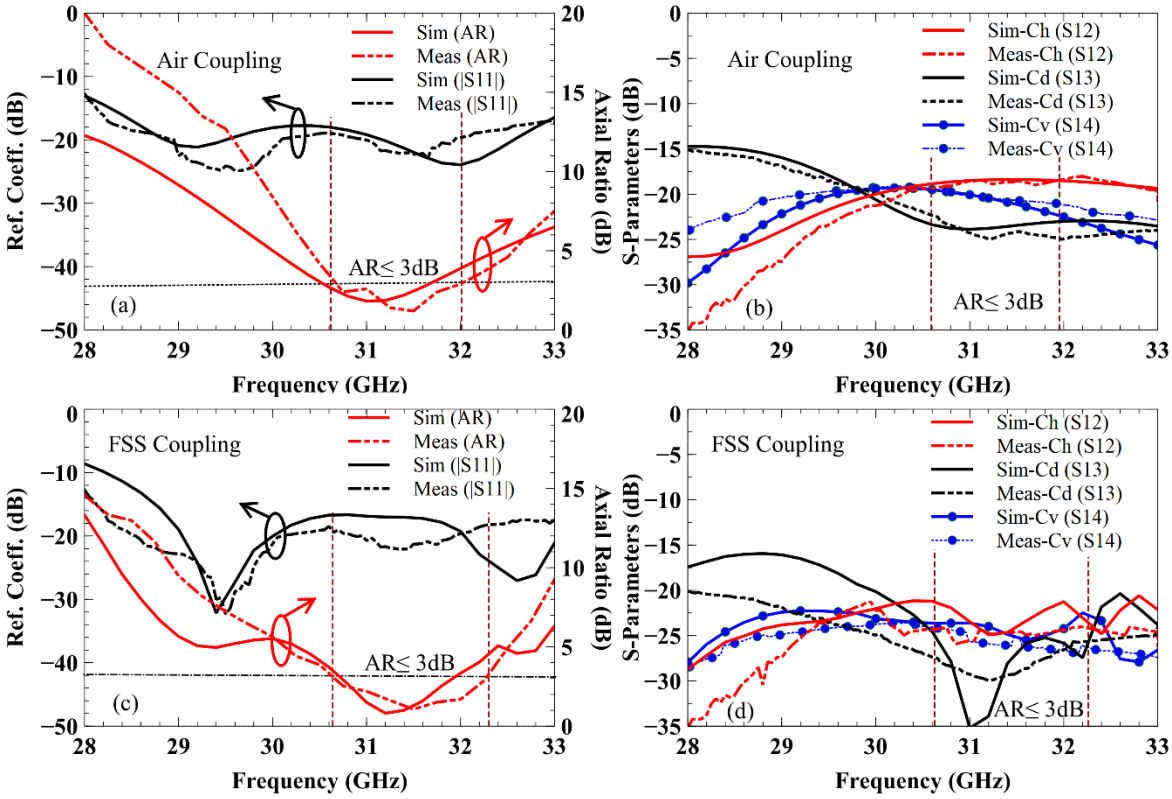

Figure 4-17: Measured and simulated results of axial ratio, reflection coefficient for different cases of (a) air and (c) FSS couplings, along with measured and simulated results of coupling for different cases of (b) air and (d) FSS couplings.

The measurements show an acceptable agreement with simulations. The highest values of measured coupling coefficients for the proposed structure in the absence and presence of the FSS superstrate on the CP bandwidth in three directions of horizontal, vertical, and diagonal are also summarized in Table 4-2. The same conclusion as before can be reached with the presence of FSS superstrate.

Table 4-2: The maximum amount of measured coupling coefficients on CP bandwidth

Without superstrate (air coupling) (dB)	With superstrate (FSS Coupling) (dB)
C_h = -18 C_v = -20 C_d = -24	C_h = -25 C_v = -26 C_d= -31

The isolation improvement in the diagonal direction is better than the ones in other directions. In addition, the coupling reduction in the horizontal and vertical directions approximately is the same. Figure 4-18 shows the effect of mutual coupling on the radiation performance of ACMA. The left-hand circularly polarized (LHCP) gain in the xz- and yz- planes were simulated using HFSS. The radiated patterns are also measured in the presence and absence the FSS superstrate at 31 GHz.

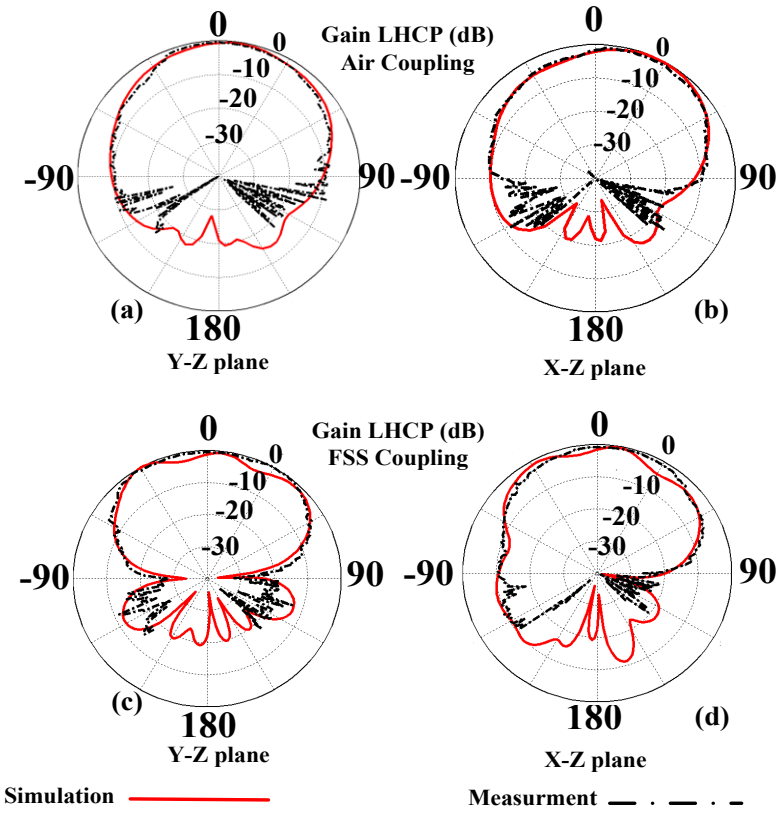

Figure 4-18: Measured and simulated LHCP gain for both cases of (a), (b) air coupling and (c), (d) FSS coupling in the yz- and xz- planes at frequency 31GHz.

As shown in Figure 4-18(a) and (b), when the ACMA elements are radiating in free space at 31 GHz, the radiation pattern is slightly tilted due to the spatially mutual coupling and the presence of the common ground plane. In addition, the reason for the 10° tilting in radiation pattern can be attributed to the design of FSS unit cell element under normal incident waves, while in the proposed integrated structure it is illuminated at oblique angles as shown in Figure 4-10. Furthermore, using FSS superstrate, the radiation pattern is slightly concentrated upward in the broadside direction, improving the antenna gain by about 1.5dB such that the FSS superstrate acted as a dielectric lens [66].

Spatially Coupling Reduction Using a FSS Polarization-Rotator Wall

An effective approach for suppressing the spatially coupling between DR antennas using a new FSS polarization-rotator wall is studied in this section of the thesis. The coupling reduction is achieved by embedding an FSS wall between two DRAs, which are placed in the H-plane. Utilizing this FSS wall, the TE modes of the antennas become orthogonal, which reduces the spatially coupling between the two DRAs. The wall is composed of 1 × 7 FSS cells along the E-plane. The mutual coupling is suppressed by greater than 16 dB on average (8 dB at 57 GHz, 22 dB at 60 GHz, 14 dB at 62 GHz) once the FSS wall is located between the DRA. The proposed FSS wall approximately has no influence on the DRA characteristics with respect to input impedance and radiation pattern. The radiation pattern is approximately unchanged compared to a DRA MIMO antenna array without FSS wall.

4.1.6 FSS Polarization Rotator Wall

The proposed wall comprises a periodic structure of FSS unit cell, as shown in Figure 4-19. It consists of a split-ring resonator (SRR) in one side, a coupling strip in the middle, and another SRR on the other side. The SRR is a common structure to obtain negative effective permeability and is used for designing metamaterials. The ring produces inductance, and the gap between the

rings produces capacitance. It also depicts a large magnetic dipole moment once excited by a magnetic field directed along its axis.

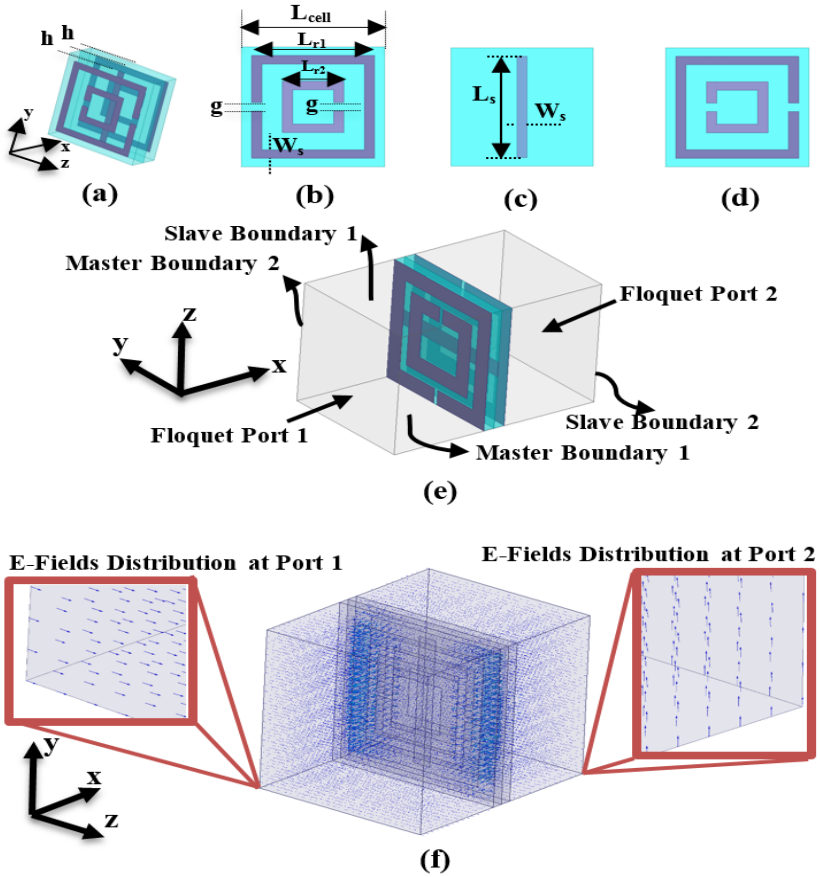

Figure 4-19: (a) Perspective view of the unit cell. (b) Metallic SRR-like on the top surface. (c) Metallic strip on the middle surface. (d) Metallic SRR-like on the bottom surface. (e) Specific boundary conditions d defined Floquet port excitation to extract scattering parameters. (f) E-fields distribution at 60 GHz. The dimensions are Lcell = 2, Lr 1 = 1.6, Lr 2 = 1, g = 0.05, Ws = 0.2, h = 0.127, and all in millimetre.

The coupling strip is used to rotate the E-field and to make the polarization of the two antennas orthogonal. Rotators of polarization and polarizers find their applications in microwave systems [97], [98], in which it is needed to vary the polarization of an EM wave. It is very common that a periodic structure of parallel wires or strips can rotate the polarization plane of an LP wave by a desired angle over a wide frequency band of interest. An LP wave can be regarded as a summation of two CP waves, one LHCP and RHCP, with the same amplitude. The FSS wall has different transmission phase for LHCP and RHCP incident waves. Therefore, the polarization plane of an LP wave will be rotated through the FSS wall once the transmission amplitude is the same for both LHCP and RHCP incident waves. The proposed FSS wall is embedded on the host

substrate Rogers RT5880 with the relative permittivity of 2.2. As depicted in Figure 4-19 (e), the bottom xy-plane is the first master boundary, and the top xy-plane is the correspondent slave boundary. Likewise, the xz-planes are the second correspondent master/slave boundaries. The Floquet port settings, under the specified boundary conditions [depicted in Figure 4-19 (e)], excite two plane waves with orthogonal electric fields such as TE(0,0) and TM(0,0) modes in the FSS wall plane. Moreover, higher order modes may also be specified in the port properties. The simulated co- and cross-polar coupling between the modes, both reflection and transmission, are given with respect to S-parameters in Figure 4-20. As exhibited in Figure 4-20, the FSS wall functions as a transmission layer with low insertion loss nearly 0 dB on a broad band.

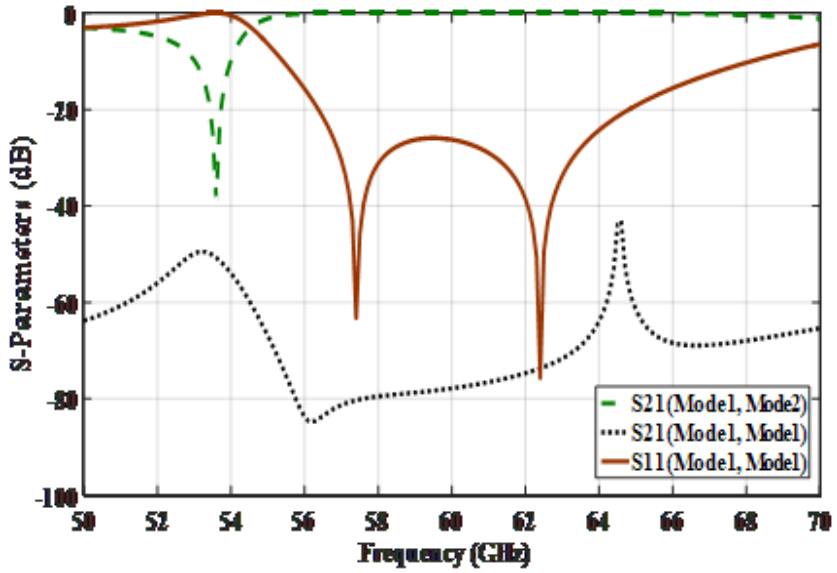

Figure 4-20: Transmission/reflection coefficients of the proposed MPR unit cell.

Although, the E-field rotates 90° through the FSS wall [see Figure 4-19 (f)] and makes the two DRA antennas orthogonal with respect to receiving the signal from each other. Thus, the FSS wall has a negligible influence on the DRA with respect to input impedance and radiation pattern. As it can be observed from Figure 4-20, the bandwidth of the FSS unit cell is about 12 GHz from 55 to 67 GHz.

4.1.7 MIMO Antenna with FSS Wall

The DR MIMO antenna array is designed based on reference [78]. The DR antenna is constructed by a cylindrical dielectric resonator with a relative permittivity of 10.2 (RT-6010). By exciting the DR antenna with a slot at the centre of the dielectric resonator, the fundamental mode $HEM_{11\delta}$ is excited. The configuration of 1×2 DR antenna array is arranged in the H-plane with a centre-to-centre distance of 2.5 mm corresponding to $\lambda_o/2$ at 60 GHz. To suppress the spatially coupling between the DR radiating elements, the FSS wall is placed between the two DRA, as shown in Figure 4-21.

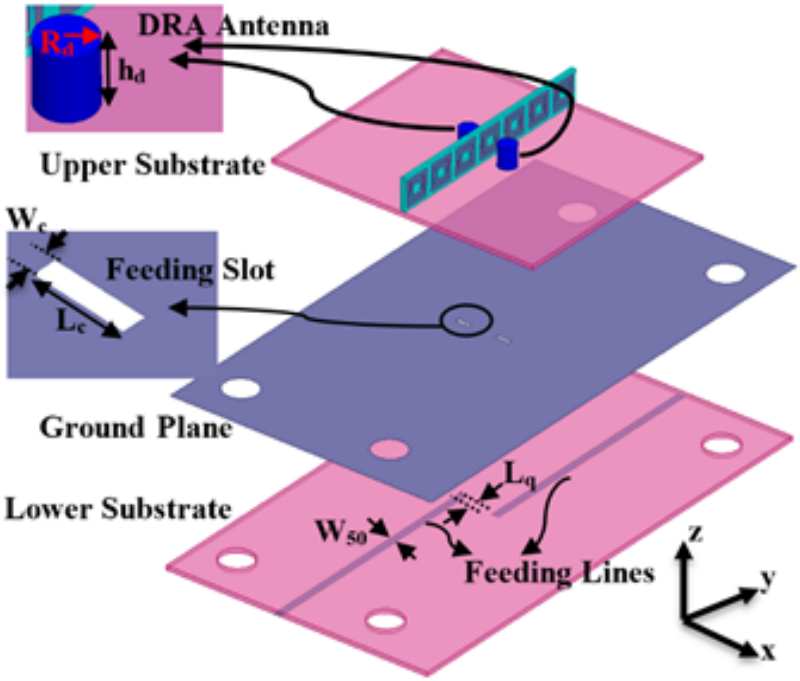

Figure 4-21: The layout of the 1×2 DR MIMO antenna with the FSS wall. The dimensions are Rd=0.53, hd=1.27, Wc=0.18, Lc=0.87, W50=0.41, Lq=0.3, and all in millimetre.

As it can be observed from Figure 4-21, the FSS wall is composed of 1×7 unit cells along the E-plane. The number of FSS cells is chosen through a parametric investigation. As it can be depicted from Figure 4-20, the FSS wall is matched over the desired frequency band (57-64 GHz). The spatially coupling reduction happens from the fact that the E-field rotates 90^o and makes the coupling between the two antennas orthogonal. The rotation of the E-field is exhibited in Figure 4-19 (f). Therefore, the two radiating elements are orthogonal, which yields coupling reduction between the DR antennas. Although, they have the same polarization with respect to

far-field radiation. Figure 4-22 depicts the scattering parameters of the antennas with and without FSS wall.

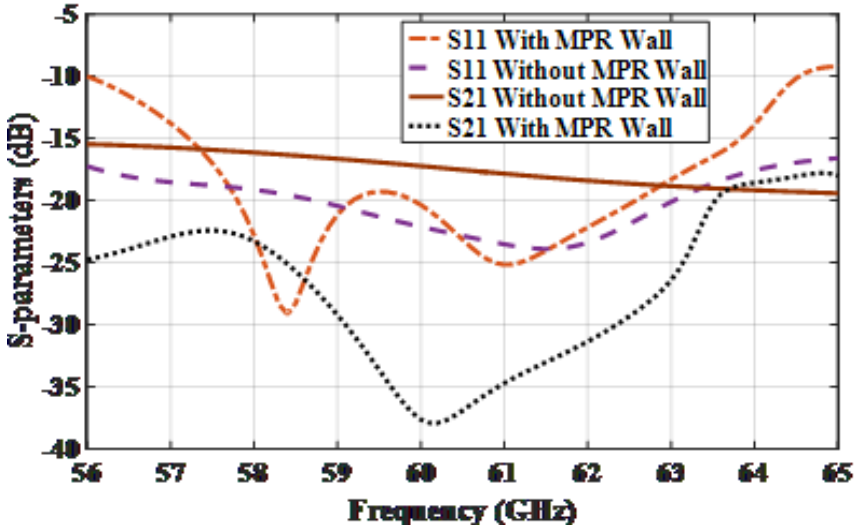

Figure 4-22: S-parameters simulation results of 1×2 DRA MIMO antennas with and without FSS wall between the two DR antennas.

As it can be observed from Figure 4-22, the spatially coupling is decreased by further than 16dB on average (8dB at 57GHz, 22dB at 60 GHz, 14dB at 62GHz). As compared to other techniques such as using EBG structures for blocking the surface waves [78], the use of the FSS wall does not affect the radiation pattern. The radiation pattern is nearly unchanged due to having an acceptable matched FSS wall (Figure 4-20). Table 4-3 compares the various techniques for reducing mutual coupling in literature.

4.1.8 Experimental Results

The MIMO antenna system with FSS wall was fabricated and measured. The measured coupling and reflection coefficient of the MIMO antenna system is depicted in Figure 4-23 (a). The photograph of the fabricated prototype is shown in Figure 4-24, and the measurement setup is shown in Figure 4-25. As it can be noted from Figure 4-22, the mutual coupling is reduced by more than 16 dB on average (8 dB at 57 GHz, 22 dB at 60 GHz, 14 dB at 62 GHz). Figure 4-23 (b) shows the normalized measured and simulated radiation patterns in the E- and H-planes at 60

GHz of the DRA, while the other element is matched. In Table 4-3, it is apparently indicated that the radiation pattern is tilted more than 30° in other approaches given in the literature [78], [94], [89]–[100]. It can be seen that the radiation pattern is not tilted in this work as compared to the MIMO antenna system without FSS wall.

Table 4-3 Comparisons to other decoupling structures

Reference	**Frequency Band**	**Average Mutual Coupling Reduction**	**Absolute MUTUAL COUPLING**			**Tilted beam (deg)**
			57 GHz	**60 GHz**	**64 GHz**	
[78]	57-64 GHz	13dB	-3dB	-10dB	0dB	30^o
[94]	4.06-4.095 GHz	10dB	-	-	-	36^o
[89]	5-7 GHz	14dB	-	-	-	27^o
[99]	57-64 GHz	14dB	-18dB	-15dB	0dB	33^o
[100]	57-64 GHz	15dB	-10dB	-13dB	-7dB	34^o
This WORK	57-64 GHz	16dB	-8dB	-22dB	0dB	Almost unchanged

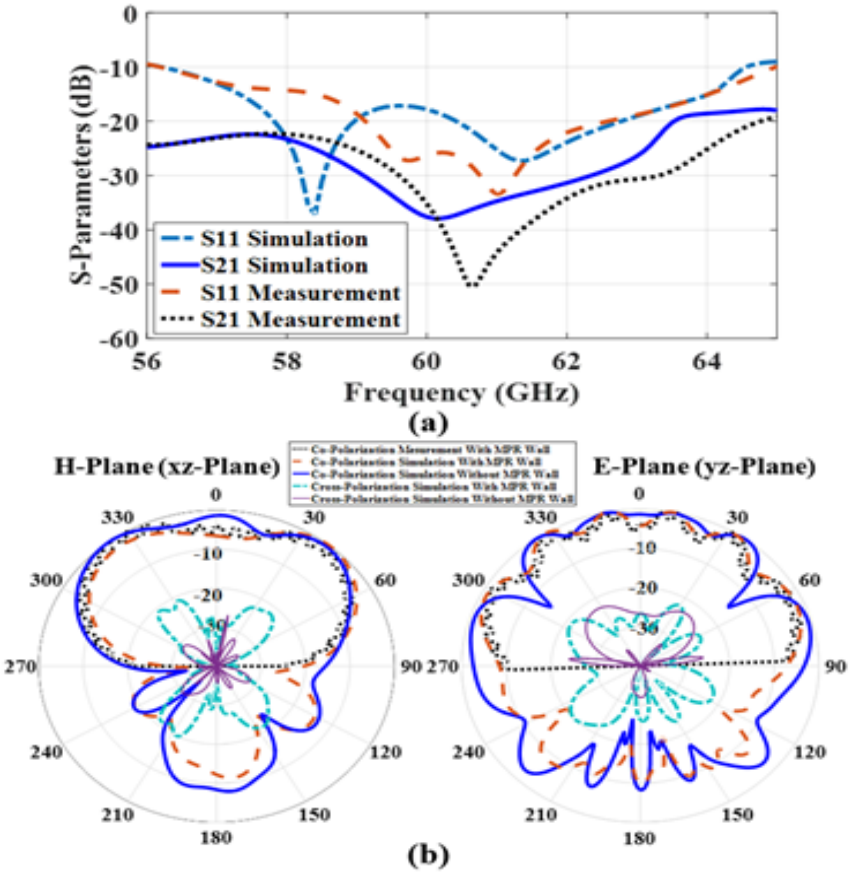

Figure 4-23: Simulated and measured results of 1 × 2 DRA MIMO antenna system with FSS wall between two radiating elements. (a) Scattering parameters. (b) Radiation pattern.

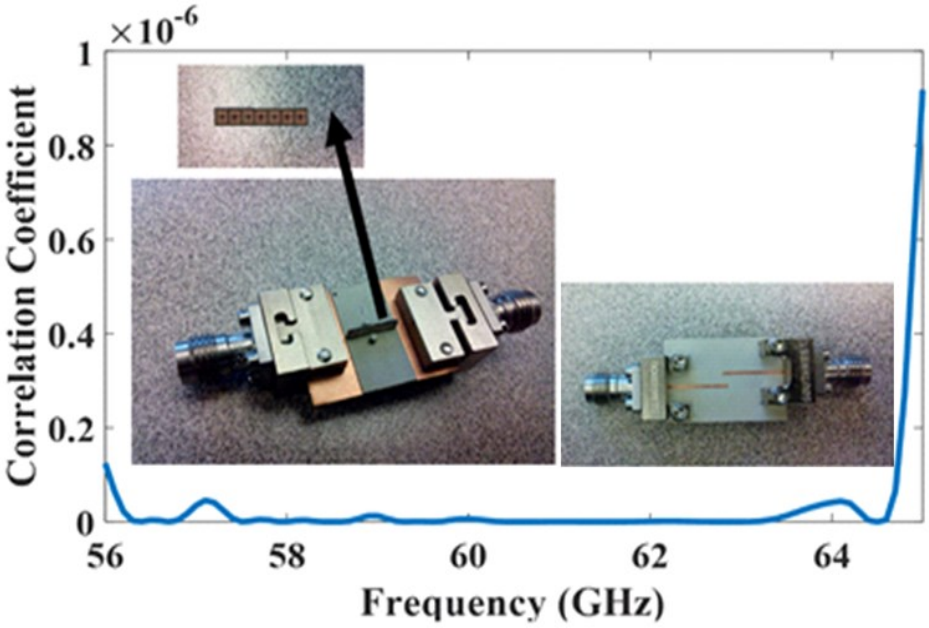

Figure 4-24: photograph of the proposed fabricated prototype.

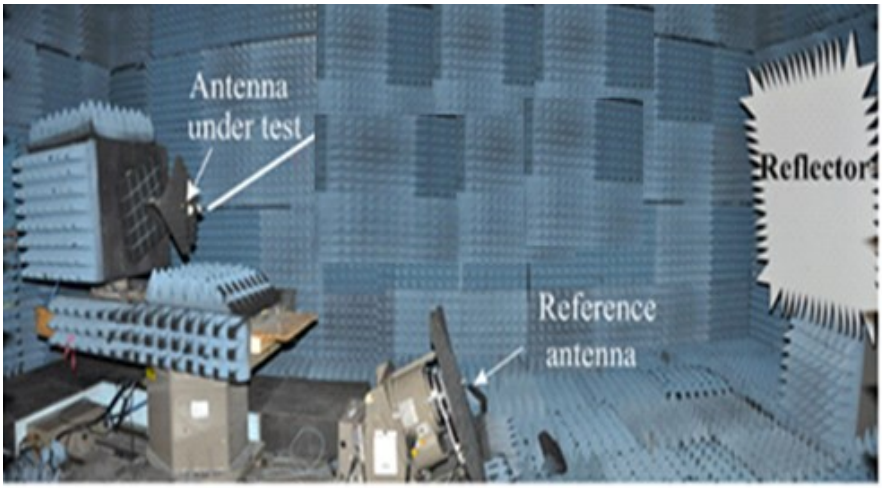

Figure 4-25: Radiation pattern measurement setup with receiving mode of the antenna under test.

Conclusion

As the first design in this chapter, an effective method for suppressing the near-field coupling between 2×2 CP-MIMO antennas around 30GHz has been presented. The suppression has been achieved by incorporating a two-layer transmission-type FSS superstrate. Due to the concentration of the power density using the FSS superstrate, enhancement in the structure gain and improvement in isolation have been achieved. The main disadvantage of this method is the partial reflection of power density from the FSS elements because the antenna illuminates each FSS element in different oblique incidence angles. The FSS unit cells are considered as a uniform planar array scattering back a small portion of the power density through the radiating antennas. In order to address this disadvantage, the reflected power density in the near-field area, when the FSS elements are illuminated by the antennas, has been studied. It is found out that by adjusting few design parameters such as the inter-antenna spacing or air gap, the insignificant reflections can be redirected far from the main beam direction to prevent any interference. However, by varying the air gap spacing, the CP bandwidth may be slightly varied due to variations in the phases of the electric field components (E_θ , $E_\emptyset$). The study has also compared the mutual coupling between CP-MIMO antennas when the patches are radiating in the air and in the presence of the FSS layers. In order to validate the simulation results, the proposed structures with an inter-antenna spacing of 0.5λ have been implemented and measured. The measured

results indicate when the FSS layers are employed, an average coupling suppression of 6 to 7dB on the 3dB-AR bandwidth has been achieved.

As the second design in this chapter, an FSS wall for reducing the mutual coupling between two DR antennas in a MIMO system has been designed and represented. The proposed FSS wall has been used to suppress the spatially coupling between two adjacent DR antennas. It provides broadband operation and low insertion loss for incident waves. The guidelines for designing the DR antenna and FSS unit cell have been discussed in details. The investigation has depicted that the proposed FSS wall has the capability to enhance the isolation between the radiating elements without disturbing the performances of the DR antennas with respect to radiation pattern and input impedance. The radiation pattern is approximately unchanged as compared to the antenna without FSS wall.

Chapter 5. Linear to Circular Polarizer Based on Multilayer FSS Slab

In this chapter, an LP-to-CP-polarizer based on multilayer FSS slab in Ka-band is presented. In order to improve impedance matching, metallic circular traces are printed periodically on each dielectric multilayer slab. Simulated results of the polarizer show that it can transform LP to CP fields over a frequency band from 23 GHz to 35 GHz (42%) with an insertion loss less than 0.5dB. The transmitted CP wave by the polarizer is approximately robust under oblique illuminations. The polarizer is fabricated and measured by a wideband horn antenna satisfying the simulated results. Then, to design a high-gain circularly polarized structure around 30 GHz, an 8-element LP array antenna with Chebyshev tapered distribution is designed and integrated with the polarizer. Obviously, the antenna limits the overall bandwidth (nearly 28 GHz to 31.5 GHz) due to the narrowband nature of the LP antenna array. When the polarizer is illuminated by an incident LP wave, the two linear components of the transmitted wave with approximately equal amplitudes and 90° phase difference on the frequency band of interest are produced.

Introduction

In antenna design, the select of the polarization of the radiated wave generally depends on the application as well as the propagation environment. Namely, in satellite communications or navigation systems, CP waves are demanded because of the benefits such as lower sensitivity to multipath fading and reduced sensitivity to Faraday rotation or the orientation of the receiver's antenna [8-10], [103]. In communication systems involving satellite-earth links, an LP wave experiences an unpredictable rotation as it propagates through the ionosphere. This rotation may cause polarization mismatch at the receiver that impacts the link budget of the system [103]. On the other hand, CP waves do not suffer from these matters and have been utilized in modern satellite and point-to-point communication systems to enhance the polarization efficiency and propagation link budget. A polarizer is a slab of an anisotropic medium that converts an incident wave with a given polarization to a reflected or a transmitted wave with a different polarization (e.g., LP to CP or vertical to horizontal). Planar polarizers are generally implemented utilizing FSS. These designs operate relied on decomposing a wave into two orthogonal components and yielding a 90◦ phase difference between them. A simple implementation for such a polarizer is a reactive surface having inductive impedance for one component of the field and capacitive impedance for the other. This way, a phase shift of 90◦ may be obtained between the two components of the emerging transmitted wave. If these two components have equal amplitudes, the incident LP wave will be transformed to a transmitted CP wave at the output [103]. A transmission-type polarizer has been extensively investigated by researchers in the

open literature for several applications [102-109]. For example, some polarizers were designed utilizing FSS structures [102-105], and others are based on traditional hybrid meander line and loop configuration [106-108]. In [102] a multilayer FSS was designed using square patches with truncated corners to obtain 90° phase difference between orthogonal linear components. The polarizer presented in [103] employs a miniaturized-element FSS composed of arrays of subwavelength capacitive patches and inductive wire grids separated by dielectric substrates. The polarizer in [104] uses a double-sided partially reflective surface (PRS), which controls independently the reflection and transmission coefficients. The work in [105] proposed a CP converter utilizing a four-layer FSS consists of split rings bisected by a metal strip, in which distance between different layers is a quarter wavelength, but the layers' dimensions are different. Despite structures suggested in [102-105] are broad band, they consist of multilayer structures with different configurations and dimensions for each layer, ending up with complicated geometry and configuration for the polarizers. In [107] single layer polarizer based on hybrid meander line and loop geometry are proposed. This structure can cover the AR bandwidth of 46.8%. However, the peak insertion loss is 3dB. In order to achieve a CP in [108], a meander line polarizer has been employed with the linear SIW antenna, while the structure does not have broadband behaviour. Another approach used in [109] included rotating FSS structure that was implemented using the substrate integrated waveguide (SIW) technology.

In this thesis, a transmission–type polarizer based on multilayer dielectric structure to transform LP incident EM wave into a CP transmitted wave is proposed. To simplify the structure, a unit cell is utilized in all dielectric layers. Moreover, to illuminate the polarizer, an 8-element linearly polarized linear array antenna with Chebyshev tapered distribution to control the radiated pattern side lobe level (SLL) is also designed. In the configuration, the antenna is placed at a half free space wavelength from the polarizer with a 45° rotation. The size of the polarizer is determined using a diffraction and transmission rays' model.

Theoretical Analysis

In this section, we consider the theoretical analysis of the polarizer. Figure 5-1 exhibits the topology of the polarizer which converts linearly polarized EM wave into a circular one. Let us consider an incoming plane wave that propagates in the +z direction, whose incident and transmitted electric fields can be expressed as [113]

$$E^{inc}(x,y,z,t) = \begin{pmatrix} E_x^{inc} \\ E_y^{inc} \end{pmatrix} e^{i(kz-wt)} \tag{5-1}$$

where ω, k, E_x, and E_y are the frequency, wave number, and the complex amplitudes of x- and y- electric

field components, respectively [125].

$$E^{tr}(x,y,z,t)=\begin{pmatrix}E_x^{tr}\\E_y^{tr}\end{pmatrix}e^{i(kz-wt)} \tag{5-2}$$

To further realize the polarization conversion of the polarizer, the transmission coefficient T.C. is defined as:

$$T.C.=\frac{E^{tr}}{E^{inc}} \tag{5-3}$$

The linear transmission matrix can be expressed as [125]

$$\begin{pmatrix}E_x^{tr}\\E_y^{tr}\end{pmatrix}=(T.C.)_{Linear}\begin{pmatrix}E_x^{inc}\\E_y^{inc}\end{pmatrix}=\begin{pmatrix}T_{XX} & T_{XY}\\T_{YX} & T_{YY}\end{pmatrix}\begin{pmatrix}E_x^{inc}\\E_y^{inc}\end{pmatrix} \tag{5-4}$$

Thus, the circularly polarized transmitted EM wave can be defined as [125]:

$$\begin{pmatrix}E_{RHCP}^{tr}\\E_{LHCP}^{tr}\end{pmatrix}=\begin{pmatrix}E_x^{tr}+jE_y^{tr}\\E_x^{tr}-jE_y^{tr}\end{pmatrix}=(T.C.)_{Circular}\begin{pmatrix}E_x^{inc}\\E_y^{inc}\end{pmatrix} \tag{5-5}$$

$$(T.C.)_{Circular}=\begin{pmatrix}T_{RHCP\_X} & T_{RHCP\_Y}\\T_{LHCP\_X} & T_{LHCP\_Y}\end{pmatrix}=\frac{1}{\sqrt{2}}\begin{pmatrix}T_{XX}+jT_{YX} & T_{XY}+jT_{YY}\\T_{XX}-jT_{YX} & T_{XY}-jT_{YY}\end{pmatrix} \tag{5-6}$$

where the factor $\frac{1}{\sqrt{2}}$ in (5-6) is due to power normalization. The matrix in (5-6) states the ability of the polarizer to convert an LP electromagnetic wave into a CP one.

Polarizer Design

The schematic model of the multilayer dielectric LP to CP polarizer is shown in Figure 5-1.

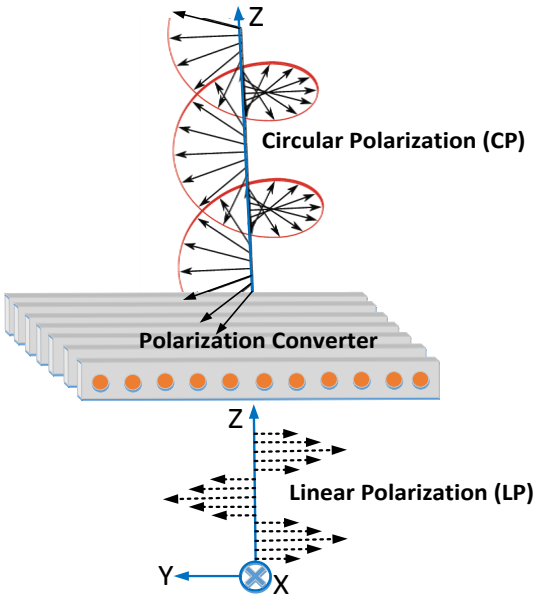

Figure 5-1: Schematic model of a linear-to-circular polarizer.

The polarizer is illuminated by a planar LP electromagnetic wave propagating in the k direction and tilted away from the x-axis by 45°. Therefore, the electric field is decomposed into two orthogonal components: the former along the x-axis and the latter along the y-axis. Figure 5-2 exhibits the unit cell model simulated by ANSYS HFSS™.

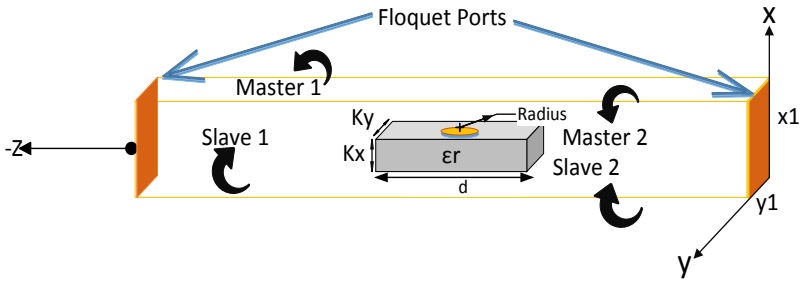

Figure 5-2: The unit cell model by HFSS software (x1=1.6mm, y1=1mm, d=4.6mm, kx=0.254mm, ky=1mm, εr=10.2, Radius=0.3mm)

The unit cell consists of two Floquet ports in distance of one wavelength (λ) far from the dielectric with constant ε_r=10.2 and thickness k_x=0.254mm. The width and length of the dielectric piece are ky=1mm and d=4.6mm, respectively. The radius of the metal circle is 0.3mm. In addition, the method applied in the unit cell model is the periodic boundary conditions of the Master/Slave in order to evaluate the infinite structure. Both Floquet ports contain two dominant modes with two orthogonal waves along x- and y-axis. The main idea of the LP-to-CP polarizer and simulation model has come from references [112], [115]-[116]. In order to study a fundamental theory for multilayer dielectric slabs, Figure 5-3 is presented.

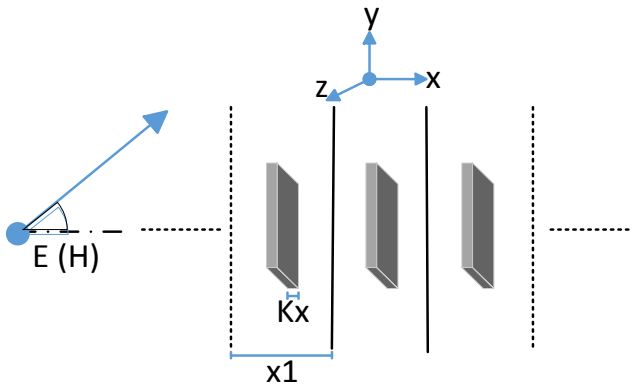

Figure 5-3: One dimensional lattice of dielectric slabs of width kx in a periodic lattice with period x1

A representative one-dimensional periodic array of dielectric slabs with period x_1 and dielectric insert width K_x is depicted in Figure 5-3. If the electric field does not have a component in the x –direction, the mode is denoted TE_x or horizontal. If the magnetic field does not have a component in the x -direction, the mode is denoted TM_x or vertical. The effective dielectric constants given in two directions by the volumetric average of the constitutive phases are [117]-[118].

$$\varepsilon_{rx} = \begin{cases} \varepsilon_r, & \dfrac{-k_x}{2} \le x \le \dfrac{k_x}{2} \\ 1, & otherwise \end{cases} \qquad (5\text{-}7)$$

$$\varepsilon_{ry} = \left[1 + (\varepsilon_{rx} - 1) \frac{k_x}{x_1} \right] \tag{5-8}$$

From (5-7) and (5-8) it can be noted that the effective dielectric constant in y-direction depends on $\frac{k_x}{X_1}$, while the x-directed component has a constant value close to 1. Therefore, due to the existence of the periodic dielectric slabs, a phase difference happens between the E-field orthogonal components when the incident EM wave transmits through the LP-to-CP polarizer. The phase difference is estimated as:

$$\Delta\varphi = \left(\beta_y - \beta_x \right) d = \frac{2\pi}{\lambda} \left(\sqrt{\varepsilon_{ry}} - \sqrt{\varepsilon_{rx}} \right) d \tag{5-9}$$

where λ, β are the wavelength and phase constant, respectively. The phase difference between the E-field orthogonal components is tuned using a length parameter d, as shown in Figure 5-2. In order to satisfy the CP requirement in (5-9), the phase difference must be $\frac{\pi}{2}$, therefore

$$d = \left(\frac{\lambda}{4\left(\sqrt{\varepsilon_{ry}} - \sqrt{\varepsilon_{rx}} \right)} \right) \tag{5-10}$$

The dielectric multilayer slab characteristics at a resonant frequency (f_r) are governed by (5-7) through (5-10), in which ε_{rx} can be estimated to 1. Thus, at 30 GHz with dielectric constant 10.2, thickness kx=0.254mm, and the periodic distance between slabs x_1 =1.6mm, d =4.6mm is obtained.

Simulation Results of Polarizer

5.1.1 Reflection and Transmission Coefficients

In order to investigate and verify the polarizer performance, a full-wave simulation is carried out using Ansys HFSS-15. Initially, the dielectric multilayer slabs with numerical values obtained from (5-7) to (5-

10) are simulated. The magnitude and phase of transmission coefficients are presented in Figure 5-4 (a) and (b), respectively. It can be noticed that the cross-transmission coefficients Tr(xy) and Tr(yx) are nearly zero. Concerning the reflection coefficient curve depicted in Figure 5-4 (c), there are two resonant frequencies at about 21GHz and 41GHz. Figure 5-4 (d) shows the magnitude and phase differences between transmission coefficients for both polarizations (xx and yy).

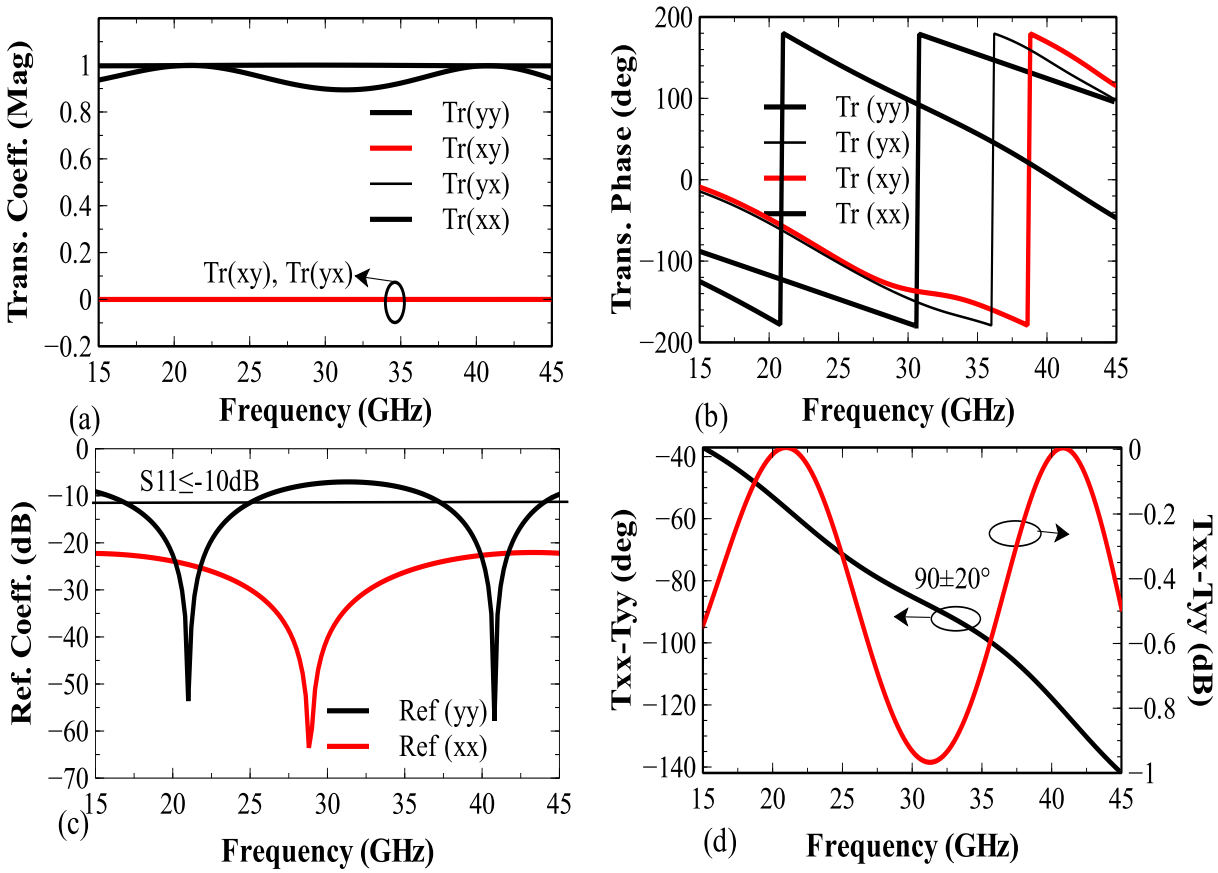

Figure 5-4: The simulated of transmission coefficients of dielectric slab without the conductor in unit cell model (a) magnitude of transmission coefficients, (b) phase of transmission coefficients, (c) reflection coefficient, and (d) difference of phase and magnitude between transmission coefficients

It is observed that the phase difference (90±20°) and magnitude difference (less than 1dB) of transmission coefficients for both polarizations remain between 24GHz to 38GHz (45%). In terms of design simplicity without any conductors, the dielectric multilayer slabs can be a good polarizer candidate. However, the -10 dB impedance bandwidth is very limited. In order to satisfy the standard impedance bandwidth (S_{11}≤-10dB), a circular conductor, due to its shape simplicity, is printed on one side of each dielectric slab. The circular conductor gives the designer freedom to achieve the desired impedance bandwidth. The dependence of transmission and reflection coefficients of the dielectric slab on the radius of the integrated

circular conductor are given in Figure 5-5. A conducting circle with radius 0.3mm is chosen as a reasonable value. Finally, the simulated transmission and reflection coefficients of the proposed polarizer with the conductor in the unit cell model are depicted in Figure 5- 6. It is obvious that the dielectric slab with a circular conductor has the same behaviour in transmission coefficient curves in comparison with the dielectric slab without the conducting circle.

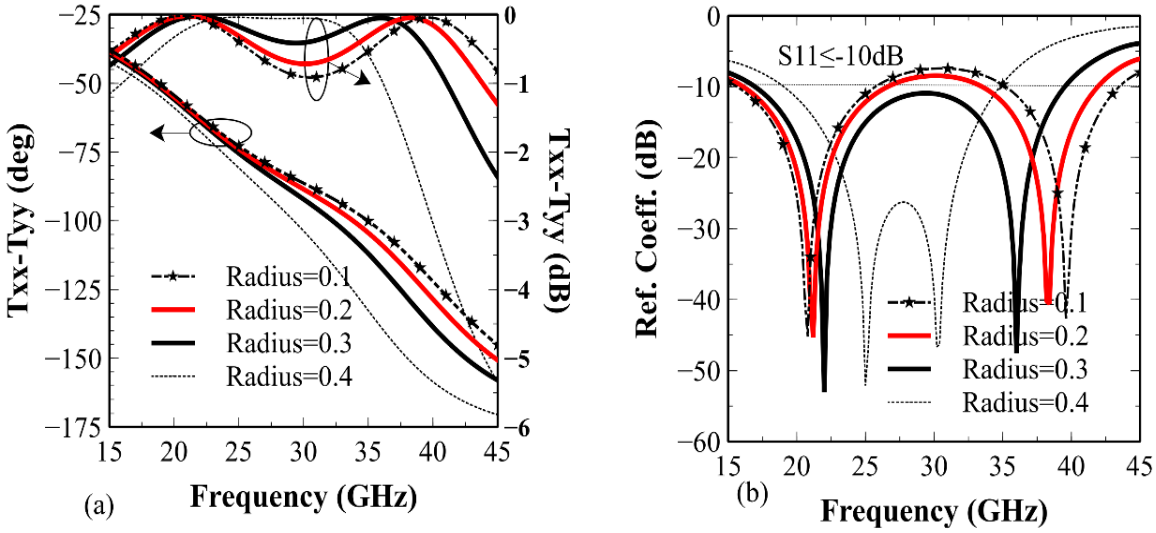

Figure 5-5: (a) variations of transmission coefficients and (b) reflection coefficients in the unit cell model when the radius of the circle conductor changes

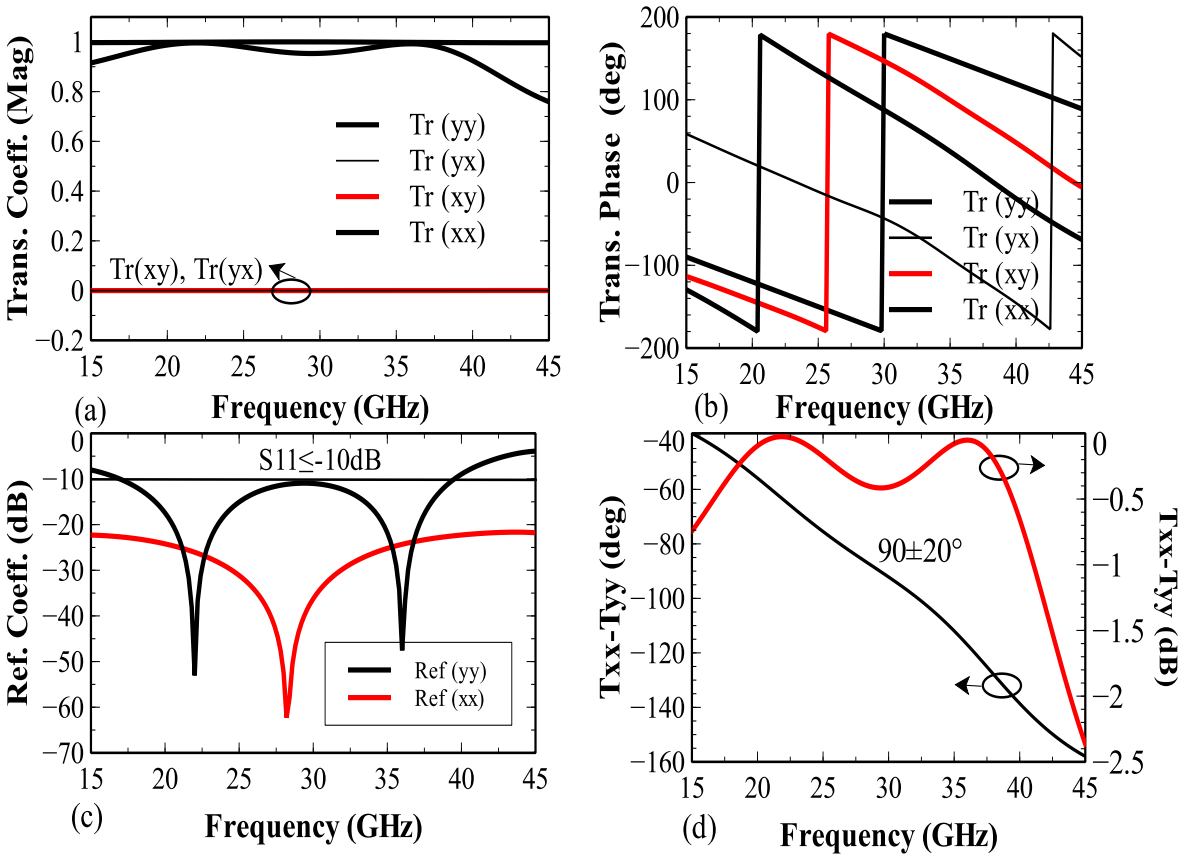

Figure 5-6: The simulated of transmission coefficients of dielectric slab with the conductor in unit cell model (a) magnitude of transmission coefficients, (b) phase of transmission coefficients, (c) reflection coefficient, and (d) difference of phase and magnitude between transmission coefficients

The main improvement is observed in the bandwidth of reflection coefficient (S_{11}≤-10dB), where it covers the frequency band 22.5GHz to 40GHz (56%). However, the phase difference of transmission coefficients (90±20°) limits the frequency band from 23GHz to 35GHz (42%). All obtained results are based on normal incident EM wave when the LP wave is titled away from the x-axis by 45°. Practically, the incident wave can be oblique or deflected due to the type of radiation pattern of antenna or installation inaccuracy. Therefore, the robustness of the polarizer under oblique incidence wave must be examined as well. As illustrated in Figure 5-7, it is observed that the broad -10dB impedance bandwidth is still maintained up to an oblique angle of 30°. It is also found out that by varying the incident wave angle, the transmission performance is approximately stable.

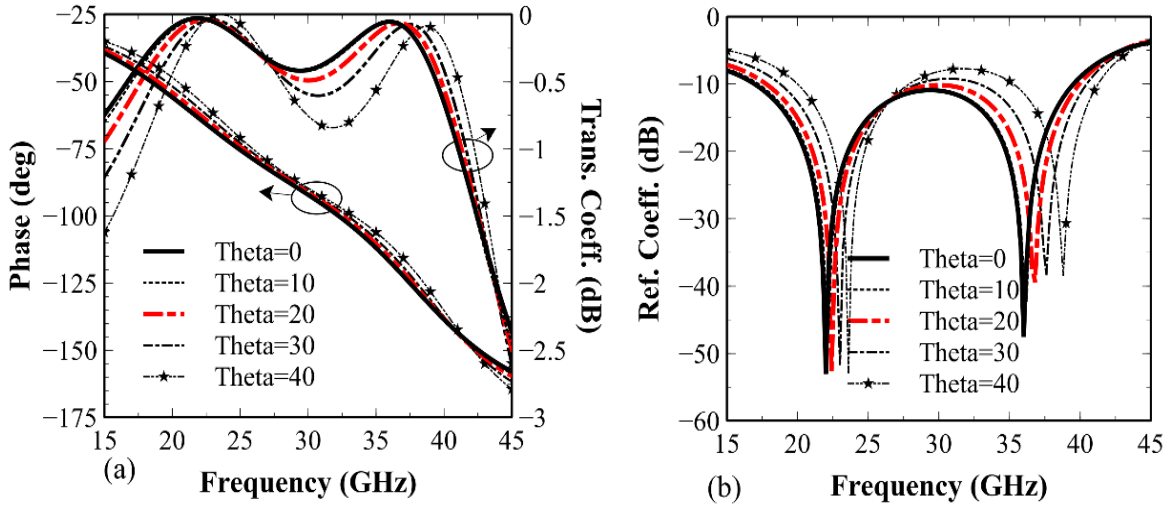

Figure 5-7: The results related to the dielectric slab with circle conductor in the unit cell model when is illuminated by an incident wave with different oblique angles (a) magnitude and phase of transmission coefficients, (b) reflection coefficients

5.1.2 Dielectric Multilayer Slabs Arrangement

One of the challenges in designing multilayer structures as superstrate (placed above the radiating sources) is to specify the number of layers and estimate the size of the superstrate. To address this challenge, the model of diffraction and transmission ray is shown in Figure 5-8 [66]. Where β and θ are the alevation angles from the radiation centre to edge of the superstrate and rays 2, respectively. This technique is useful for circular layers, but it can also give a good estimation of square shape layers. In this model, the phase of diffraction and transmission rays radiated from the antenna source to dielectric multilayer slabs should be equal.

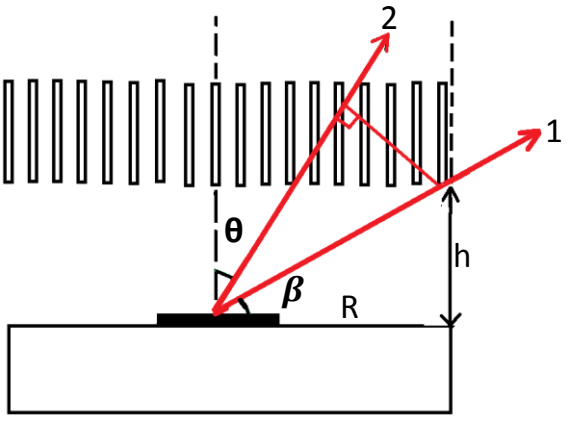

Figure 5-8: Model of the diffraction and transmission rays [66].

In Figure 5-8, rays 1 and 2 are the first diffraction and transmission with phases 1 and 2, respectively. Since the wave phase is defined as

$$\varphi = e^{-j\beta d} = e^{-j\left(\frac{2\pi\sqrt{\varepsilon_r}}{\lambda}d\right)} \tag{5-11}$$

Therefore, with respect to Figure 5-8, we have

$$\varphi_1 = e^{-j\left(\frac{2\pi h}{\lambda \sin\beta}\right)} \tag{5-12}$$

$$\varphi_2 = e^{-j\left(\frac{2\pi h\cos(\frac{\pi}{2}-\beta-\theta)}{\lambda\sin\beta}+\varphi_t\right)} \tag{5-13}$$

In order to keep the diffraction and transmission rays in phase, we impose the following conditions,

$$\frac{2\pi h}{\lambda\sin\beta} = \frac{2\pi h\cos(\frac{\pi}{2}-\beta-\theta)}{\lambda\sin\beta}+\varphi_t \tag{5-14}$$

Note that, here, "θ" is supposed to be so small, hence (5-14) can be evaluated as

$$\frac{h}{\lambda}(\frac{1}{\sin\beta}-1)-\frac{(\varphi_t)}{2\pi} = N \tag{5-15}$$

The proposed polarizer involves the transmission phase ϕ_t in x- and y- polarization, which are 179.7° and 87.5°, respectively. In order to have the minimum size of the polarizer, "N" should be a positive integer. The elevation angle β from the antenna source to the edge of the polarizer, for the two aforementioned directions, is computed as 15° and 17°, respectively, resulting in an ellipse with major and minor axes of 37mm and 33.4mm. Based on the diffraction and transmission rays' model, the size of the proposed dielectric slab as exhibited in Figure 5-2 is 33×25 unit cells. It means that the proposed polarizer consists of 33 circular conductors which are linearly printed on each of the 25 dielectric layers.

5.1.3 Position of the Transmitted Wave Polarization

In order to investigate the purity of transmitted wave CP, the polarization azimuth angle ψ, and ellipticity angle χ are used to examine the orientation and case of the elliptical polarization, as shown in Figure 5-9. The parameter ψ specifies the angle between the major axis of the ellipse and the x-axis, while the angle χ examines the ellipticity behaviour.

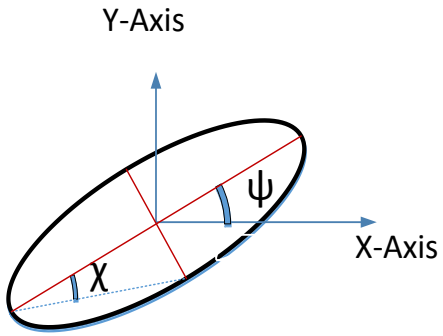

Figure 5-9: The polarization ellipse with two angles shown ψ and χ as the geometrical parameters of the ellipse

The angles ψ and χ can be calculated from the following equations [119]:

$$\Delta\varphi = \varphi_{yy} - \varphi_{xx} \tag{5-17}$$

$$\psi = \frac{1}{2}\left(\tan^{-1}\left[\frac{2r}{1-r^2}\right]\cos\Delta\varphi\right) \tag{5-18}$$

$$\chi = \frac{1}{2}\left(\sin^{-1}\left[\frac{2r}{1+r^2}\right]\sin\Delta\varphi\right) \tag{5-19}$$

where "r" in (5-16) is the amplitude ratio. As shown in in Figure 5-10 (a), the variations of polarization azimuth angle (ψ) and ellipticity angle (χ) of the transmitted wave with frequency are highlighted. Whenever the ellipticity angle of the transmitted wave is $\pm$45°, it means that polarization is purely circular. Correspondingly, the ellipticity angle of the transmitted wave in the proposed polarizer is -45° at around 30GHz, indicating the pure CP at the frequencies close to 30GHz, as shown in Figure 5-10. To further

understand the tendency of the polarization ellipses and its dependence on the frequency, sixteen uniformly distributed frequencies along the bandwidth were selected. The corresponding results are shown in Figure 5-11. It can be noticed that by increasing the frequency from 25GHz to 40 GHz, the polarization is right hand rotated. Also, as an acceptable estimation, it is observed that when the ellipticity angle (χ) corresponds to -45±5°, an excellent CP from 26GHz to 33GHz is obtained. However, an elliptical polarization is observed in the rest of the frequency band. It is expected that the distortions in the circular polarization at the edges of the band are mainly caused by elevated reflections.

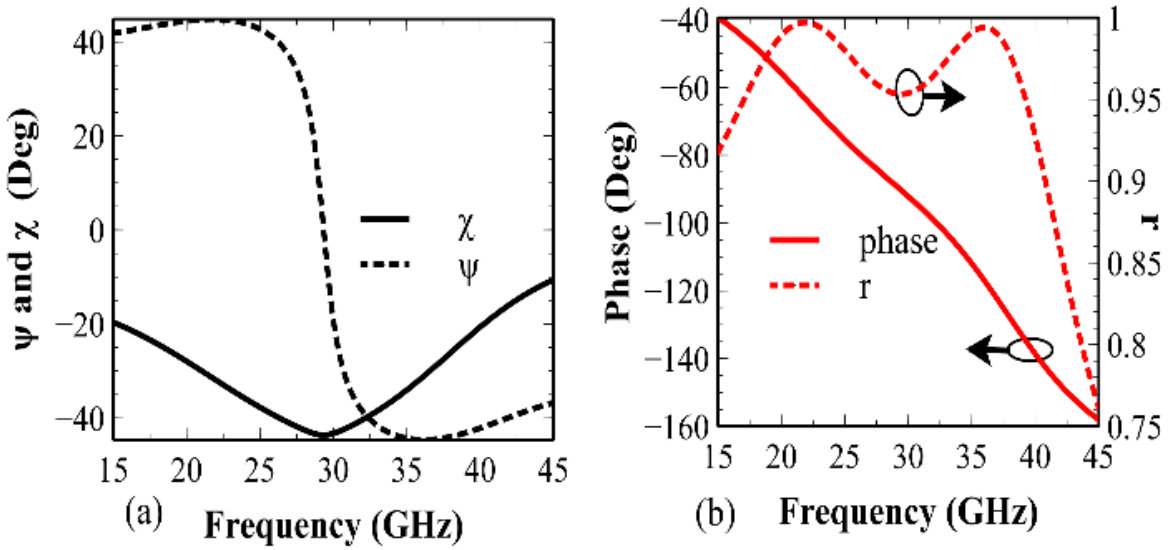

Figure 5-10: (a) The simulated angles of polarization azimuth (ψ) and ellipticity (χ) and (b) the phase difference ($\Delta\phi$) and amplitude ratio (r) versus frequency

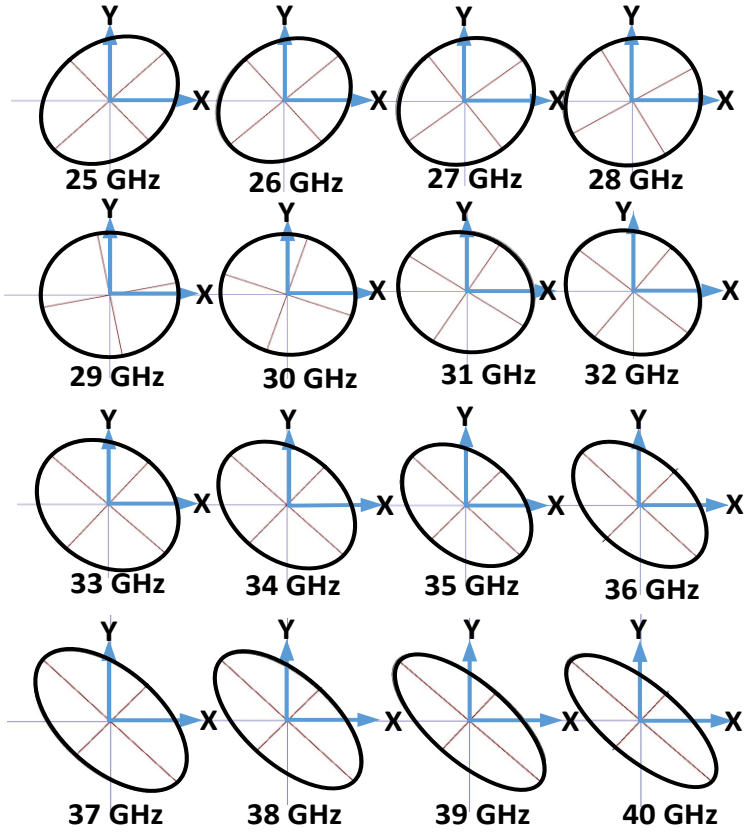

Figure 5-11: Theoretically predicted polarization cases in the plane perpendicular to the wave vector at different frequencies from 25GHz to 40 GHz.

Table 5-1 summarized a brief comparison between the proposed design and sample published polarizers in literature in terms of 3-dB AR bandwidth and maximum insertion loss in the band of interest. According to the table, the proposed design has a better performance compared to other structures, particularly in the insertion loss performance.

Table 5-1: Performance comparison of our proposed design wih deign in the literature

Year/ Ref.	**Design**	**3-dB AR (BW) (%)**	**Peak Insertion loss (dB)**
2016/ [103]	anisotropic FSS	40	≤ 3
2012/ [106]	Meander line and stub	36	1
2011/ [120]	Cross slot	14.5	3.2
2011/ [120]	Split circular ring FSS	21	3.3
Proposed	FSS slab	42	≤ 0.5

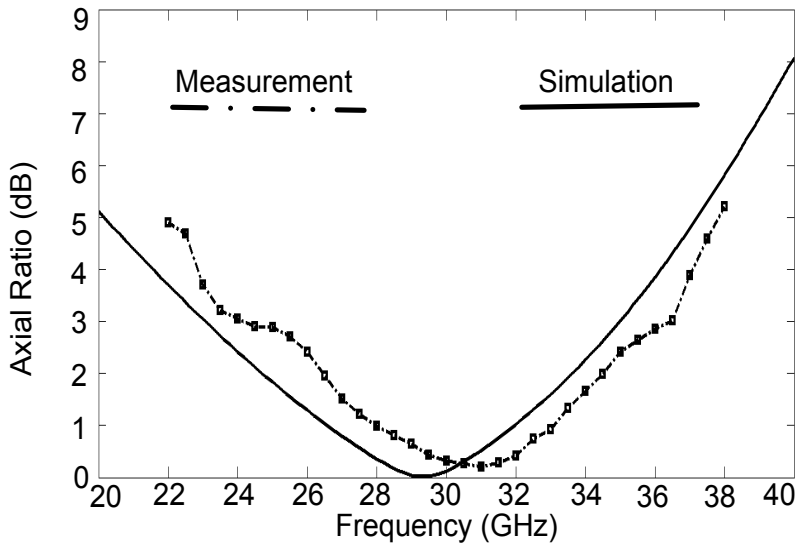

Figure 5-12: The measured and simulated axial ratio of the polarizer with the wideband horn antenna

In order to realize the polarizer performance in practical applications, it is implemented and axial ratio is measured using a wideband horn antenna, as shown in Figure 5-12. Fortunately, the measured axial ratio approximately has an acceptable agreement with the simulated one, covering 41% (AR ≤ 3dB).

5.1.4 Integrated Antenna Design

In order to investigate and verify the polarizer performance with an antenna, an 8-element linear array antenna is designed. The wide bandwidth and broadside pattern are two main reasons for choosing an aperture-coupled microstrip antenna (ACMA) as the primary prototype. Figure 5-13 shows the geometry of a single ACMA feeding operating on Ka-band around 30GHz.

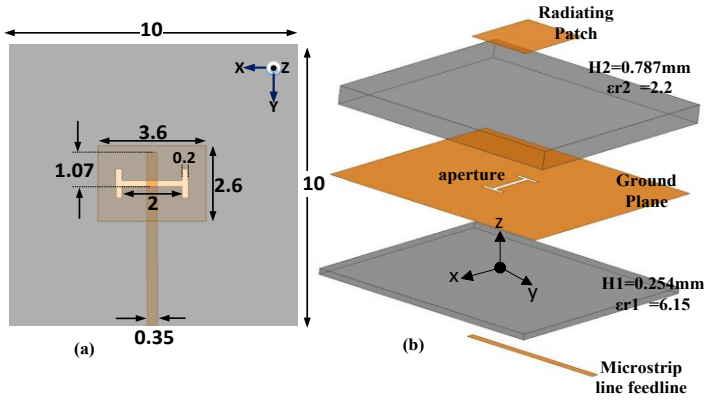

Figure 5-13: The Geometry of the single linear ACMA (a) top view and (b) side view (optimized values are versus millimetre).

The antenna consists of two different substrates, a Rogers RT/Duroid 5880 with dielectric constant 2.2 and thickness 0.787mm on the top and the other is Rogers 3006 with dielectric constant 6.15 and thickness 0.254mm on the bottom. Due to the limitation in the inter-element spacing of linear array structures, an H-shaped slot is etched off the common ground plate [121]. Figure 5-14 illustrates an equivalent circuit of ACMA similar to the model in [51]. Figure 5-15, shows the reflection coefficient and gain of the single ACMA.

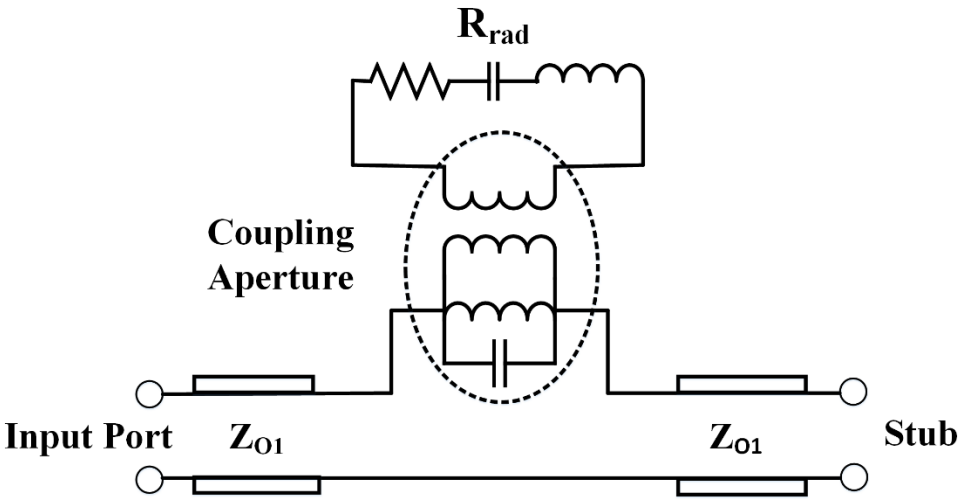

Figure 5-14: The equivalent circuit model of the ACMA [51].

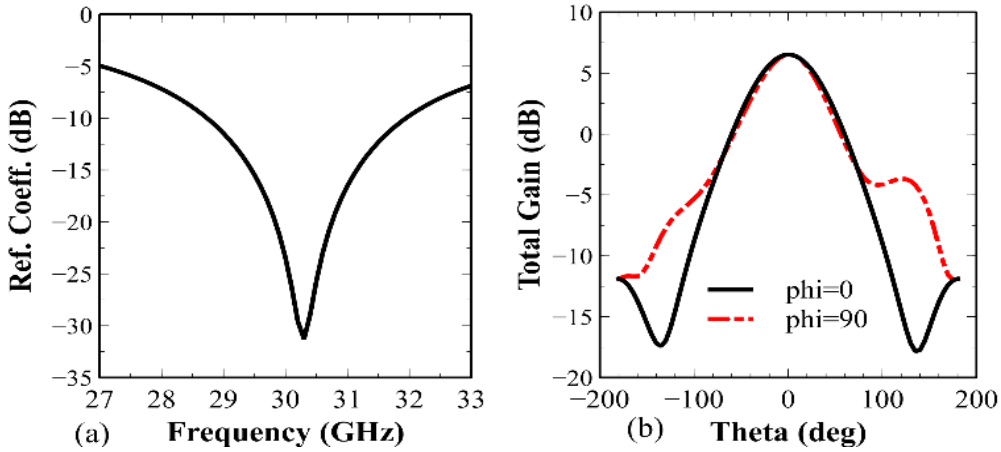

Figure 5-15: (a) The reflection coefficient and (b) radiation pattern of single ACMA at 30GHz .

In order to illuminate the transmission-type polarizer, the high gain array antenna with the capability of lower side lobe level (SLL) is proposed. Thus, an 8-element series-fed linearly polarized array antenna using suitable Chebyshev taper distribution operating at 30GHz is designed. Each antenna element is fed with a 50-ohm input impedance. To design the microstrip series-fed array, firstly the feeding network is

divided into two linear subarrays and fed at the center by microstrip line [122]. In order to guarantee the same phase among the elements and to obtain the radiation pattern at broadside, the distance between the feed points of the array elements has to be equaled to one guided wavelength (λg). The symmetric arrangement reduces the cross-polarization level of the array and minimizes the beam-squinting with frequency [122]-[123]. For this case, the cross-polar component produced in one direction of the antenna array is abandoned by the cross-polar component created in the reverse orientation of the antenna array at broadside. Moreover, a tapered distribution is achieved utilizing quarter-wavelength transformers ($\lambda_g/4$) along the line. The simulated reflection coefficient along with radiation pattern on the E-plane and H-plane at 30GHz are shown in Figure 5-17. It is observed that the ACMA array resonates at a centre frequency close to 30GHz with -23dB H-plane SLL and a gain of 13 dB.

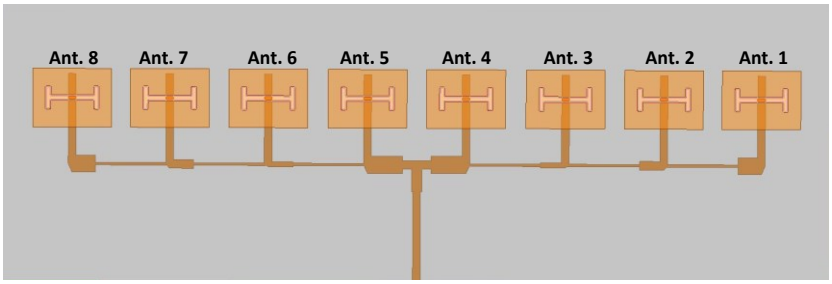

Figure 5-16: The 8-element linearly polarized array ACMA with Chebyshev tapered distribution

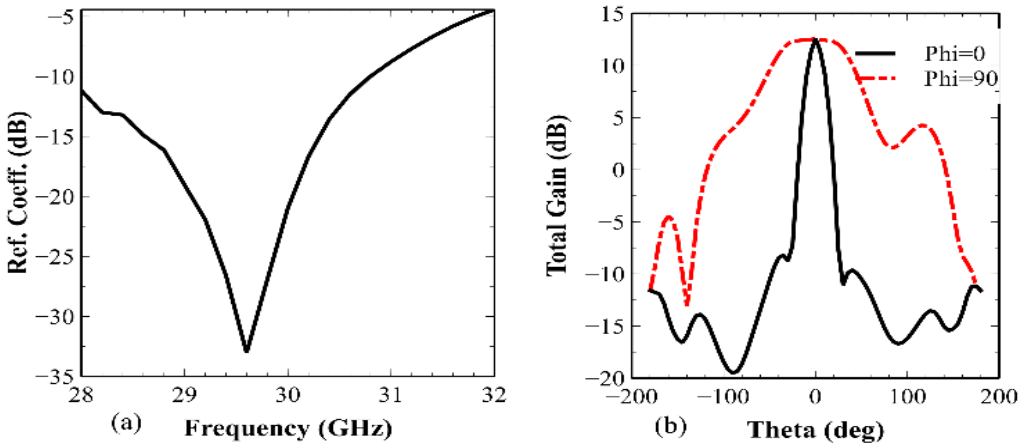

Figure 5-17: (a) The reflection coefficient and (b) radiation pattern of 8-element linear array antennas at 30GHz

In this section, both the 8-element ACMA LP array and polarizer structures are combined to form the final proposed structure. The LP array is placed under the polarizer using two spacers (holders) with a thickness 5mm (a half wavelength at 30 GHz), as shown in Figure 5-18. In order to connect the spacers to the antenna array structure, four screws are used. In addition, an end launch connector from Southwest Company to feed and excite the array is applied.

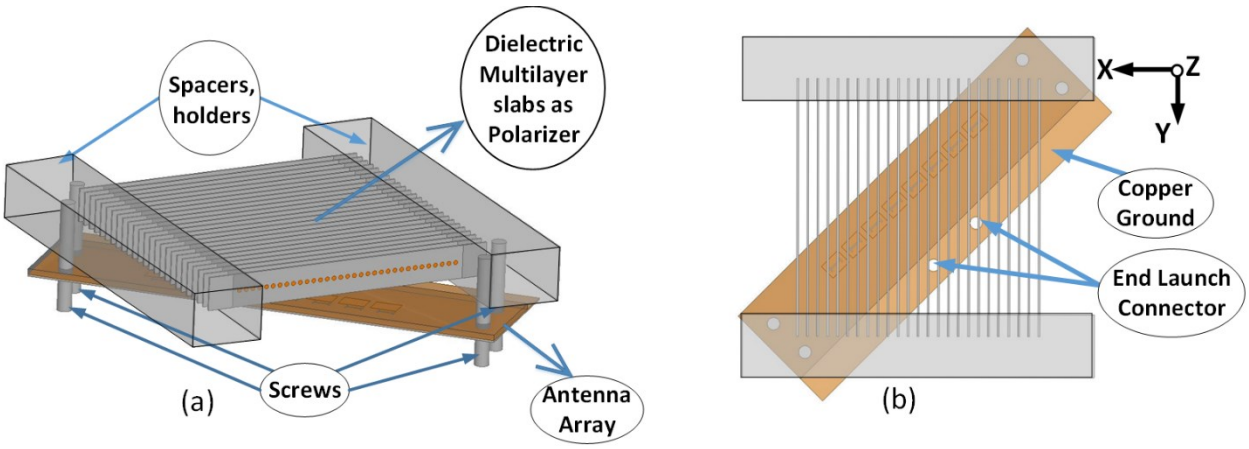

Figure 5-18: The final proposed design, including the multilayer slab polarizer, the antenna array, spacer, screws; (a) isometry view and (b) top view

To verify the design and integrated structure's performance, the proposed dielectric multilayer slab polarizer and the 8-element LP-ACMA were fabricated and tested. Figure 5-19 shows the photo of the assembled prototype.

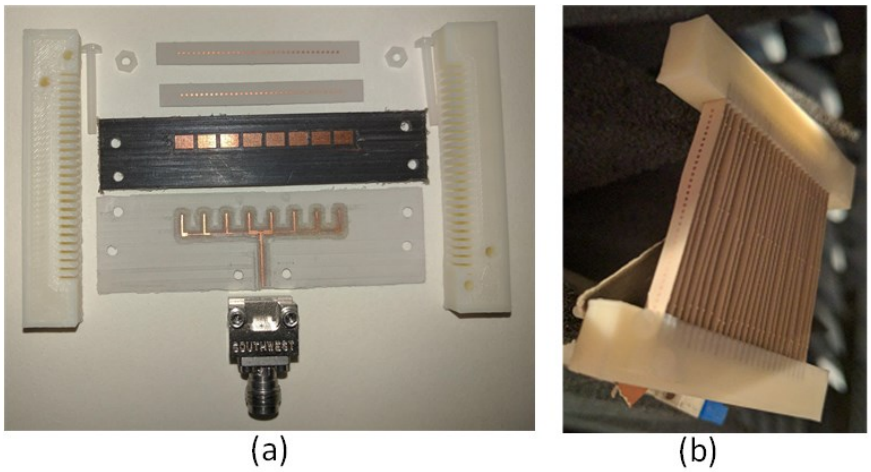

Figure 5-19: The photo of (a) the assembled design and (b) the proposed structure

It consists of two different substrates as the antenna array, dielectric multilayer slabs as the polarizer, spacers, screws, and connector. The measured reflection coefficient of the 8-element linear array ACMA with and without the polarizer were carried out utilizing an Agilent N5227A PNA Network Analyzer (10MHz-67GHz). Also, the far field anechoic chamber is utilized to measure the radiation patterns and axial ratio as depicted in Figure 5- 20.

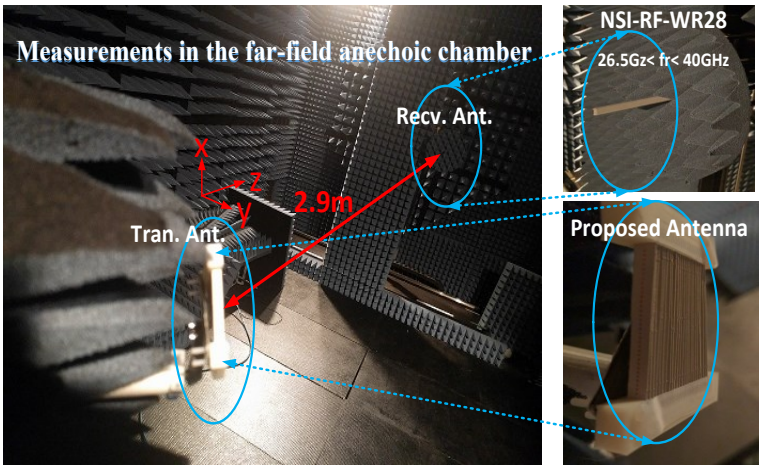

Figure 5-20: The photo of the antenna under test in the far-field anechoic chamber

The left and right-hand electric fields, and AR of the antenna are calculated from the measured electric fields, with both amplitude and phase following [55], [124]:

$$E_\theta = |E_\theta| \quad (5\text{-}20)$$

$$\vec{E}_{RH} = \frac{1}{\sqrt{2}}(\vec{E}_\theta + j\vec{E}_\varphi), \vec{E}_{LH} = \frac{1}{\sqrt{2}}(\vec{E}_\theta - j\vec{E}_\varphi), \quad (5\text{-}21)$$

$$AR(dB) = 10\log\left(\frac{\left|\left|\vec{E}_{RH}\right| + \left|\vec{E}_{LH}\right|\right|}{\left|\left|\vec{E}_{RH}\right| - \left|\vec{E}_{LH}\right|\right|}\right) \quad (5\text{-}22)$$

The measured and simulated results including the reflection coefficient, axial ratio, and total gain are exhibited in Figure 5-21. It can be observed from Figure 5- 21 that the experimental results and simulated ones have an acceptable agreement. The measured results of the polarizer along with the antenna array show that impedance bandwidth (|s11|≤-10dB) covers 28GHz to 32GHz with an axial ratio bandwidth (AR≤3dB) from 28GHz to 31.5GHz, and a total gain of 13dBi with a pure CP at the central frequency of 30GHz. As shown in Figure 5-22, the radiation patterns of the proposed antenna array with and without the polarizer at 30GHz are presented.

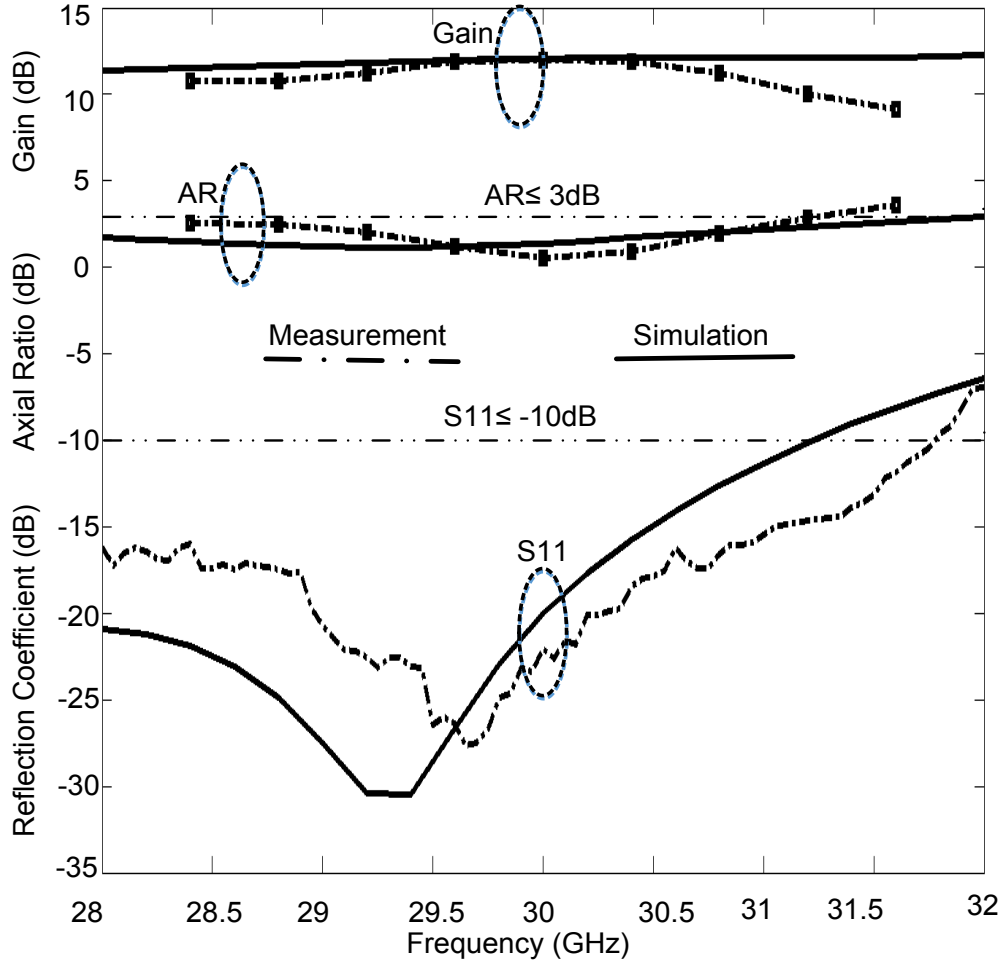

Figure 5-21: The measured and simulated curves of total gain, axial ratio, and reflection coefficient of the proposed design; including the LP antenna array with the polarizer.

From the normalized total gain curve in Figure 5- 22(a), it can be observed that the sidelobe level (SLL) is nearly -20dB due to the Chebyshev tapered distribution used in the feed line. Figure 5-22 (b) shows the normalized RHCP gain of the final proposed integrated structure including both the antenna array and polarizer. The simulated and measured results have an acceptable agreement in the main beam angular

region. In Figure 5-23, it can be realized that the radiated field from the antenna rotates in clockwise direction demonstrating a right-hand circularly polarized wave.

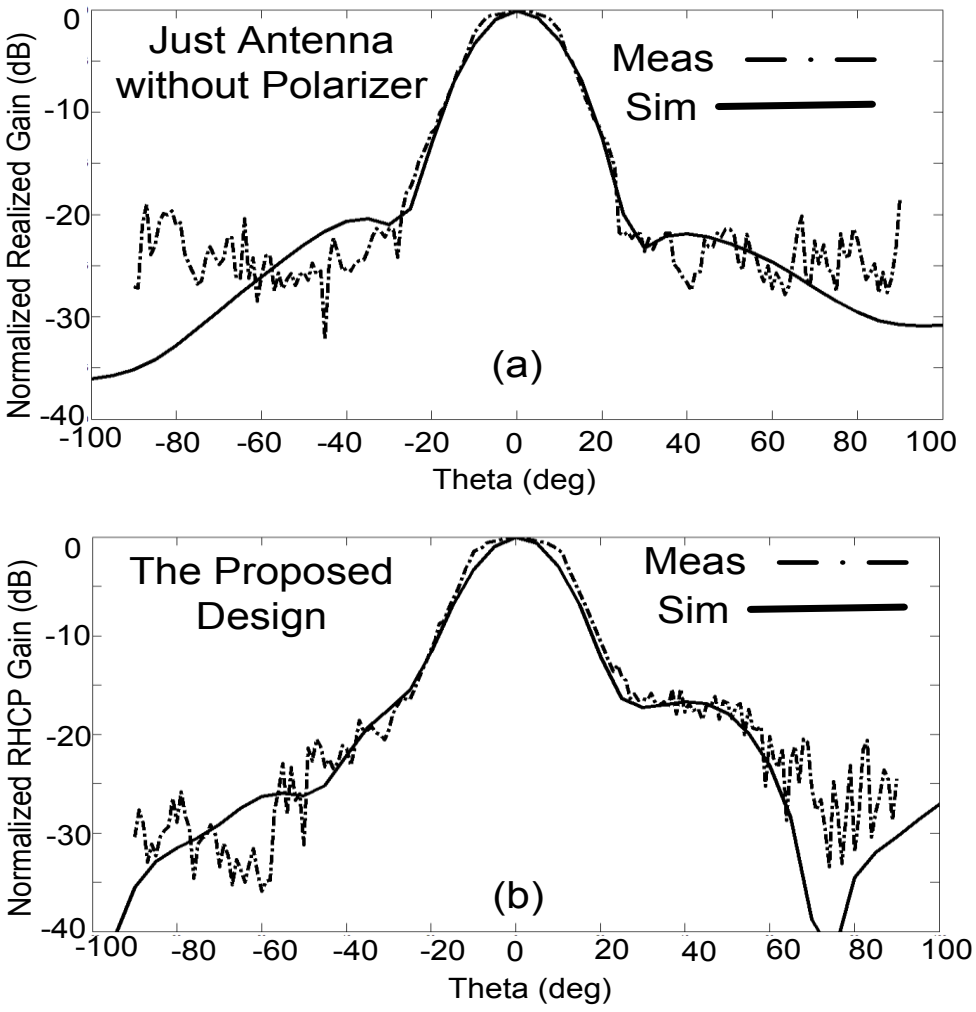

Figure 5-22: (a) The normalized total gain of the LP antenna array without the polarizer and (b) the normalized RHCP gain of the polarizer with the antenna array at 30GHz

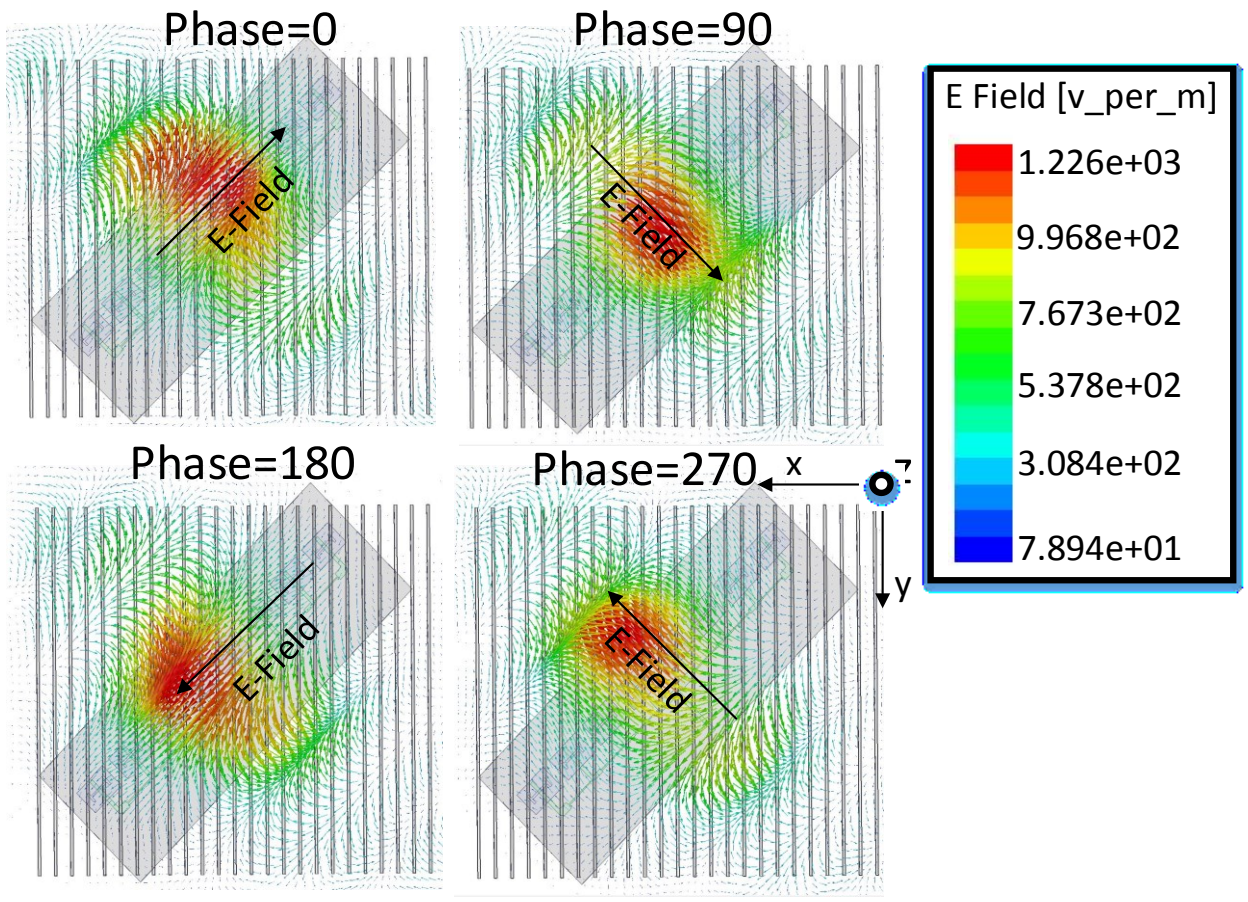

Figure 5-23: (a) RHCP far E-field variations at different phases (a)0°, (b)90°, (c)180°, and (d)270 °at the centre frequency 30 GHz.

Conclusion

In this thesis, a new polarizer based on dielectric multilayer slabs for MMW applications is presented. The polarizer can function from 23 GHz to 35 GHz (42%) with excellent impedance and AR bandwidths. The insertion loss of polarizer is less than 0.5 dB which in industrial applications can be excellent. The polarizer is fabricated and measured by a wideband horn antenna satisfying the simulated results. Next, in order to design a high-gain circularly polarized structure at around 30 GHz, an 8-element LP array antenna with Chebyshev tapered distribution is designed and integrated with the polarizer. Obviously, the antenna restricts the overall bandwidth due to the narrowband nature of the LP antenna array. The combined structure was fabricated and measured. There is an excellent agreement between the experimental results with the simulated ones. The measured results of the fabricated structure show that the final design is able to cover impedance and axial-ratio bandwidths nearly 28 GHz to 31.5 GHz. Furthermore, it has a pure CP and realized a gain of 13 dBi at 30 GHz. This polarizer with the antenna array can be a suitable candidate for

several applications including satellite communications, orthogonal polarization transformers, sub-reflectors, and CP lenses.

Chapter 6. Broadband RCS Reduction using FSS Metasurface

Introduction

Recently, FSSs have received extensive attention in MMW wireless communication and imaging systems so that designers have allocated extensive efforts to investigation community because of their potential applications in the commercial and industrial sectors [126]. To control, manipulate, and reduce the characteristics of the scattered EM fields, wideband RCS suppression has always been a challenging goal and interesting issue to designers [134]. Different methods have been proposed in the literature to steer the scattered waves away from the backscatter direction which has based on loading the object with radar absorbing materials (RAM) and/or passive or active cancellation [136]. However, this technique rises the weight and air drag. Furthermore, the metallic ground plane with RAM is angle and frequency sensitivity because it has a narrow frequency band [134-137]. Another approach is to shape the target geometry [138] that it can be considered as an effective alternative, but this technique increases the design complexity in terms of the engineering aspects of the vehicle so that it only functions well at high frequencies while adversely affects is observed at low frequencies [134-137]. Another alternative of attaining the scattering purpose, using a planar structure has been given by [139], in which it is based on a combination of perfect electric conductors (PEC) and artificial magnetic conductors (AMC) in a chess board. The low profile and simple structure are the main benefits of this structure. In this configuration, AMC unit cells produce a 0° phase difference to the scattered waves while PEC reflects incident waves with a 180° phase difference at its operating frequency. Applying the contribution of the PEC and AMC cells, a 180 phase difference is obtained, resulting in destructive interference and creating a null in the specular angle [135-139]. The main disadvantage the mentioned configuration, in [139], is the narrowband behaviour of the AMC cells so that the chess board earns a 10-dB RCS reduction (normalized to a PEC surface) over a bandwidth of nearly 5% in [138], which is not enough for most applications. It is obvious that bandwidth extension of these kinds of designs is still one of the critical study interests. In this chapter of the thesis, in order to reduce RCS, two different designs will be proposed.

Initially, a super-wideband reflective metasurface for both monostatic and bistatic RCS suppression with different incident angles is presented. The major property of the proposed metasurface is to rotate 90° linear polarization. The design consists of a two-layer substrate with the identical material and thickness. The main metasurface is arranged by the binary elements “0” and “1”. Each of the Elements is composed of 4×4 FSS cells. The elements are formed by the binary coding matrix to distribute the scattered electromagnetic waves and reduce the maximum bistatic RCS of the metasurface over a wide band of incident angles at both polarizations. In order to achieve the binary coding matrix, group search optimization (GSO)

algorithm is employed. The element arrangement on metasurface leads to a significant RCS reduction in frequency range from 5.1 GHz to 22.1 GHz (approximately 125%) at normal incidence for both polarizations. Meanwhile, a theoretical analysis is performed on the ratio of the "0" and "1" elements using Least Square Error (LSE) method to find the best ratio value so that the optimum value of the ratio as a new constraint is added to GSO algorithm to attain a new coding matrix in another process of the optimization algorithm.

As the second design of this chapter, a wideband CP antenna with low RCS and the high gain feature is presented. The proposed antenna is based on a combination of the FPC and sequential feeding technique. The purpose of this antenna is to produce CP with the high directive level on wide bandwidth keeping low RCS.

Broadband Coding FSS Metasurface for RCS

In this section of this chapter, a wideband metasurface for RCS reduction based on a polarization conversion is presented. The unit cell composes of a two-layer metasurface based on FSS backed by a thin grounded dielectric substrate. In addition, a polarization conversion ratio (PCR) of nearly 131% for an efficiency of higher than 90% is achieved. To distribute the scattered electromagnetic waves and suppress the maximum bistatic RCS of the metasurface over a broad band of incident angles at both polarizations, the elements are arranged using the binary coding matrix achieved by group search optimization (GSO) algorithm. The reflective two-layer metasurface is designed in such a way to generate reflection phase difference of 180° between two elements "0" and "1" on a broad frequency band. A theoretical analysis is performed on the ratio of the "0" and "1" elements using Least Square Error (LSE) method to find the best ratio value. The simulated and experimental results show that the structure can significantly reduce 10-dB RCS over a wide frequency range from 5.1 GHz to 22.1 GHz (125%) at the normal incidence for both polarizations.

6.1.1 Unit Cell Structure

The proposed FSS cell consists of a two-layer dielectric substrate, identical materials, and thicknesses, with a full PEC ground plane on the bottom and a double-head arrow FSS on the middle, while there is no copper on the top of the second layer, As shown in Figure 6-1. The double-head arrow and the backing sheet are separated by a Rogers's 5880 dielectric spacer with a thickness 3.175mm, a dielectric constant ε_r=2.2, and a loss tangent tan δ=0.009.

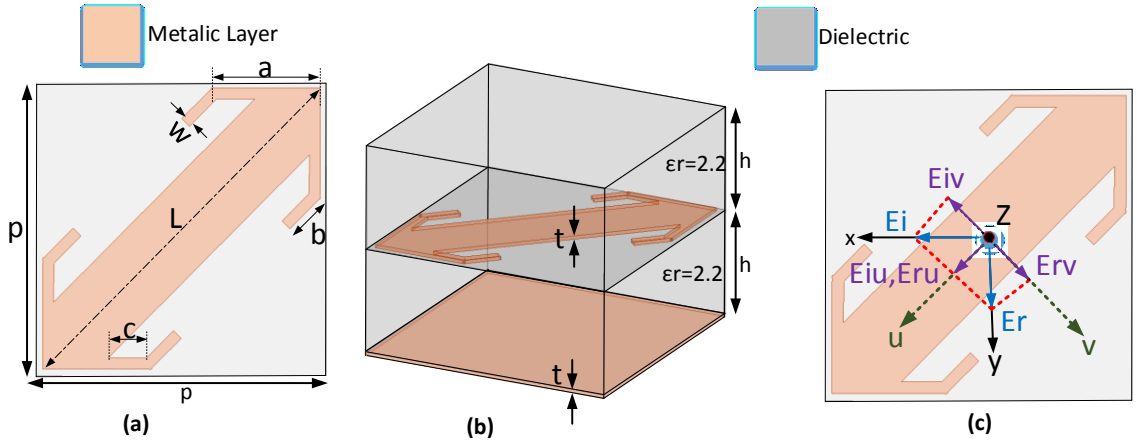

Figure 6-1: The FSS unit cell: (a) front view, (b) side view of the unit cell, (c) x- and y–axes are used to highlight EM wave direction, while u- and v-axes are used to show the FSS anisotropic axes.

The periodicity of the FSS unit cell is 8mm. The other parameters of the double-head arrow structure are summarized in Table 6-1.

Table 6-1: The proposed FSS unit cell dimensions

Parameter	Size (mm)	Parameter	Size (mm)
p	8	b	1.13
L	10.75	c	1.05
W	0.3	h	3.175
a	3	t	1.13

The proposed FSS has a symmetric axis defined by u-axis along 45° direction with respect to y-direction as shown in Figure 6-1(c). Thus, the FSS can be considered as an anisotropic homogeneous layer with a dispersive relative permeability tensor $\vec{\mu}$ and a relative permittivity put on top of a copper groundsheet, which is shown by u, v, and z axes. Therefore, $\vec{\mu}$ can be indicated by diagonal elements μ_{uu}, μ_{vv}, and μ_{zz}. As it can be observed in Figure 6-1(c), the proposed FSS is combined by oblique v-shaped resonators and wire resonator. Hence, it is apparent that the proposed FSS resonator has multiple resonances [145]. In order to prove this declaration, the FSS resonance behaviour is determined using the model unit cell with the Floquet port by ANSYS HFSS. Figure 6-2 exhibits curves of the co-polarization reflection versus frequency.

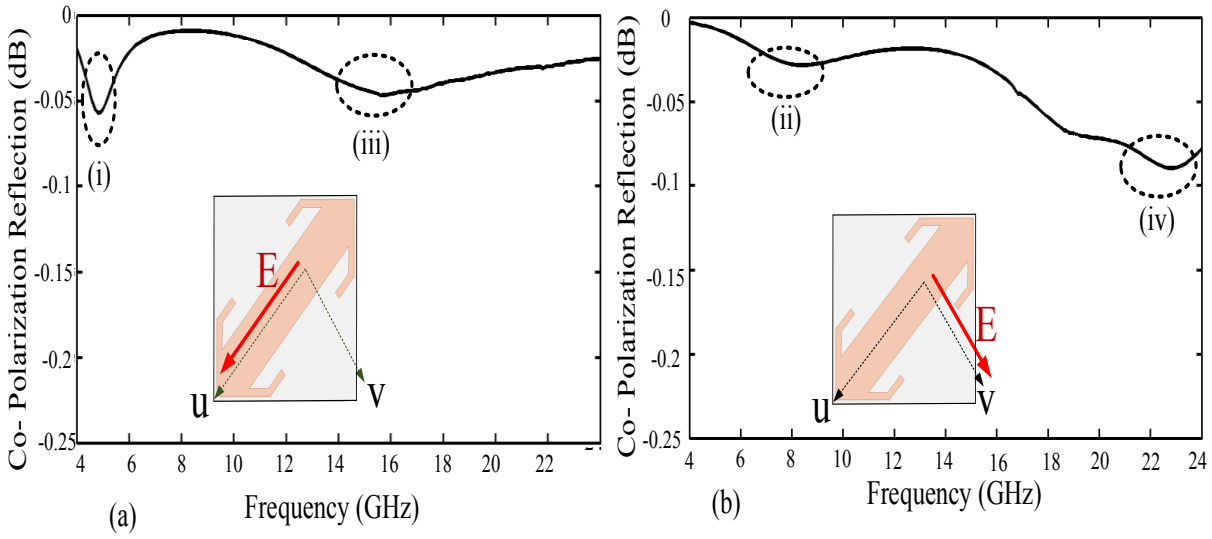

Figure 6-2: The four resonances of the proposed FSS under normal incidence: (a) u-polarized case and (b) v-polarized case.

It is obvious that two resonances (i) and (iii) are excited in the u-polarized case as depicted in Figure 6-2(a), whilst the two other resonances (ii) and (iv) are excited in the v-polarized case as illustrated in Figure 6-2(b). Once x-polarized waves are incident as depicted in Figure 6-1 (c), four resonances are excited since the u- and v- components exist at the same time. To determine if a resonance is magnetic or electric, it should be examined the resonance type through surface current distribution, as shown in Figure 6-3. It is observed that the resonance parts of the FSS how to behave in both polarized cases. Electric and magnetic resonances are produced by the symmetric and anti-symmetric couplings of the currents on the FSS resonator and PEC groundsheet, as shown in Figures. 6-3(a) and 6-3(b), respectively.

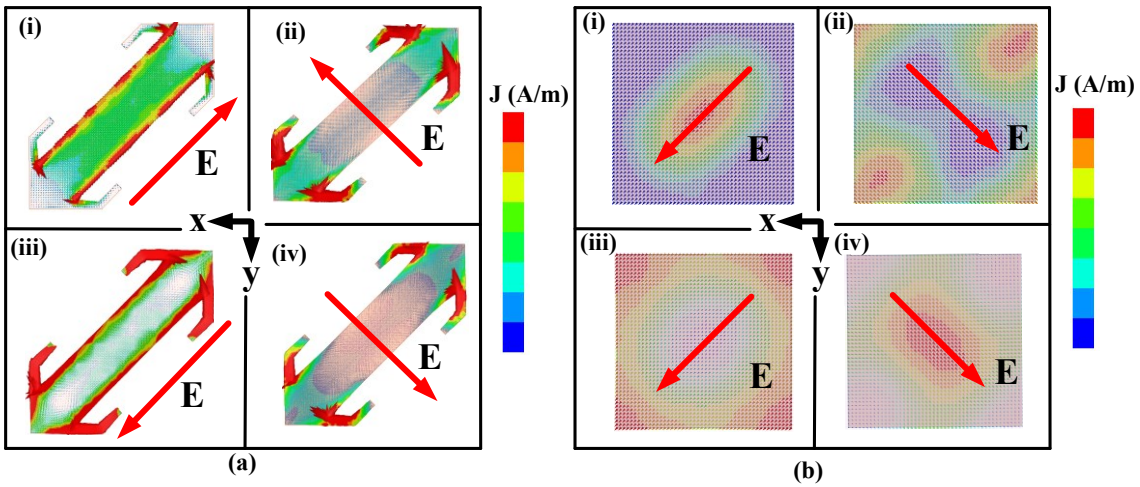

Figure 6-3: The surface current distributions induced on (a) FSS and (b) ground plate for resonance (i) to resonance (iv).

As a matter of fact, the electric and magnetic resonances are determined qualitatively with respect to the electrical length between two metallic layers [146]. The operating wavelength of the resonances (iii) and (iv) are much smaller than operating wavelength of resonances (i) and (ii). So, the electrical length between the two metallic parts for resonates (iii) and (iv) is much greater than it for resonances (i) and (ii) under the same unit cell thickness (h). Hence, it can be concluded that magnetic coupling for resonances (iii) and (iv) is much less than resonances (i) and (ii) [146]. After realizing the physics of multiple resonances, the concept of the polarization conversion in the FSS becomes apparent. Preferably, the polarization must be entirely converted orthogonally after reflection. In order to examine the polarization conversion mechanism of the FSS cell, a schematic diagram can be applied. Figure 6-4 exhibits the elements of "0" and "1" along with incident and reflection electric fields. As it can be seen the elements are able to generate "symmetric" and "antisymmetric" modes via electric-field components along the v- and u-axes, respectively. According to a normally illuminating plane wave "Ei" linearly polarized in the x-direction, "Ei" can be decomposed into the parallel components and the perpendicular term "Eiv" and "Eiu", respectively.

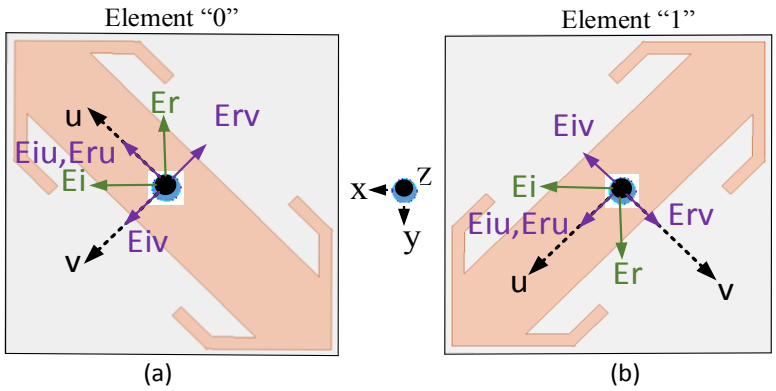

Figure 6-4: Intuitive image of the x-polarized wave (E incident field along the x-axis) normally illuminating the FSS cell of (a) the elements "0" and (b) "1".

As shown in Figure 6-4 (a), the function in the "v" direction can be taken into account as a PEC because of the electric resonance, therefore "Erv" and "Eiv" after being reflected will be out-of-phase. Although, the function in the "u" direction can be considered as a high-impedance surface in the "u" direction due to magnetic resonance. Hence, "Eru" and "Eiv" are in–phase. Using vector synthesizing, y-polarized reflective wave "Er" is achieved by conversion of the illuminating x-polarized wave "Ei". Element "1" in Figure 6-4 (b) behaves in opposite side. Regarding the examination aforementioned, reflective wave "Er" generated by both structures, elements "0" and "1", produces 180°-phase difference. For verifying polarization conversion, numerical simulations are carried out using both softwares Ansys HFSS and CST Microwave Studio. The periodic boundary conditions by master and slave in x- and y-directions and a

Floquet port along the z-direction are applied. As aforementioned above, the proposed polarization conversion metasurface is composed of FSS unit cells, which can be utilized for controlling the reflective parameters of scattering EM waves. The reflected EM wave is mainly composed of cross- and co-polarized reflection components R_{xy} and R_{yy} respectively, which can be computed as below [147].

$$R_{xy}=\frac{|E_{rx}|}{|E_{iy}|}=\sqrt{\frac{(1-cos\Delta\varphi)}{2}} \tag{6-1}$$

$$R_{yy}=\frac{|E_{ry}|}{|E_{iy}|}=\sqrt{\frac{(1+cos\Delta\varphi)}{2}} \tag{6-2}$$

where $\Delta\varphi$ is defined as the phase difference between R_{uu} and R_{vv}. Meanwhile, the polarization conversion ratio (PCR) is considered as [147]

$$PCR=\frac{R_{xy}^2}{R_{xy}^2+R_{yy}^2} \tag{6-3}$$

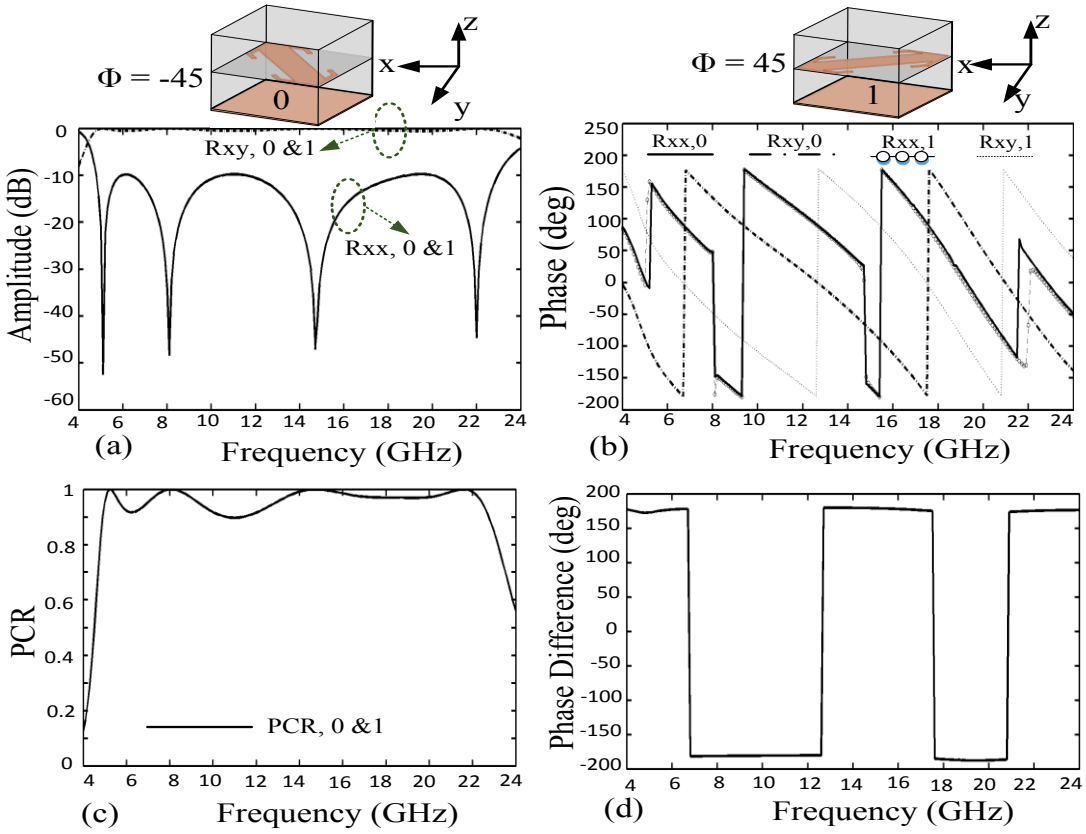

Figure 6-5: The geometry of the FSS elements "0" and "1", respectively the rotators with angles of -45° and 45°. (a) Amplitude of reflective coefficients for elements "0" and "1" with co-polarization (xx) and cross-polarization (xy), (b) Phase of reflective coefficients versus frequency, (c) Polarization conversion ratio (PCR) of the elements "0" and "1", and (d) Phase difference between the element "0" and element "1".

As shown in Figure 6-5, the FSS unit cells with a property of reflective polarization conversion have been introduced as elements "0" and "1". The elements "0" and "1" desirably direct the scattering amplitude and phase of incidence in a broadband band, as depicted in Figure 6-5 (b) and (d). It is observed that in the frequency range from 4.8 GHz to 23 GHz, the co-polarized reflection R_{xx} is less than -10dB. Hence, it is predicted that the PCR will be higher than 90 % with a relative bandwidth closely 131%. Now, by (6-3), the PCR of elements "0" and "1" is computed. As shown in Figure 6-5(c), it is observed that the PCR for an efficiency of higher than 90% is wider than 130%. Table 6-2 gives a comparison between the proposed structure and other reported polarization converters [150-156]. It is depicted that the proposed FSS has a super-broadband as compared with it in other studies in which the PCR is higher than 130%.

Table 6-2: Comparison with other wideband polarization convertors

Year/ References	**O. BW. (GHz)/ R. BW. (%)**	**Electrical size (width × length × thickness)**
2010/ [150]	14.7-18 (20%)	$0.9\lambda_g \times 0.3\lambda_g \times 0.4\lambda_g$
2010/ [151]	10.6-17.5 (49%)	$0.6\lambda_g \times 0.6\lambda_g \times 0.2\lambda_g$
2015/ [152]	12.4-28 (77%)	$0.7\lambda_g \times 0.7\lambda_g \times 0.2\lambda_g$
2016/ [153]	5.7-10.3 (58%)	$0.4\lambda_g \times 0.4\lambda_g \times 0.1\lambda_g$
2016/ [154]	7390-13870 (61%)	$0.7\lambda_g \times 0.7\lambda_g \times 0.2\lambda_g$
2016/ [155]	10-18.4 (59%)	$0.6\lambda_g \times 0.6\lambda_g \times 0.2\lambda_g$
2017/ [156]	6-17.8 (98%)	$0.3\lambda_g \times 0.3\lambda_g \times 0.3\lambda_g$
Proposed	4.8-22.8 (131%)	$0.4\lambda_g \times 0.4\lambda_g \times 0.3\lambda_g$

O. BW. : Operation bandwidth (PCR ≥ 90 %)

R. BW. : Relative bandwidth (PCR ≥ 90 %)

Figure 6-6 depicts the simulated results of reflective parameters for the polarization conversion when it is impinged by EM wave with different oblique angles of incidence versus frequency. The amplitudes of reflective coefficients with co-polarization with varying oblique angles of incidence from normal to 40° versus frequency approximately have a clear transformation from 0 to 1, as shown in Figure 6-6(a). In addition, it is seen that magnetic to electric resonances (i) to (iv) are nearly preserved for different oblique of incidences at 5 GHz, 8 GHz, 14.5 GHz, 22 GHz, respectively. As predicted before, the amplitudes of reflective coefficients with cross-polarization with varying oblique angles of incidence approximately have an opposite manner with it in co-polarization, as shown in Figure 6-6(b). It means that reflective coefficients with cross-polarization nearly for all oblique angles of incidence completely reflect on the

desired frequency band. Correspondingly, the PCR results of the reflective FSS are presented for various oblique angles of incidence versus frequency band in Figure 6-6(c). From the PCR results, it can be found out that with changing oblique angles of incidence only at two frequencies (approximately 16.5 GHz and 18.5 GHz) the PCR is deteriorated, while it nearly behaves persistently at the lower frequency band (5 GHz to 16 GHz) for oblique incidence.

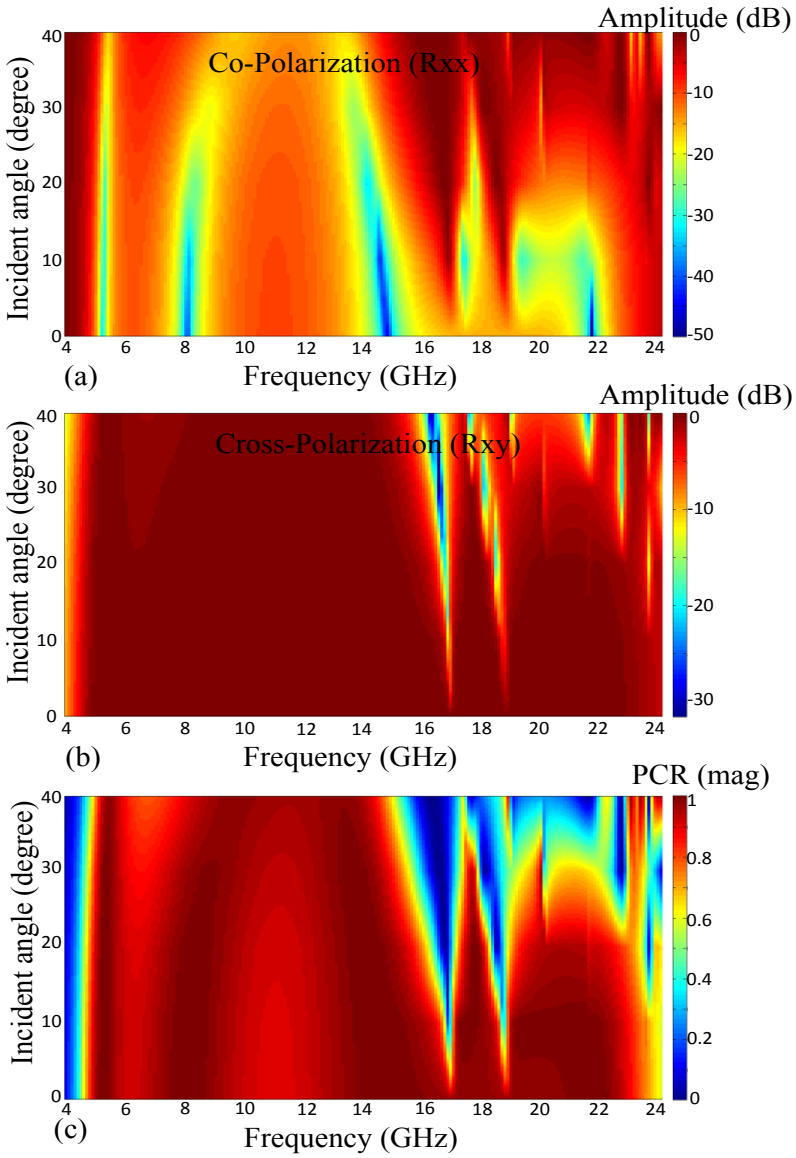

Figure 6-6: Simulated results of reflective parameters of FSS with different incident angles versus frequency band. (a) The amplitude of reflective coefficients with co-polarization, (b) amplitude of reflective coefficients with cross-polarization, (c) PCR of reflective coefficients.

In order to understand the design procedure of FSS unit cell Figure 6-7 is shown. From Figure 6-7, it is evident that the PCR of one-layer FSS in case I, has not satisfied efficiency 90%. Therefore, in order to modify the PCR, the second layer with the identical substrate (without any copper) is added as the FSS in

case II. In comparison with the case I, PCR in case II little improved. In case III as the proposed design, with adjustment in design parameters of the double-head arrow of the FSS, PCR is expanded from 4.8 GHz to 22.8 GHz (approximately 130%) for efficiency higher than 90%.

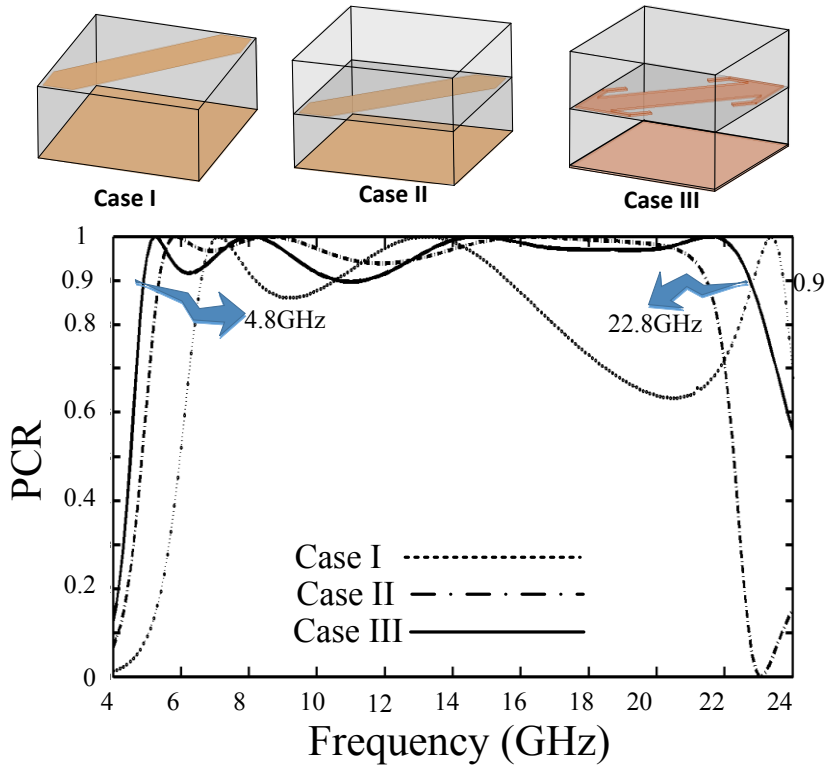

Figure 6-7: The PCR results for the different FSS cells with respect to the design procedure

6.1.2 Metasurface Mechanism

The mechanism of metasurface including the FSS is determined in this section. The fundamental of FSS metasurface is that the reflective fields will abandon and shape scattering characteristics within a frequency band of interest once the phase difference of the scattered fields between the two designs is 180°. RCS suppression and bistatic maximum scattering angle are evaluated through array theory [134]. To reach this goal, a metasurface containing $N \times N$ identical-sized FSS cells with dimension "D" is designed. Each FSS cell is occupied using elements "0" and "1", as depicted in Figure 6-4. The reflective phase of each FSS element is supposed to be $\varphi(m,n)$ which is either 0° or 180° for the frequency band of interest. The far-field function reflected by the FSS metasurface is given as:

$$f(\theta,\varphi)=f_e(\theta,\varphi)\sum_{m=1}^{N}\sum_{n=1}^{N}exp\left\{-i\left\{\varphi(m,n)+kDsin\theta\left[\left(m-\frac{1}{2}\right)cos\varphi+\left(n-\frac{1}{2}\right)sin\varphi\right]\right\}\right\} \tag{6-4}$$

where k is the wave vector. φ and θ are the azimuth and elevation angles of an arbitrary direction, respectively, while $f_e(\theta,\varphi)$ is considered as the pattern function of a unit cell. Meanwhile, the coupling between unit cells "0" and "1" is ignored due to the quick computations and configurable orthogonality. Directivity equation of the reflective metasurface can be expressed as

$$Dir(\theta,\varphi)=\frac{4\pi\left|f(\theta,\varphi)\right|^2}{\int_0^{2\pi}\int_0^{\pi/2}\left|f(\theta,\varphi)\right|^2 sin\theta d\theta d\varphi} \tag{6-5}$$

The $f_e(\theta,\varphi)$ term is eliminated due to the phase difference between unit cells "0" and "1". Hence, the functions (6-4) and (6-5) above let us control the scattering waves using the metasurface coding of FSS cells. The RCS reduction of a reflective chess board, compared to that of a PEC, can be expressed by [134]

$$\text{RCS reduction}=10log\left[\frac{\lim_{r\to\infty}\left[4\pi r^2\frac{\left|E^s\right|^2}{\left|E^i\right|^2}\right]}{\lim_{r\to\infty}\left[4\pi r^2(1)^2\right]}\right]=10log\left[\frac{\left|E^s\right|^2}{\left|E^i\right|^2}\right] \tag{6-6}$$

In is study, some preliminary assumptions are made to limit the search space and in turn, steer the optimization process toward the optimal solution. To perform, so, the following patterns should be avoided:

(i) A chessboard with all FSS cells equal to either zero or one;

(ii) The coding sequences of 010101/010101…; and,

(iii) The coding sequence of 010101/101010…

The best RCS reduction is obtained using optimizing the coding sequences of elements of "0" and "1" based on FSS cells.

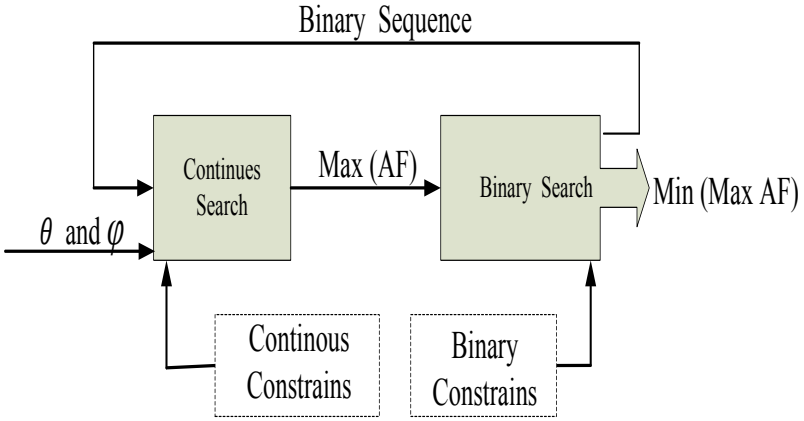

Figure 6-8: The Defined bi-level model of the algorithm.

6.1.3 Least Square Error (LSE) Method

In this investigation, group search optimization (GSO) algorithm is employed for finding an optimal arrangement of the FSS unit-cells. Here, a new constraint is considered which restricts the ratio of "1" and "0" elements to a predefined value. According to the set of analysis based on a trial-and-error process, it has been obtained that having a special ratio between elements leads to better solutions, as shown in Figure 6-9.

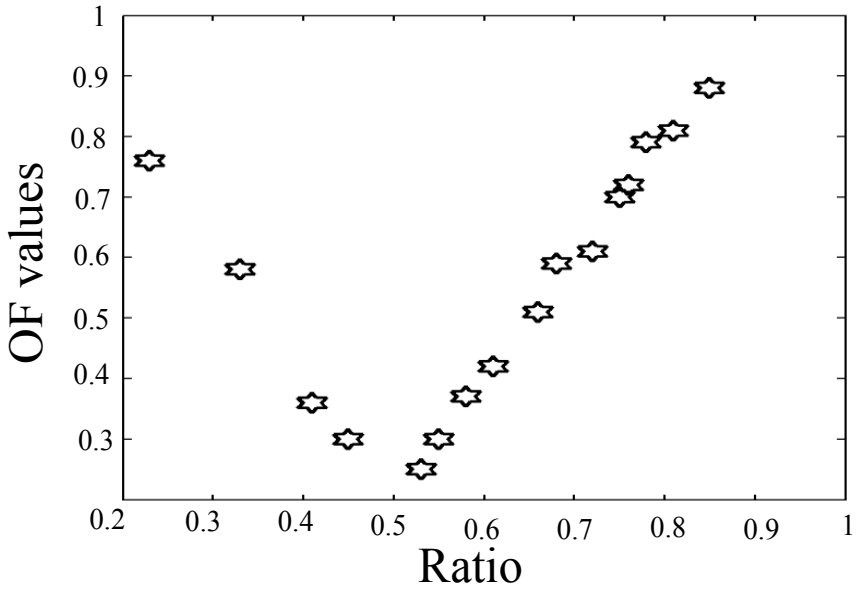

Figure 6-9: Optimized OF values versus ratio of "1" and "0" elements.

However, finding the accurate ratio is a formidable issue. In this study, we have proposed a new method to find the best value associated with ratio of "1" and "0" elements. As an example, the structure and matrix shown in Figure 6-10 are presented for the first objective function (OF) while its ratio is 0.4. Given the

value of the objective function, namely OF, for different ratios, say R_1, R_2,…, it is proposed to obligate a poly nominal relation such as (6-7) between each pair of OF and R which is depicted in matrix format by (6-8):

$$OF_i=\sum_{n=0}^{\infty} a_n R_i^n+\xi_i \qquad i=1,2,\ldots \tag{6-7}$$

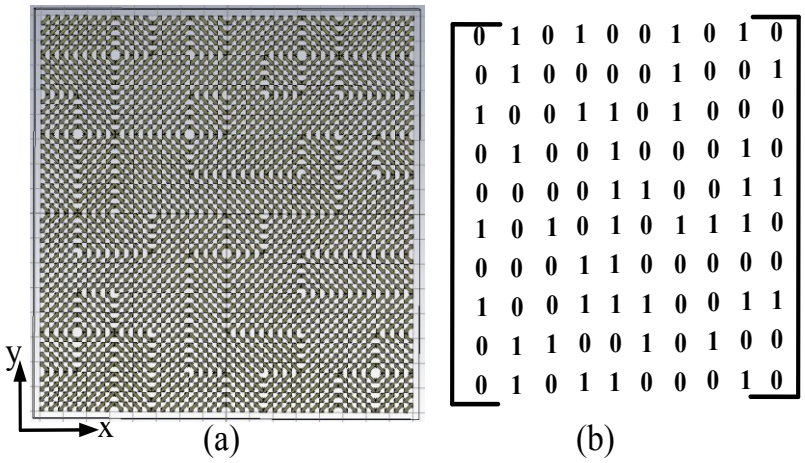

Figure 6-10: Proposed metasurface and associated coding matrix with ratio 0.4.

$$\underbrace{\begin{bmatrix} of_1 \\ of_2 \\ \vdots \\ of_i \end{bmatrix}}_{OF_{Ns\times 1}} = \underbrace{\begin{bmatrix} 1 & R_1 & R_1^2 & \cdots & R_1^n \\ 1 & R_2 & R_2^2 & & R_2^n \\ \vdots & & \vdots & \ddots & \vdots \\ 1 & R_i & R_i^n & \cdots & R_i^n \end{bmatrix}}_{H_{Ns\times Nu}} \underbrace{\begin{bmatrix} a_0 \\ a_1 \\ \vdots \\ a_n \end{bmatrix}}_{A_{Nu\times 1}} + \underbrace{\begin{bmatrix} \xi_1 \\ \xi_2 \\ \vdots \\ \xi_i \end{bmatrix}}_{\xi_{Ns\times 1}} \tag{6-8}$$

Where N_u is a number of unknown variables and N_s is a number of input samples. To minimize the estimation error, an appropriate error indicator based on the square value of individual errors is defined as follows:

$$J(X)=\xi^2=[OF\text{-}HA]^T\ (OF\text{-}HA) \tag{6-9}$$

The minimum of $J(X)$ is obtained when the gradient of $J(X)$, namely $\nabla J(X)$, is 0. Doing so "A" is computed as:

$$A=[H^T HJ^{-1} H^T OF \tag{6-10}$$

Having a sufficient number of samples, the unknown variables can be estimated. In order to satisfy maximum likelihood criteria, the number of OF samples should be larger than that of unknown variables. Considering N_u to be 2, we will come up with a polynomial equation such as (6-11):

$$OF=a_2R^2+a_1R+a_0 \tag{6-11}$$

Hence, optimal ratio is:

$$R^{opt}=\frac{-a_1}{2a_2} \tag{6-12}$$

Note that, the relationship between OF and R can be described by any other polynomial function. A high degree function would need extra input samples which add to the computational burden of the whole process; however, a low value might jeopardize the accuracy of the estimation. Thus, a compromised decision should be made on the degree of polynomial function. This was done based on a trial-and-error process in simulation studies. To summarize the entire process Figure 6-11 is given. The chart presented in Figure 6-11 indicates the procedure of choosing the binary coding matrix. Firstly, the GSO optimization for equal iterations gives different OF_i separately, which for each OF we will have a different ratio R_i. Then, in this study, we have used LSE method to achieve the extremum point or optimal ratio R^{opt}. After achieving R^{opt}, it is operated in GSO in the new process as a new assumption which the optimization must satisfy that requirement.

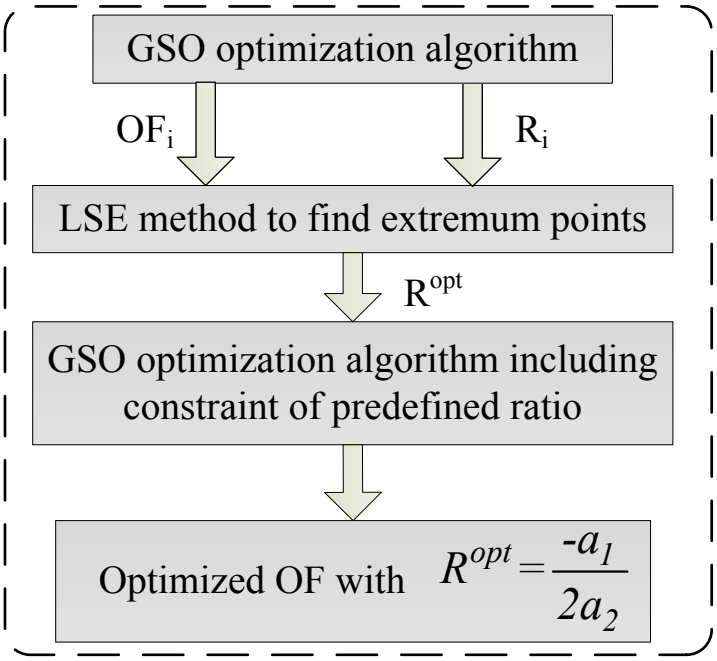

Figure 6-11: Flowchart of GSO optimazation and LSE method to find the best coding arrangemnt for the metasurface board

6.1.4 Reflective Metasurface Configuration

Now, an optimized binary coding matrix corresponding to the whole metasurface is attained, as shown in Figure 6-12. The proposed coding matrix and associated metasurface are observed with an optimum ratio 0.5, in which each element "0" and "1" is formed by 4×4 FSS unit cells with a size 32×32mm^2. In order to realize the importance of the ratio issue, Figure 6-13 is exhibited, where it is observed how the RCS reduction in the reflective metasurface can be changed by various ratios. As mentioned above, ratio 0.4 for the first OF using GSO optimization is earned while after employing LSE method the optimum ratio 0.5 is computed.

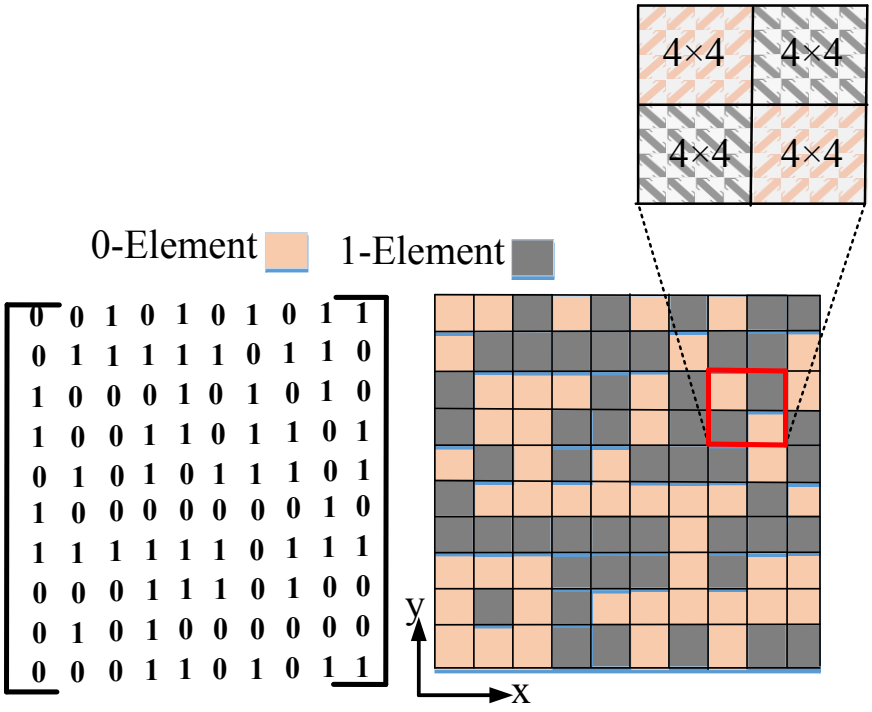

Figure 6-12: Proposed coding matrix and associated metasurface.

It means that the number of elements "0" and "1" should be identical. This phenomenon is mostly attributed to the identical data entropy and the reciprocity fundamental between the element "0" and element "1". In order to achieve broadband RCS suppression, the combinational format optimization can be the best alternative for designing the reflective metasurface. In this study, an optimized format has been chosen by GSO algorithm. As shown in Figure 6-13, it is quite evident that how much the RCS reduction in a reflective metasurface for a normal incidence is improved when the number of elements "0" and "1"

become equal. It is also observed that broadband RCS reduction of the reflective metasurface with optimized coding matrix can be expanded from 5.1 GHz to 22.1 GHz (125%) for both x- and y-polarized incidence. It should be mentioned that the results for x- and y- polarizations are quite the same that is why those are not distinguished individually in the Figure 6-13.

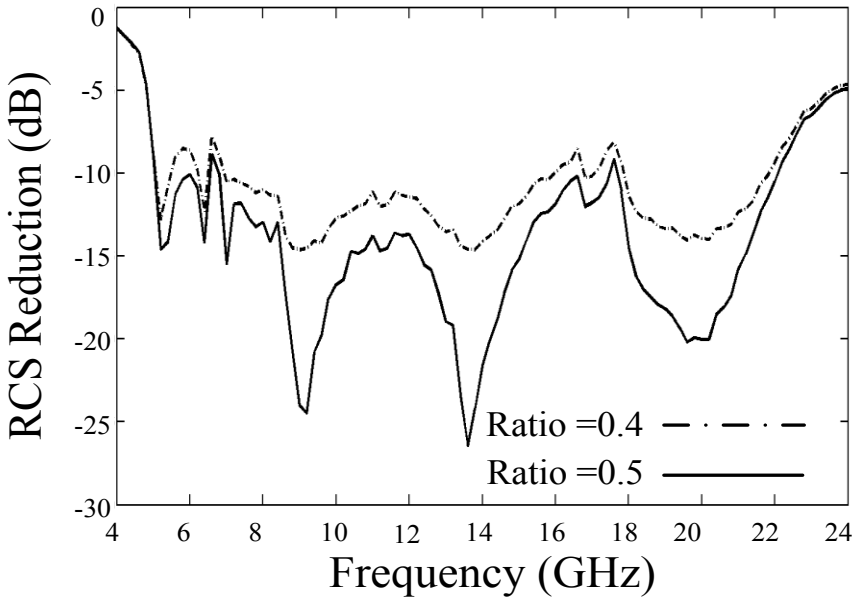

Figure 6-13: Normal incidence RCS reduction for different ratios versus frequency

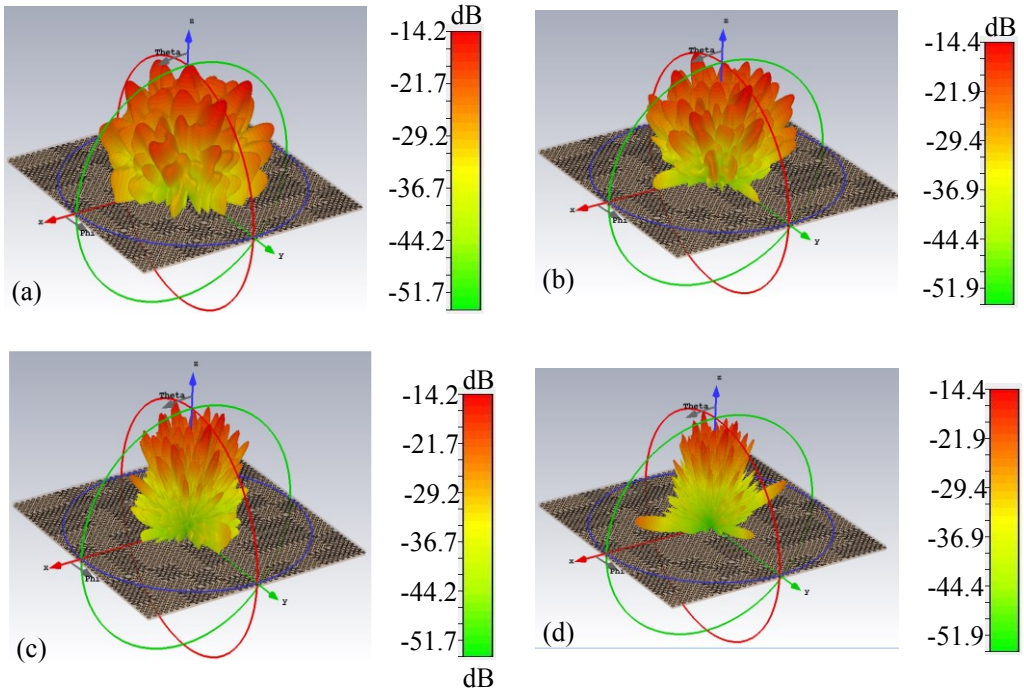

Figure 6-14: 3-D RCS pattern of the proposed metasurface under normal incidence at (a) 7 GHz, (b) 9.2 GHz, (c) 14 GHz, and (d)19.6 GHz.

The similarity of RCS reduction between x-polarization and y-polarization is attributed to the square matrix (M = N=10). The peaks of RCS reduction are obtained for reflective metasurface at 7 GHz, 9.2 GHz, and 13.6 GHz and 19.6 GHz approximately close to those in PCR curve in Figure 6-5(c). The 3-D RCS pattern of the proposed metasurface based on FSS at the resonant frequencies are illustrated in Figure 6-14. In comparison with 3-D RCS pattern of the uniform structures in the previous literature, it can be observed that the grating lobes are decreased and scattered fields are distributed more uniformly around. Meanwhile, it is interesting to mention that the maximum grating lobes have more than 14dB RCS reduction at the whole 3-D space concerning the same size of the metal surface. As aforementioned, using equation (6-4), the scattered fields can obviously be controlled through coding matrix of the reflective metasurface. For instance, once the FSS cells are set as elements either "0" or "1" as shown in Figure 6-15(a), $f_1(\theta,\varphi)=c_1(\cos\psi_1+\cos\psi_2)$ is simply derived; once the coding sequence is selected as shown in Figure 6-15(b), $f_2(\theta,\varphi)=c_2(\sin\psi_1+\sin\psi_2)$ is obtained, where c_1 and c_2 have constant values, $\psi_1=\frac{1}{2}kD(\sin\theta\cos\varphi+\sin\theta\sin\varphi)$ and $\psi_2=\frac{1}{2}kD(-\sin\theta\cos\varphi+\sin\theta\cos\varphi)$.

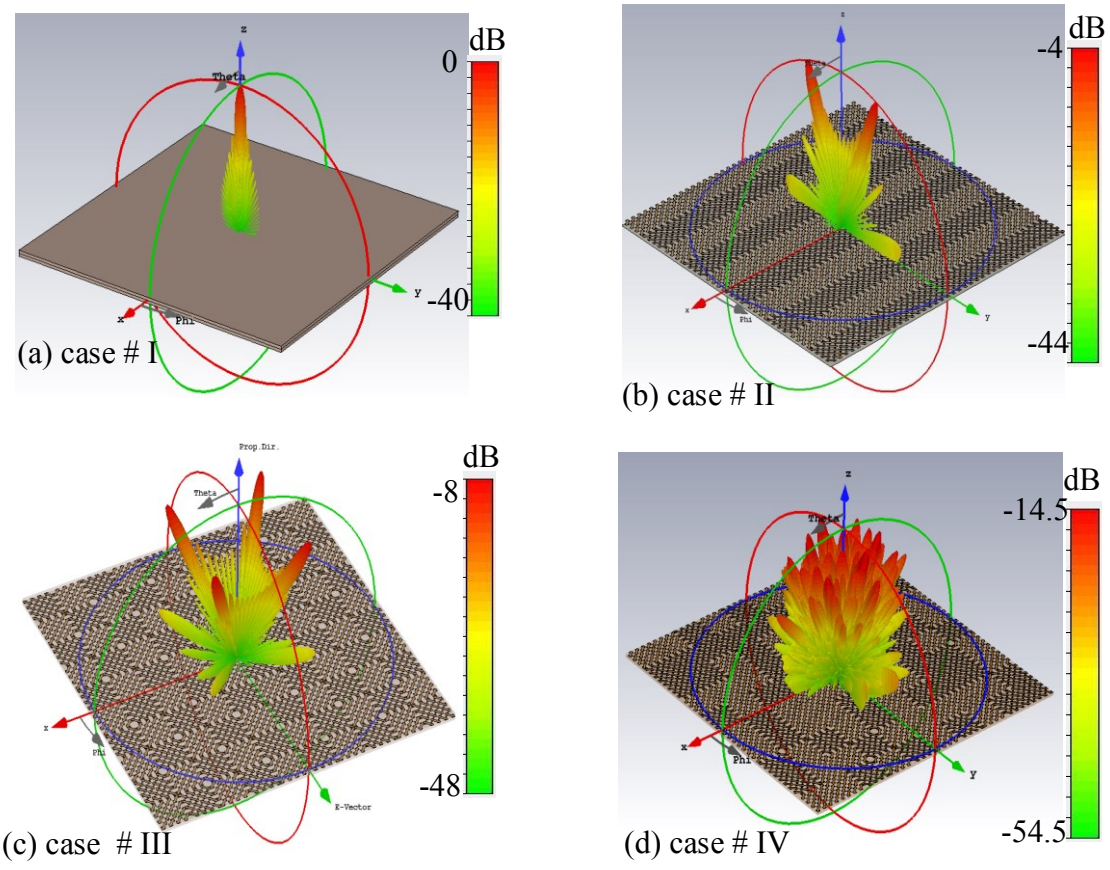

Figure 6-15: 3-D simulation patterns of periodic coding metasurfaces to indicate their ability to control scattering patterns using various coding sequences under the normal incidence of EM waves at the centre frequency 14 GHz. (a) case #I (000000…/000000...), (b) case #II (010101…/010101...), (c) case #III (010101…/101010...), and (d) case #IV (the proposed metasurface)

The investigation of the expressions above demonstrates that by the various coding structures, as exhibited in Figure 6-15, the normally incidences are scattered as a single principle beam, two main beams, and four major beams, respectively. The predictions based on the analyses are in acceptable agreement with the simulation results carried out using the commercial software CST Microwave Studio. From Figures 6-15 (b) and (c) can be found out that only the equal number of elements "0" and "1" without optimization algorithm can never be enough. In order to determine the RCS reduction behaviour of the designs for various cases (shown in Figure 6-15), Figure 6-16 is presented, where the proposed design (case # IV) suppresses the RCS greater than it in other designs (case # II and case # III). The broadband reflective metasurface is validated using simulation to quantify the RCS reduction of the design using CST at different incidence angles versus frequency under TM and TE polarizations, as exhibited in Figure 6-17.

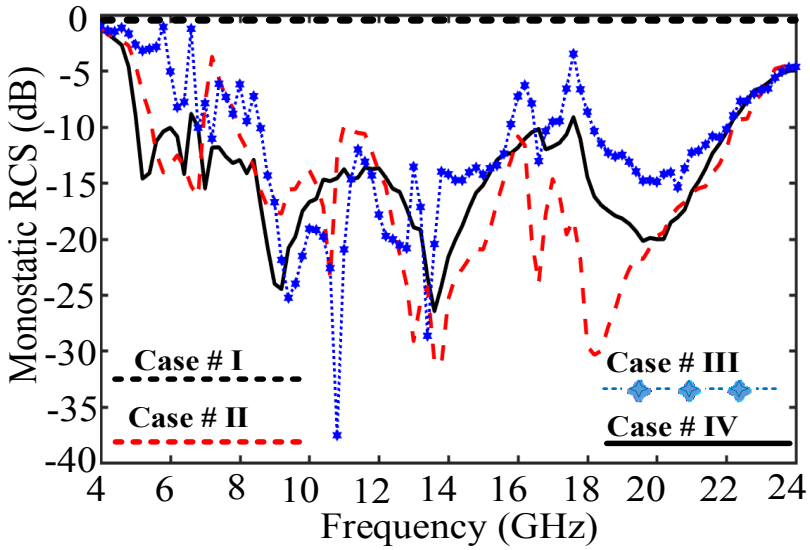

Figure 6-16: Normalized RCS reduction of the designs for the different cases (shown in Figure 6-15) at normal incidence with respect to an equal size metallic plate.

An RCS reduction less than −10 dB is obtained in a broad frequency range for both polarizations, and the RCS reduction was more than -10 dB at the 50° incidence. It can be found out that by increasing incident oblique angle θ from normal to 50°, the RCS reduction bandwidth is slightly decreased as it is expected before. The incident angle is obviously demonstrated to have a significant influence on the RCS reduction

bandwidth. In the case of oblique incidence as shown Figure 6-18, where EM waves run back and forth in a two-layer dielectric substrate, the propagation phase can be denoted as [152]

$$4\beta=\frac{4\sqrt{\varepsilon_r}k_o h}{\cos\theta_t} \tag{6-13}$$

Which is greater than that under normal incidence conditions. The additional propagation phase will generate a destructive interference condition at the surface of the metasurface and more affect the bandwidth. At higher frequencies, the additional propagation phase varies further extremely once θ_i is increased.

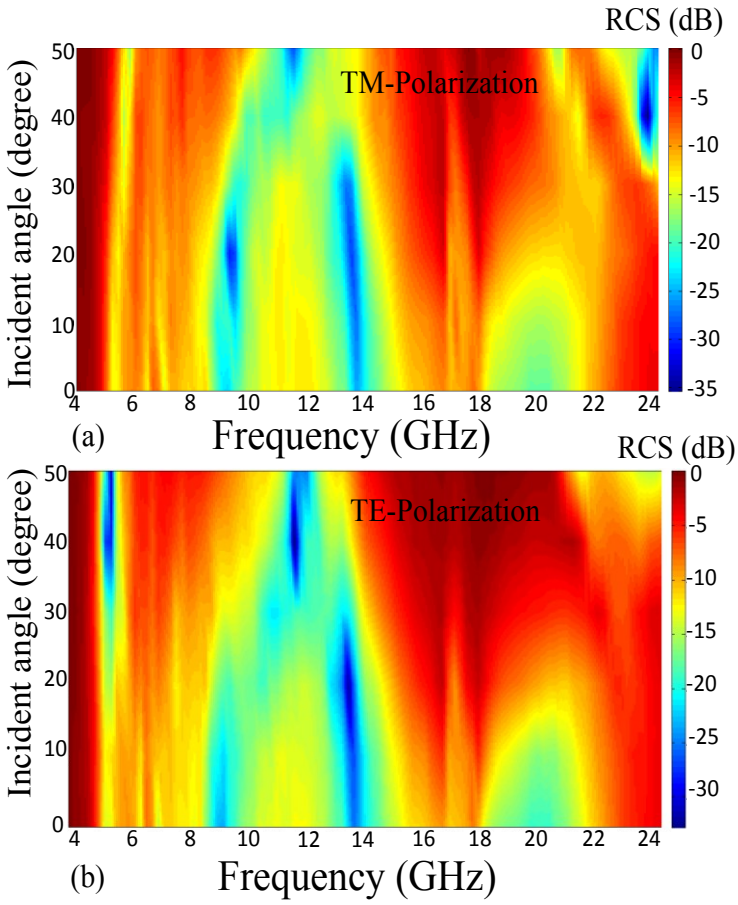

Figure 6-17: Maps of the simulated RCS reduction versus frequency range at different incidence angles for (a) TM and (b) TE polarizations.

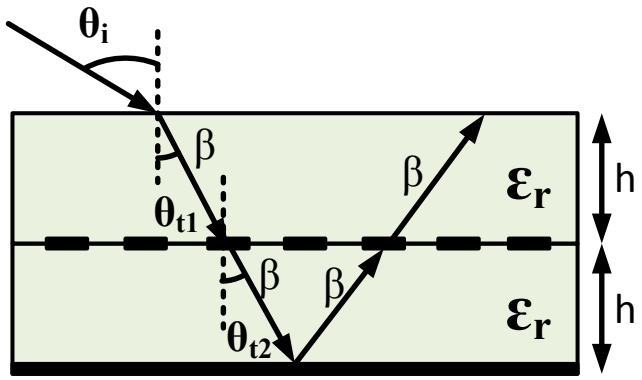

Figure 6-18: Diagrammatic sketch of EM wave propagation in a two-layer dielectric substrate at oblique incidence ($\theta_{t1} \simeq \theta_{t2} \simeq \theta_t$).

Moreover, a drop in the RCS reduction bandwidth for oblique incidence appears at around 17 GHz, which indicates that the EM energy is absorbed. This EM absorption originates from an extra resonance between the metallic ground and metasurface [152]. In order to further understand the performance of the proposed reflective metasurface, the RCS reduction bandwidth at various incidence angles under TM and TE polarizations are summarized in Table 6-3.

Table 6-3: Specular direction RCS reduction bandwidth for different incident angles

Incident angle θ	10-dB RCS reduction BW% TE-Polarization	10-dB RCS reduction BW% TM-polarization
0	125%	125%
10	124%	125%
20	110%	119%
30	81%	107%
40	61%	64%
50	52%	52%

It is interesting to mention that in spite of the set of negligible variations, the bandwidth preserves more than %110 for the incident angle up to 20° which verifies the least dependency of the proposed design to the incidence angle. However, the RCS reduction bandwidth for 30° incident angle is significantly dropped by 81% under TE polarization as compared with it under TM polarization. Therefore, the RCS reduction bandwidth approximately conserves property of the minimum tendency to TE and TM polarizations at

different incidence angles except for 30° which exist a difference 26% in the RCS reduction bandwidth between two polarizations. In order to verify the RCS suppression of the reflective metasurface by the optimized coding matrix, the near-fields of oblique incidence for both TE and TM polarizations at the centre frequency 14 GHz are depicted in Figure 6-19. The reflection-phase difference of 180° between two FSS elements “0” and “1” leads to the cancellation for the scattered waves, especially in the normal incidence. When the plane wave incidence impinges on the PEC plane and the coding metasurface individually, difference between the scattering waves becomes significant; the former wave is approximately a plane wave. Hence the far-field scattering pattern will generate a single beam, and RCS suppression will not generate at this frequency. However, in the case of the proposed coding metasurface, the reflection-phase difference of FSS cells is 180°, and the scattered wave is canceled. Therefore, the wavefront is wavy like, and far-field scattering pattern generates different beams in various directions. It can be observed that the near scattering fields have been directed at an incident angle not only of 0°, 20° but also of 40°. One should note that the components of scattering fields in TE and TM polarizations have been significantly steered by the suggested reflective metasurface because of the control of amplitude and phase by polarization conversion and the destructive interference by FSS cells “0” and “1” at 14 GHz.

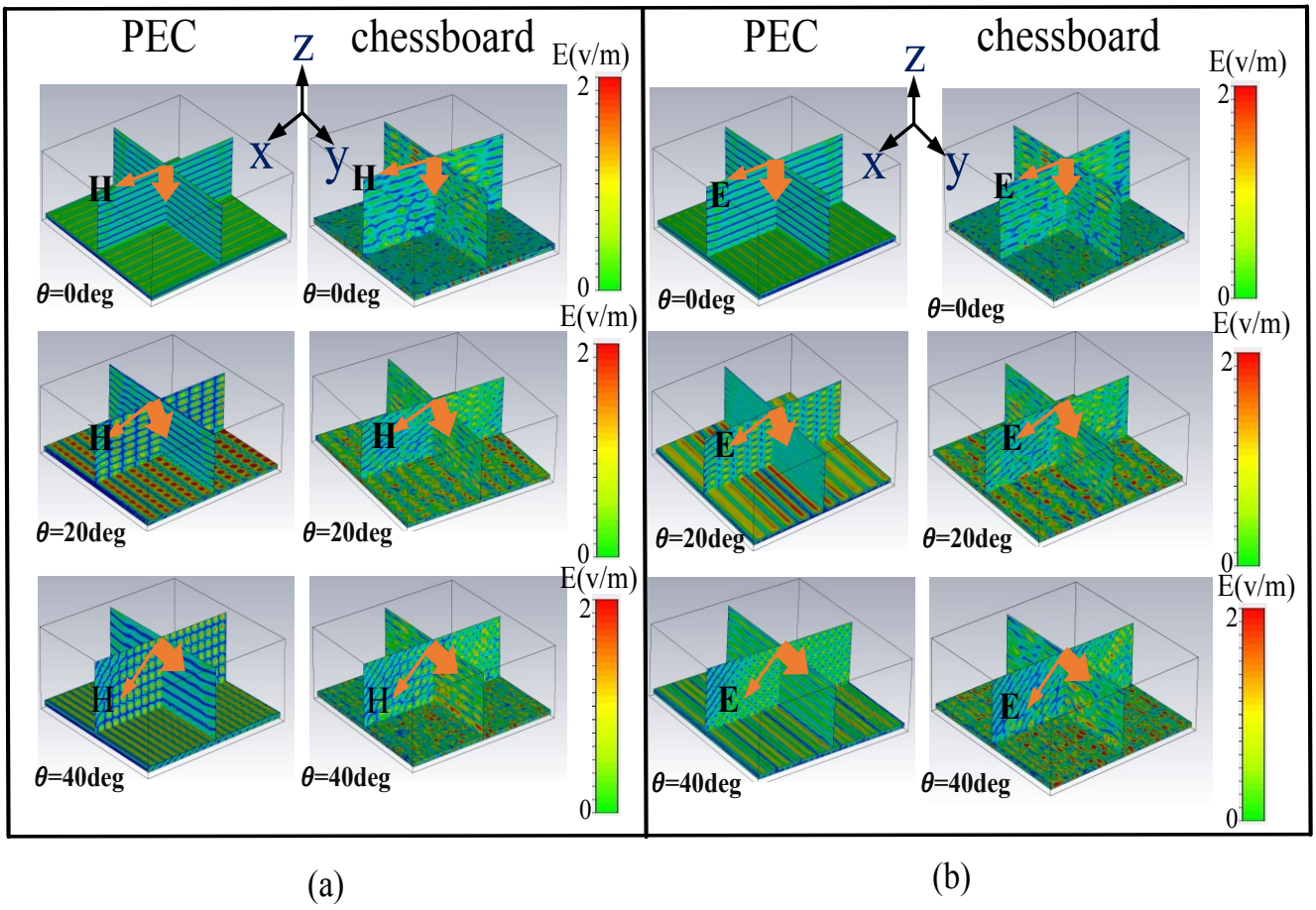

Figure 6-19: Near-fields of reflective metasurface with optimized coding matrix and PEC at 14 GHz for an incident angle of 0 deg, 20 deg, and 40 deg (a) TE polarization and (b) TM polarization.

From Figure 6-19, the variation disposition of the scattering fields is approximately uniform for the TE- and TM- polarized incidences as the incident angle varies from 0° to 40°.

6.1.5 Fabrication and Measurements

In order to experimentally validate the performance of the reflective metasurface with simulation results, the proposed two-layer design is fabricated and measured. The proposed two-layer structure is fabricated utilizing the standard printed circuit board (PCB) technology. Both substrates are RT/duroid 5880 with εr=2.2 and thickness 3.175mm. The photographs of the fabricated two-layer metasurface are shown in Figure 6-20. The entire size of the fabricated metasurface is 320×320mm^2. This size corresponds to a square structure composed by 10×10 elements of "0" and "1". Each FSS elements are simultaneously formed by 4×4 FSS cells, respectively. Meanwhile, the size each of FSS cells is 8mm. As shown in Figure 6-20, the first layer consists of the reflective coding matrix while the second layer (without any copper) is placed on the top. The purpose of using the second layer only is to broaden the RCS reduction bandwidth.

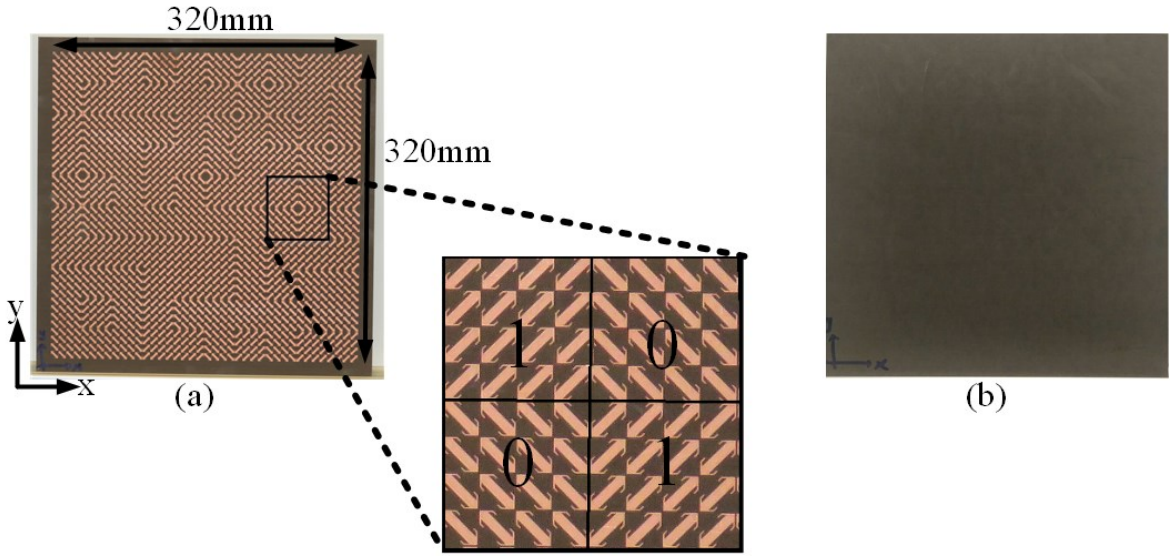

Figure 6-20: The photo of fabricated two-layer metasurface (a) bottom layer (reflective coding matrix metasurface) and (b) top layer (without any copper)

It should mention that in order to attach two layers to each other using screws, the main size of the structure is considered 10 mm greater than 320 mm. Because of the difficulties associated with bistatic measurements, just backscatter results (incident angle 0°) of the proposed reflective metasurface is experimentally measured in the anechoic chamber of the Concordia University. Two identical kinds broadband ridged horn antennas operating from 750 MHz to 18 GHz (ETS-Lindgren, #3115) and from 18 GHz to 40 GHz (Com-Power AH-840) are utilized as the transmitting and receiving antennas which are connected to two ports of an E8364B PNA 10 MHz to 50 GHz. The reflective metasurface is located far enough from the radar antennas inside the anechoic chamber in the far-field of the antennas to guarantee plane wave impingement, as exhibited in Figure 6-21.

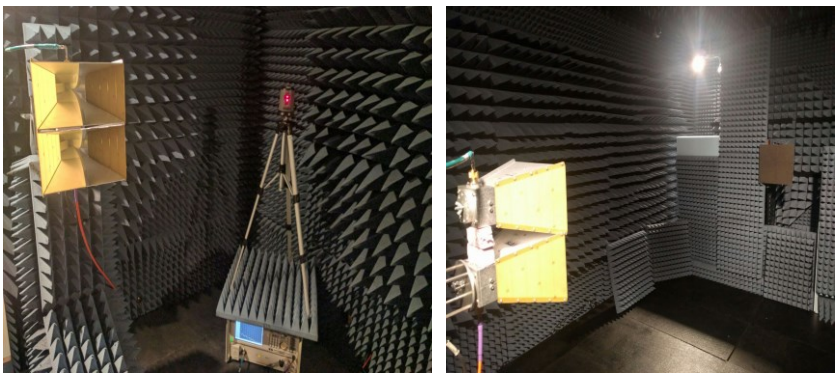

(a) (b)

Figure 6-21: (a) the same antennas as transmitting and receiving along E8364B PNA and (b) the measurement set up and the proposed fabricated design inside the anechoic chamber.

The backscatter is tested in two stages over the bandwidth of 4-18 GHz and then 18-24 GHz in the stepped frequency mode. In order to compute the RCS reduction, the scattering waves from metallic surfaces involving the equal sizes are measured as well. Due to restriction in the size of the anechoic chamber and inaccuracy in the target alignment and the fabrication, the negligible discrepancies are seen between simulation and experimental results. The simulation results for the monostatic RCS reflects a suppression of minimum 10 dB from 5.1 GHz to 22.1 GHz which compares approvingly to the measurements, as shown in Figure 6-22. An approximately 125% fractional bandwidth is achieved for both simulations and measurements. To clarify the capability the proposed design concerning the RCS reduction bandwidth at the normal incidence, it is compared with a series of similar structures reported in the references in Table 6-4.

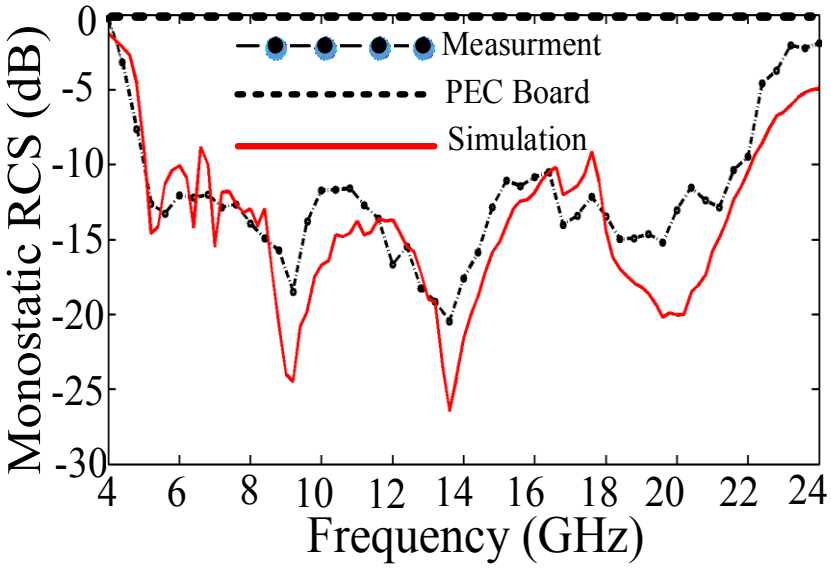

Figure 6-22: Normalized RCS reduction of the proposed reflective metasurface at normal incidence with respect to an equal size metallic plate. Solid and dashed lines represent: the simulated and measured diagrams, respectively.

Table 6-4: Comparison between similar designs and proposed metasurface under normal incident

Year/References	Frequency Band (GHz)	-10-dB RCS reduction B.W
2015/ [134]	4.1-7.6	63%
2013/ [135]	14.5-21.8	41%
2014/ [137]	9.5-15.8	50%
2017/ [141]	3.75-10	91%
2017/ [148]	7.5-13.2	60%
2015/ [149]	9-23	87%

2017/ [156]	6.1-17.8	98%
2015/ [157]	5.7-15.1	90%
Proposed	5.1-22.1	125%

It can be concluded that the metasurface has a wider bandwidth in terms of -10-dB RCS reduction as compared with the similar reported designs in the recent literature.

Broadband and High-Gain Low-RCS CP Antenna Based on FSS

In this section of this chapter, in order to reduce RCS, the second design including wideband CP antenna with low RCS and high gain properties is presented and investigated. The proposed antenna is based on a combination of the FPC and sequential feeding technique. The purpose of this antenna is to produce CP with the high directive level on wide bandwidth, whilst conserving low RCS. The principle of FPC and resonance is earned by employment one FSS metasurface. It is indicated that all the benefits above-mentioned can be attained over a wide frequency band by designing an appropriate FSS metasurface and modifying the feeding lengths to tune desirable phase. RCS suppression is realized by 180° $\pm$ 37° reflection phase variations between adjacent FSS unit cells on the metasurface. The experimental results show that the gain of the antenna with the metasurface is at least 8 dB greater than that of the primary antenna with a peak value approximately 20 dB at 28.5 GHz. Moreover, bandwidths of 3-dB gain, impedance ($|S11| \leq -10$ dB), and axial ratio (AR) ≤ 3 dB are ranged from 27.5 to 33.5 GHz (19.7%), 26.7 to 34.2 GHz (24.6%) and 26.8 to 33.1 GHz (21%), respectively. The monostatic RCS reduction for a normal incidence is effectively reduced from 28 to 48 GHz (52%).

6.1.6 Modelling and ANALYSIS

The proposed FPC antenna is initially examined with ray theory approach [57], which is convenient in realizing the operation fundamental of antenna gain increase and RCS reduction. The FPC antenna considered here consists of two reflectors and a small printed patch antenna. One of the two reflectors is the FSS metasurface used as a transmitting window, which permits the EM wave to transmit partially because

it is also named partially reflective surface (PRS). As shown in Figure 6-23 (a), the schematic view of the proposed FPC antenna for the goal of RCS reduction is presented. It is seen that the incident waves transmit through the metasurface, air gap, and the antenna's the second substrate, and then is reflected by the metallic ground. Hence, the operating principle of RCS suppression relies on destructive interference which is arranged by the combination of two kinds of FSS unit cells and FPC. It means that the unit cells are regarded as one box containing the metasurface, air gap, second substrate and metal ground plate, (see Figure 6-23). With respect to Figure 6-23 (a), the incident field (E_i) is equal to the sum of transmitted field (E_t) and reflected field (E_r) which is given as $E_i = E_r + E_t$ where $E_r = |E_r| e^{j\varphi_r}$ and $E_t = |E_t| e^{j\varphi_t}$.

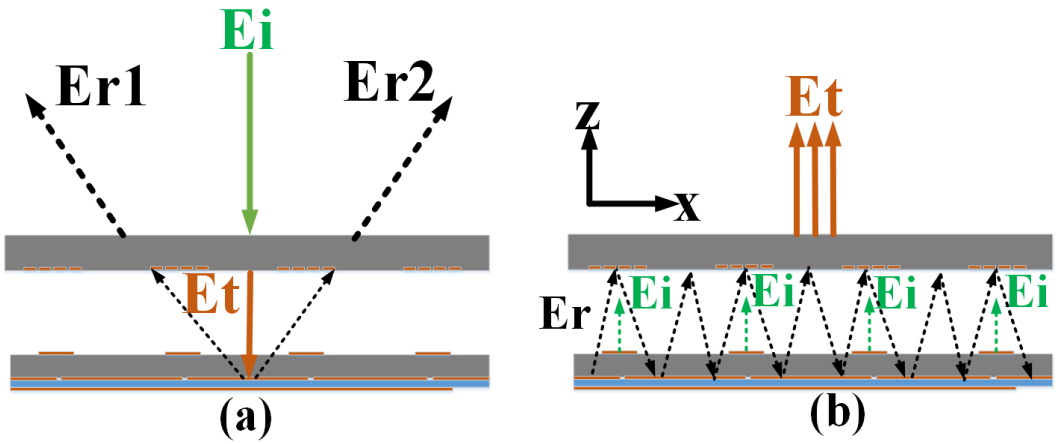

Figure 6-23: The schematic view of the proposed structure including the antenna with the FSS metasurface for two cases of (a) RCS reduction and (b) gain enhancement.

Here, because of two types of FSS unit cells, the reflected field is formed as $E_r = E_{r1} + E_{r2}$ where $E_{r1} = |E_{r1}| e^{j\varphi_{r1}}$ and $E_{r2} = |E_{r2}| e^{j\varphi_{r2}}$. So, the reflected waves produced by FSS#1 and FSS#2 generate destructive interference in the specular direction once $|\varphi_{r1} - \varphi_{r2}|$ is satisfying $|180° \pm 37°|$ as it is acceptable for low-RCS requirements. Moreover, the criteria of $|180° \pm 37°|$ relies on a compromise of in-band and out-of-band RCS suppression. Note that, the RCS suppression would be enhanced when reflection phase difference become roughly 180°, which is useful and efficient for in-band RCS suppression. However, it limits the bandwidth of low RCS. On the other hand, we should satisfy requirements related to the FSS metasurface or partially reflective surface (PRS). Once the FSS metasurface is located at a resonant air gap (cavity height) from source antenna which itself embedded in a metallic ground plate, the antenna gain is increased considerably, as shown in Figure 6-23 (b). The rays radiated by the source antenna are reflected multiple times with reducing amplitudes between the metasurface and the ground plane (see Figure 6-23 (b)). These

multiple reflections end up constructive interference and increase the antenna gain along the broadside considerably once the air gap "h" between the ground plate and the metasurface corresponds to [66]

$$h=\frac{\lambda}{4\pi}((\varphi)-2N\pi) \tag{6-14}$$

$$\varphi=\varphi_{\text{sub, airgap}}+\varphi_{FSS} \tag{6-15}$$

in which φ and λ are the reflection phase of FPC and free space wavelength, respectively. N is an integer and order of resonant mode (N = 0, 1, 2…). In addition, as N is increasing the side-lobe levels become greater.

6.1.7 Antenna Design

The geometry of a two-layer single element antenna fed by aperture coupling is depicted in Figure 6-24. It consists of two substrates: the bottom substrate is Rogers RO3006 whilst the top one is Rogers RT/duroid 5880 with an x-shaped slot etched off the metallic ground [4]. As shown in Figure 6-24, a parallel feeding technique as one of the sequential feeding networks is presented. This structure is based on the architecture presented by the authors in [4]. The feeding network is an anti-phase equal power divider which this feeding network has four output ports with 90° phase delay in an anti-clockwise sequence, as shown in Figure 6-25. Note that, in order to have a design freedom to optimize the phase in final design, the authors consider parameter "L" connected to the four output ports as a variable design parameter. One should note that, since parameter "L" has a 50-ohm characteristic impedance, its length variations do not impact the impedance matching of the feeding network.

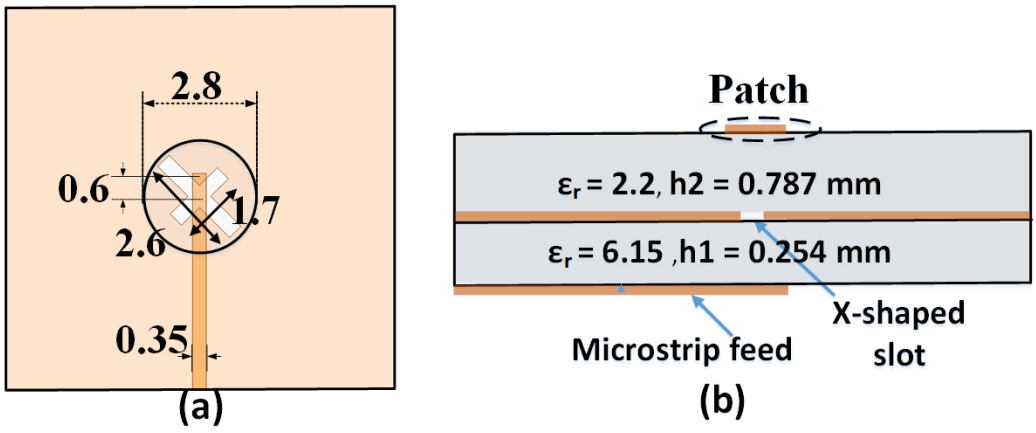

Figure 6-24: The geometry of patch antenna (a) top view and (b) side view [4].

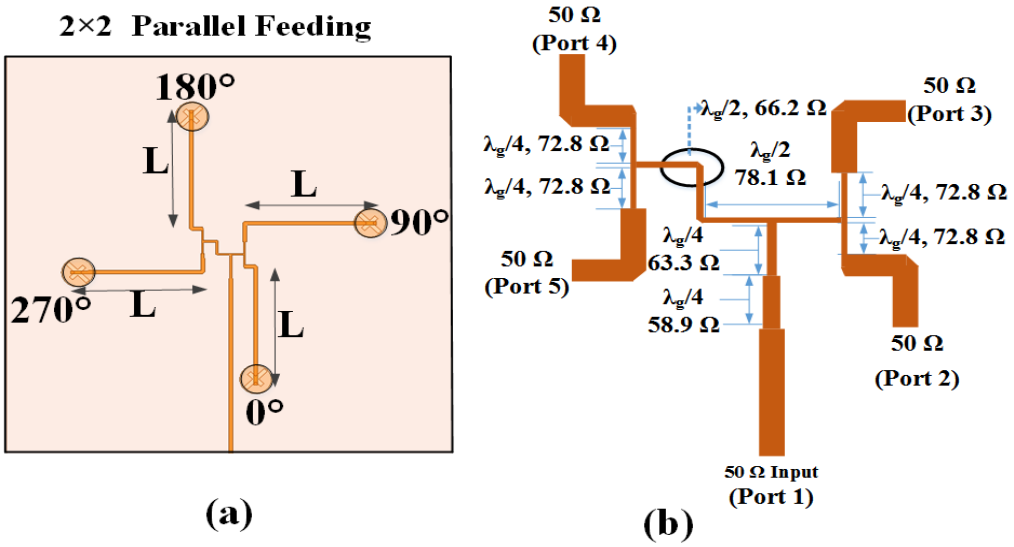

Figure 6-25: The sequential feeding network (a) 2×2 antenna subarrays and (b) parallel feeding (RHCP) [4] (L=12mm).

6.1.8 FSS Cell

In order to suppress RCS, two different FSS unit cells with various reflection phase responses are necessary. In terms of modeling and analysis mentioned above and also prevent any mistakes, the FSS unit cells are regarded as a box containing the metasurface, air gap, second substrate and metallic ground, as depicted in Figure 6-26.

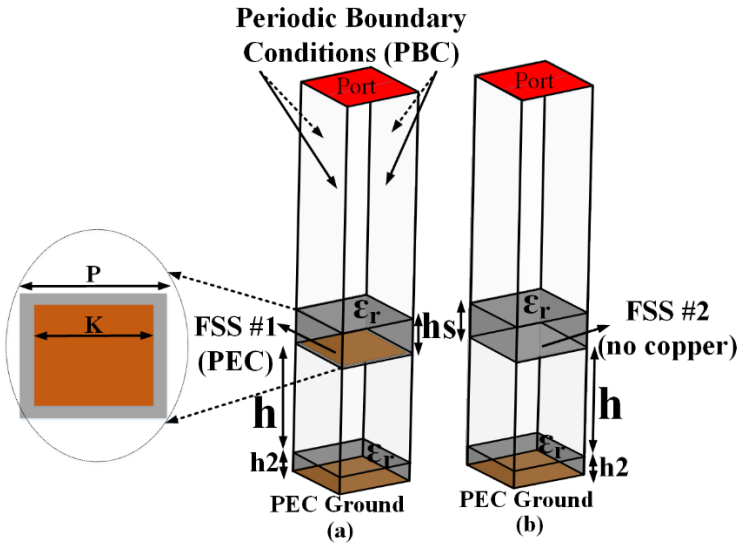

Figure 6-26: The simulated models of the FSS unit cells (a) FSS#1 and (b) FSS#2 (P=3.5mm, K=3.2mm, h=4.8mm, h2=0.787mm, hs=1.52mm, εr=2.2).

To fully investigate the reflection features of the FSS unit cells, the full-wave numerical analysis is performed in Ansys HFSS utilizing a unitary cell under proper periodic boundary conditions (PBC) and

floquet port excitation. Apparently, the FSS unit cell analysis approach not only reduces the computation time but also accurately anticipates the reflection and transmission coefficients as compared to treating the entire superstrate layer. The relative permittivity and dielectric loss tangent are 2.2 and 0.0009, respectively. The difference between FSS #1 and FSS #2 is only the copper patch while all dimensions and materials are identical. For FSS #1, a copper patch is printed on the bottom surface of superstrate, as shown in Figure 6-26 (a). In order to realize the reflection frequency response of FSS unit cells, the simulation results of reflection coefficients for both magnitude and phase are exhibited in Figure 6-27. From Figure 6-27 (a), it can be seen that magnitude of the reflection coefficient for both the FSS cells are greater than 0.99 which ensures the high gain with respect to (6-16) as follows [57]

$$Dr=\frac{\left(1+\left|\Gamma\left(f,\theta=0\right)\right|\right)}{\left(1-\left|\Gamma\left(f,\theta=0\right)\right|\right)} \tag{6-16}$$

Where Dr is the relative directivity on the broadside direction $(\theta=0)$ and Γ is the magnitude of the reflection coefficient. Moreover, the half-power fractional bandwidth (HPBW) of highly reflecting superstrate with frequency dependent reflection characteristics can be calculated using (6-17) as follows [57].

$$HPBW=\frac{\Delta f}{f_0}=\frac{\lambda}{2\pi h}\frac{1-\Gamma}{\sqrt{\Gamma}} \tag{6-17}$$

As one can observe from (6-16), the directivity is based on the reflectivity (Γ) of the metasurface so that directivity (Dr) increases significantly by reflectivity (Γ). Therefore, high directivity is achieved with a greatly reflective screen. However, from (6-17) it can be realized that bandwidth reduces as (Γ) increases, and a narrow BW is predicted for air gap.

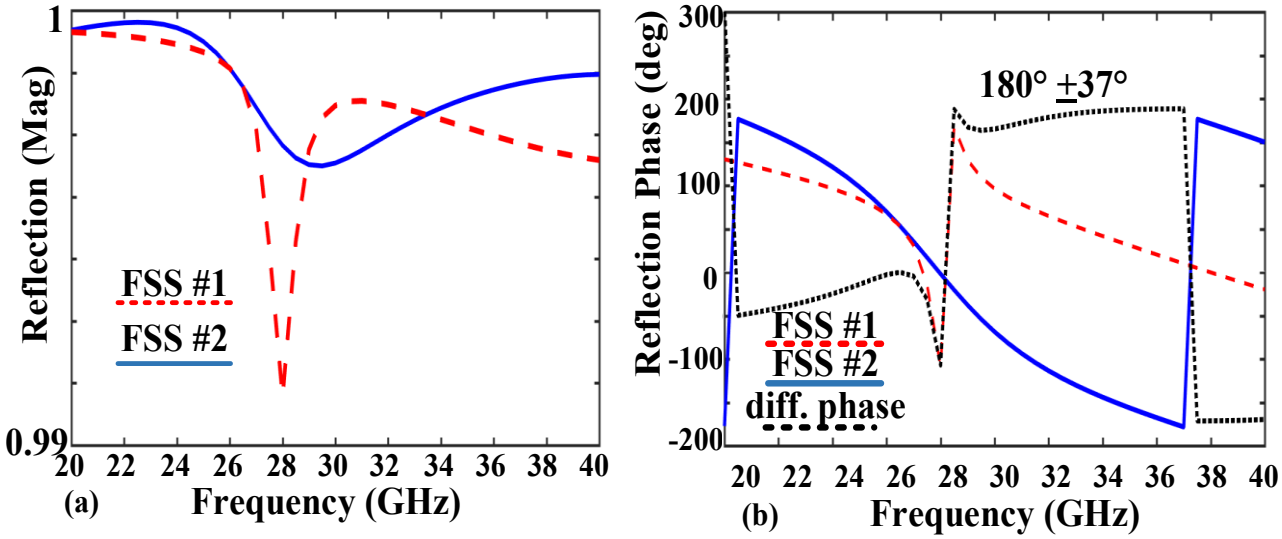

Figure 6-27: The reflection coefficients of FSS units (a) magnitude and (b) phase.

The best alternative to address this problem is to optimize the reflectivity (phase and magnitude) using (6-14) to (6-17) [57]. After the optimization process by HFSS, the reflection phase of both the FSS unit cells and also the difference between those computed as shown in Figure 6-27 (b). it can be observed that the phase difference of the reflected waves remains in the range 180°±37° from 28.2 GHz to 48 GHz (52%). Therefore, a wideband RCS reduction (nearly 52%) for the proposed structure is expected.

6.1.9 FPC Antenna Structure

The proposed source antenna excited by a sequential-phase feed (see Figure 6-25). To form the FPCA, the FSS layer is placed over the source antenna at an air gap of "h". As shown in Figure 6-28, all material and thickness of the proposed FPC antenna are given, as well. Figure 6-29 shows the top view of the FSS metasurface, where to satisfy the RCS reduction requirements, each FSS structure is formed by 4×4 FSS unit cells with an entire dimension of 14×14 mm (see Figure 6-29). Note that, the copper patches of FSS #1 are printed on the bottom surface of the superstrate. So, initially, by selecting suitable the air gap "h", the broad impedance bandwidth of the source antenna must be conserved. Second, gain enhancement is acquired by the FPC formed by the metasurface and the metallic ground. Third, to protect CP feature of the source antenna, the appropriate arrangement of the FSS unit cell is needed. Fourth, by the FSS layer backed by the ground plate, a reflective broadband RCS reduction is attained. Evidently, it is complicated to optimize the four functions simultaneously. Hence, our goal is to acquire a compromise between above features. The FSS metasurface is designed with respect to the following procedure.

(i) Design the FSS unit cell with determining the reflectivity properties according to the flat phase to generate the broadband FPC and the highest magnitude to enhance directivity or gain. (Figure 6-26 and Figure 6-27)

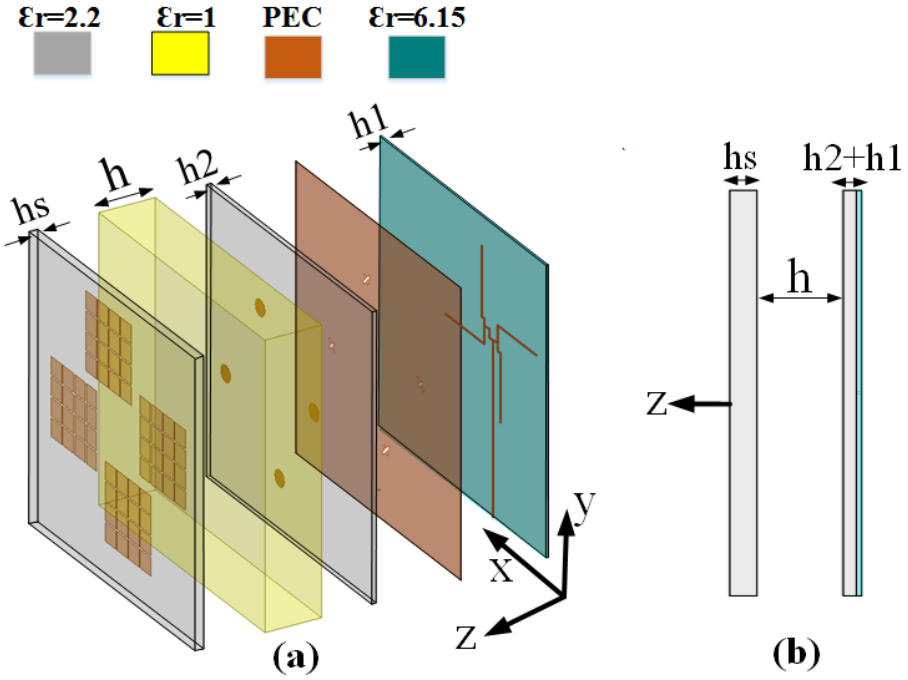

Figure 6-28: (a) The 3-D configuration and (b) side view of the FPC antenna (h1=0.25mm, h2=0.787mm, h=4.8mm, hs=1.52mm).

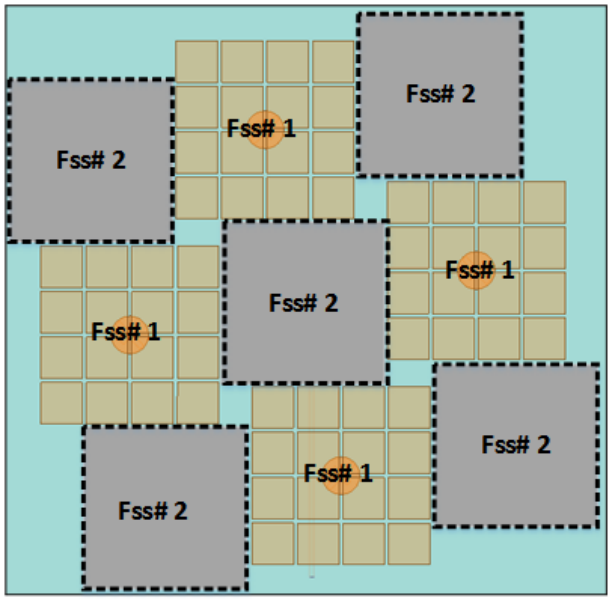

Figure 6-29: The FSS metasurface including structures of FSS#1 and FSS#2, (each FSS structure is formed by 4×4 FSS unit cells).

(ii) Find the proper air gap “h” between the source antenna and the FSS metasurface to cover the preferable impedance bandwidth of the antenna (26–34 GHz).

(iii) Arrange the FSS unit cells in terms of the number and the place at the bottom of the metasurface to fulfil the CP-wave requirements including generate, preserve, and expand 3dB axial-ratio (AR) bandwidth.

(iv) Reduce the wideband RCS by 180° $\pm$ 37° reflection phase variations between adjacent FSS unit cells (FSS #1 and FSS #2). One should note that FSS #2 must somehow behave not to deteriorate the other factors generated by FSS #1 such as the impedance and CP bandwidths and gain enhancement (see Figure 6-26 and Figure 6-27).

(v) Optimize length of parameter “L” with a characteristic impedance of 50 ohms to adapt the phases and earn an appropriate trade-off between four main factors (impedance and CP bandwidths, gain enhancement, RCS reduction).

In order to compare the simulation results of the reflection coefficient and axial ratio, and gain for both source antenna without the metasurface and the suggested FPC antenna (with the metasurface) Figure 6-30 is presented. One should note that after optimization by Ansys HFSS the air gap between the source antenna and the metasurface acquired 4.8 mm (close to half a wavelength). With respect to Figure 6-30, it is observed that impedance bandwidth the source antenna and FPC antenna (with metasurface) are ranged from 25.6 to 34.5 GHz (29.6 %) and 26.5 to 35 GHz (27.6 %), respectively.

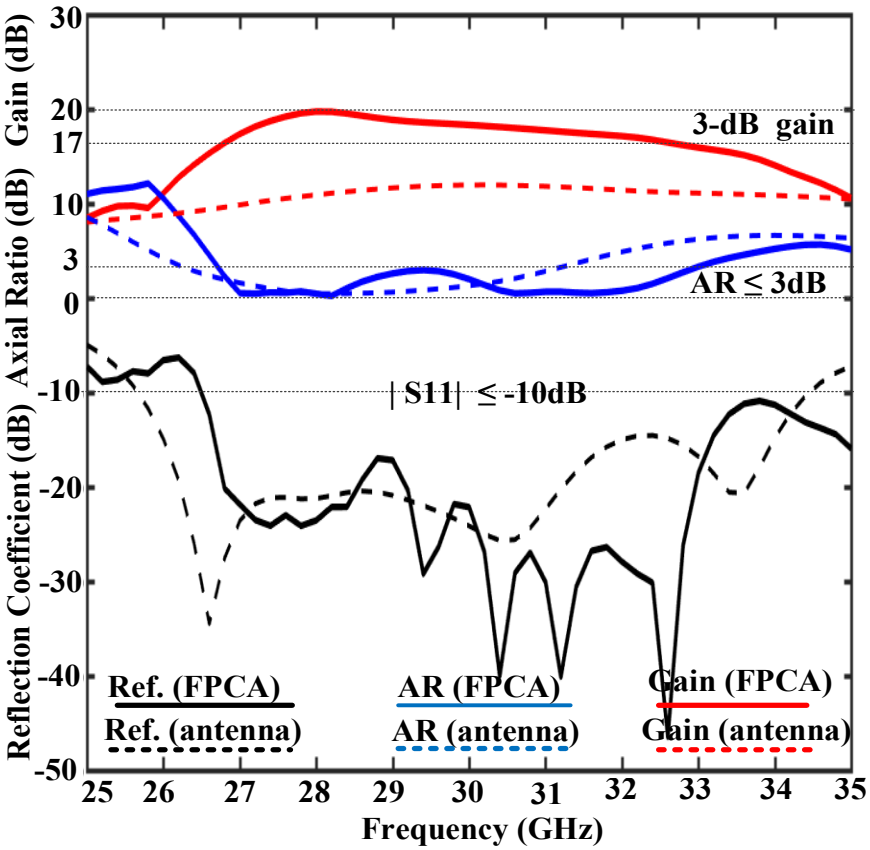

Figure 6-30: The simulated gain, AR, and reflection coefficient, for both the source antenna (without metsurface) and the FPC antenna (with metasurface).

Those have a great agreement because the air gap (h=4.8 mm) is approximately half a wavelength of free space. The simulated 3-dB AR bandwidth for the source antenna at broadside is extended from 26.3 to 31.2 GHz (17 %) whilst it for the FPC antenna is ranged from 26.5 GHz to 32.9 GHz (21.5 %) showing the metasurface fulfils the CP-wave requirements, namely, produce, protect, and extend 3dB axial-ratio (AR) bandwidth. As shown in Figure 6-30, the simulated 3-dB gain bandwidth for the source antenna is from 26.4 to 35 GHz (28 %) with the maximum gain of 12 dB at 29 GHz, which is less than it for the FPC antenna, expanding from 26.8 GHz to 32.6 GHz (19.5 %) with peak gain of 20 dB at 28 GHz. It can be realized that the FSS metasurface increases the peak gain by 10 dB at 28 GHz. As aforementioned above, for the suggested design, the parameter "L" gives a design freedom to optimize all the pointed factors such as the gain, AR, and RCS. Thus, in order to examine the structure performance with "L" parameter variations Figures 6-31 and 6-32 are given. From Figure 6-31 it can be found out that the performance of radiation and impedance of the proposed antenna under "L" parameter variations is trivial. However, to make an appropriate decision concerning the best value "L", the scattering behaviour (monostatic RCS) for various values of "L" should be considered.

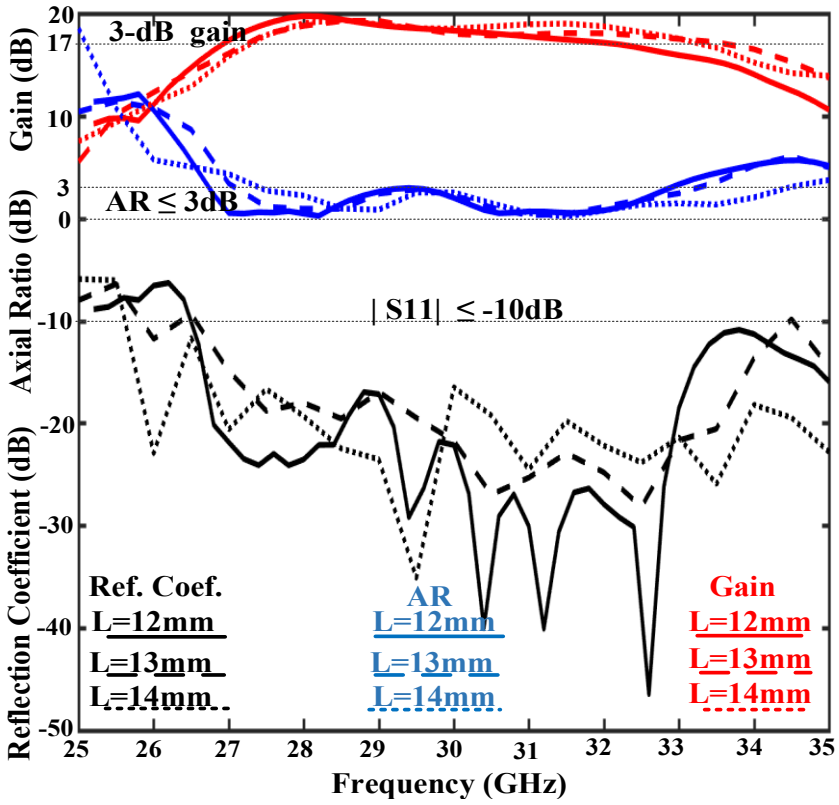

Figure 6-31: The simulated reflection coefficient , AR, and gain for FPC antenna (with metasurface) for "L" parameter variations.

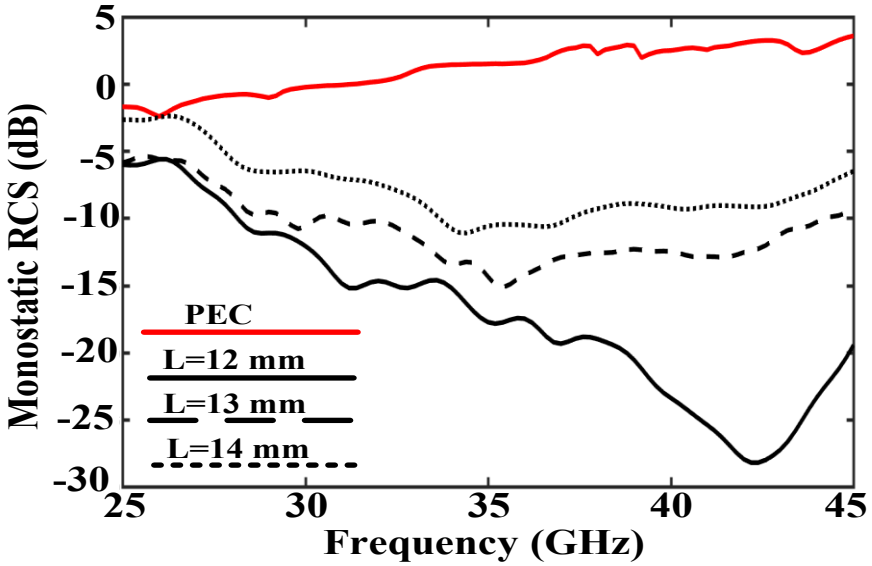

Figure 6-32: The monostatic RCS comparison of the FPC antenna with both the proposed and PEC metasurface with "L" parameter variations.

As shown in Figure 6-32, it can be concluded that the monostatic RCS variations in the normal incidence for different values of "L" is significant. Consequently, with respect to Figure 6-32, to fulfil the RCS suppression requirement, the best value of "L" corresponds to 12 mm.

6.1.10 Experimental Results

To validate the great impedance, radiation, and scattering performance of the proposed structure, the prototype of FPC antenna is implemented utilizing common printed circuit board (PCB) fabrication approach. The photograph of the assembled fabricated antenna is exhibited in Figure 6-33.

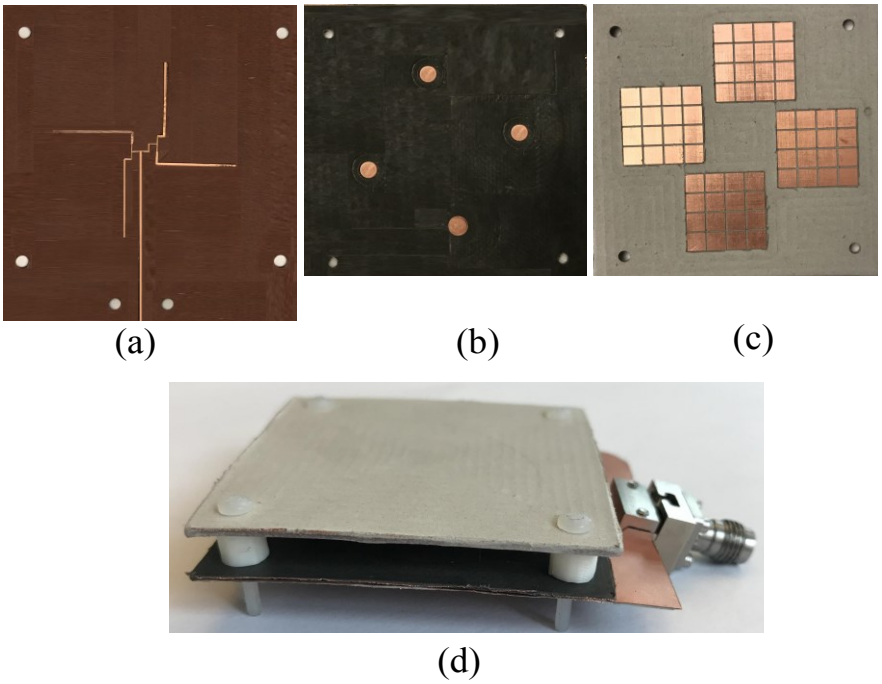

Figure 6-33: The photo of the assembled fabricated antenna (a) the sequential feeding, (b) the patch, and (d) the FSS metasurface, and (e) the proposed FPCA.

The RHCP and LHCP fields and then AR of the proposed FPC antenna are computed by measured $E_\theta = |E_\theta|$ and $E_\varphi = |E_\varphi|$ as follows [66]

$$\vec{E}_{RHCP} = \frac{}{\sqrt{2}}(\vec{E}\theta + j\vec{E}\varphi), \ \vec{E}_{LHCP} = \frac{}{\sqrt{2}}(\vec{E}\theta - j\vec{E}\varphi) \tag{6-18}$$

$$AR\ (dB) = 10\ log\left(\frac{|\vec{E}_{RHCP}| + |\vec{E}_{LHCP}|}{|\vec{E}_{RHCP}| - |\vec{E}_{LHCP}|}\right) \tag{6-19}$$

The measured and simulated results of the total gain, axial ratio (AR), and reflection coefficient are compared with each other, as exhibited in Figure 6-34.

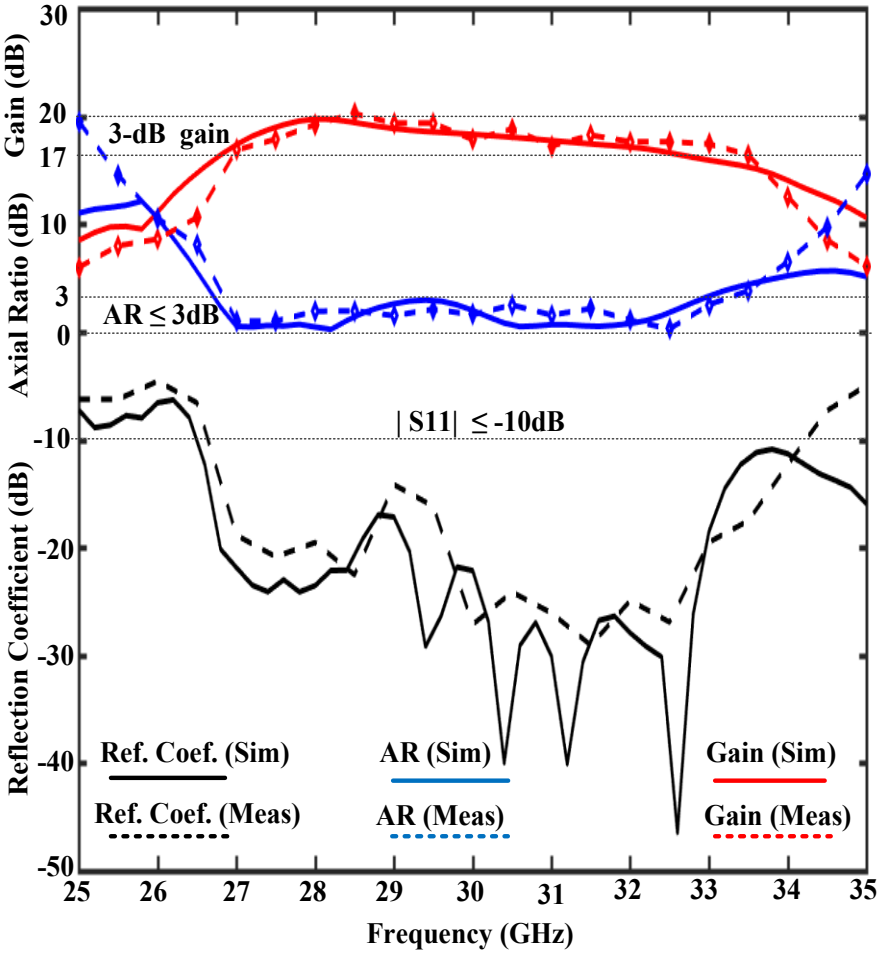

Figure 6-34: The simulated and measured reflection coefficient , AR, and gain for FPC antenna (with metasurface).

It can be observed there exist an excellent agreement between simulations and measurements so that reflection coefficient ($|S_{11}| \leq -10dB$) of the fabricated FPC antenna is extended from 26.7 to 34.2 GHz (24.6 %). The simulated and measured AR and gain at broadside is shown in Figure 6-34, as well. The measured 3-dB AR bandwidth is 21%, expanding from 26.8 to 33.1 GHz while the measured 3-dB gain bandwidth is 19.7%, ranging from 27.5 to 33.5 GHz with a peak gain of approximately 20 dB at 28.5 GHz. The normalized simulations and measurements of RHCP and LHCP gain for the FPC antenna at φ=45° for three frequencies of 27.5, 30, and 33 GHz are demonstrated in Figure 6-35. The maximum radiation all occurs at broadside orientation and the significant gain difference is observed between RHCP and LHCP in the main beam for the three frequencies. It is also found out that with the frequency increment from 28 GHz to 33 GHz, side-lobe level (SLL) is increasing which inherits the radiation features of the source antenna. In addition, the measured patterns have considerable resemblance trends with simulated ones. To validate the effectiveness of the proposed design on RCS suppression, the FPC antenna is terminated with match load and placed vertically on a foam platform.

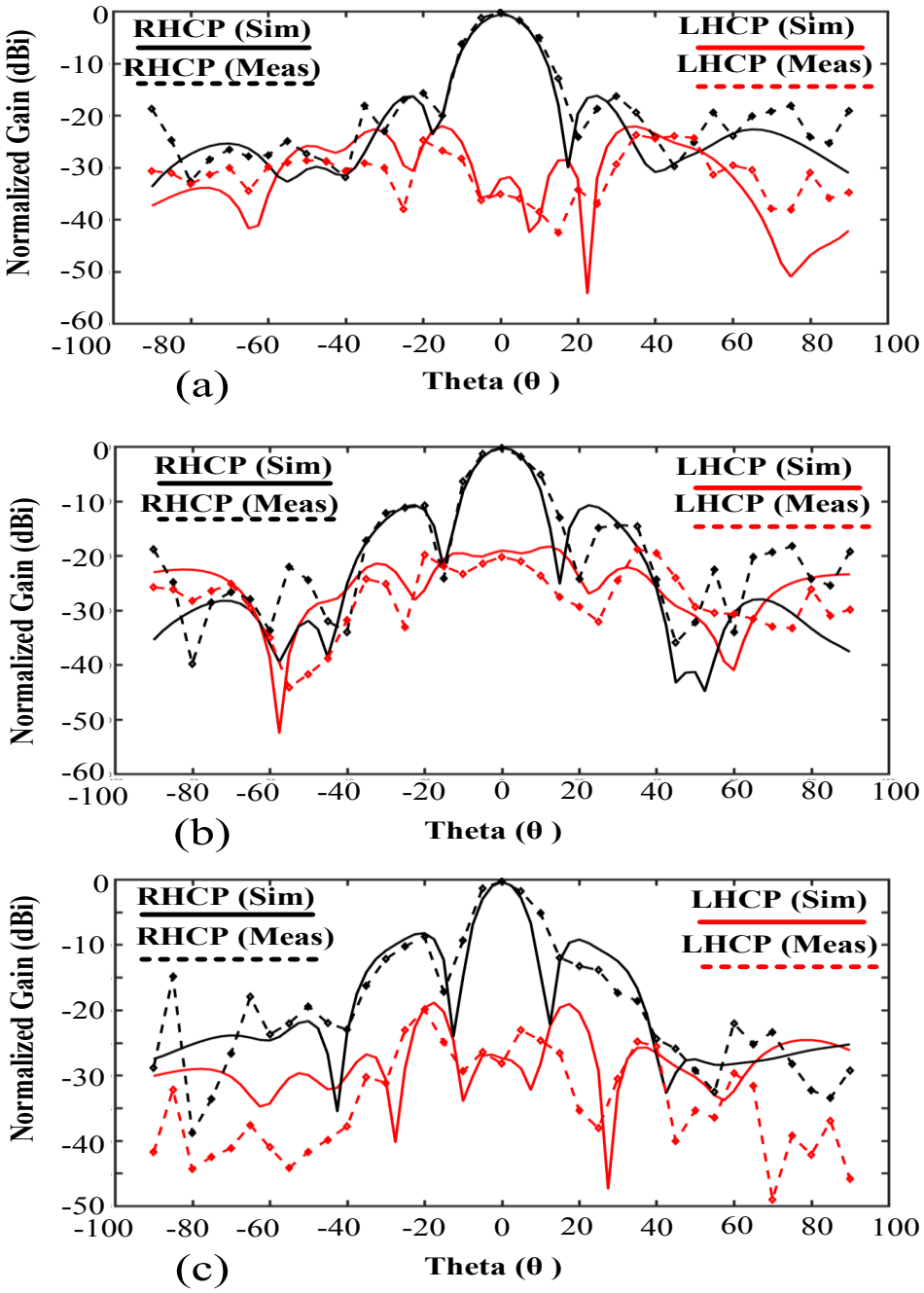

Figure 6-35: The normalized simulations and measurements of RHCP and LHCP gain at φ=45° for the FPC antenna at three frequencies of (a) 27.5 GHz, (b) 30 GHz, and (c) 33 GHz.

Two types of horn antennas for transmitting and receiving which are connected to an E8364B PNA (10 MHz to 50 GHz) placed in front of the FPC antenna. Note that, due to the set of difficulties associated with bistatic measurements, only backscatter results (under normal incidence) of the proposed FPC antenna is experimentally measured in the anechoic chamber of the Concordia University. Meanwhile, the FPC antenna terminated with a matching load is placed far enough from the antennas inside the anechoic chamber in the far-field of the horn antennas to ensure plane wave impingement. One should note that to

calculate the RCS reduction, measurement of the scattering waves from the metallic metasurface with the identical size are essential, as well. The measured and simulated monostatic RCS of both the FPC antenna and the metallic metasurface with the same size under normal incidence is shown in Figure 6-36.

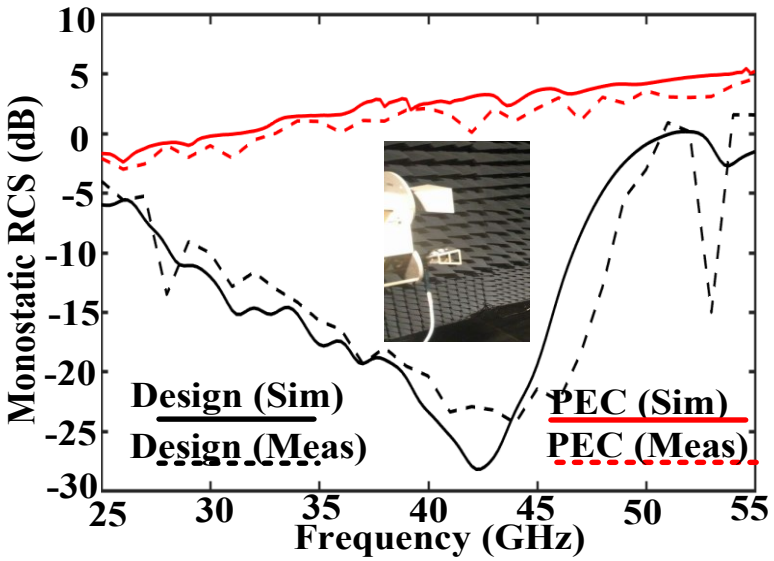

Figure 6-36: The simulated and measured monostatic RCS of the proposed FPC antenna and the PEC metasurface with the identical size under normal incidence, the photo of two types of horn antennas used for transmitting and receiving.

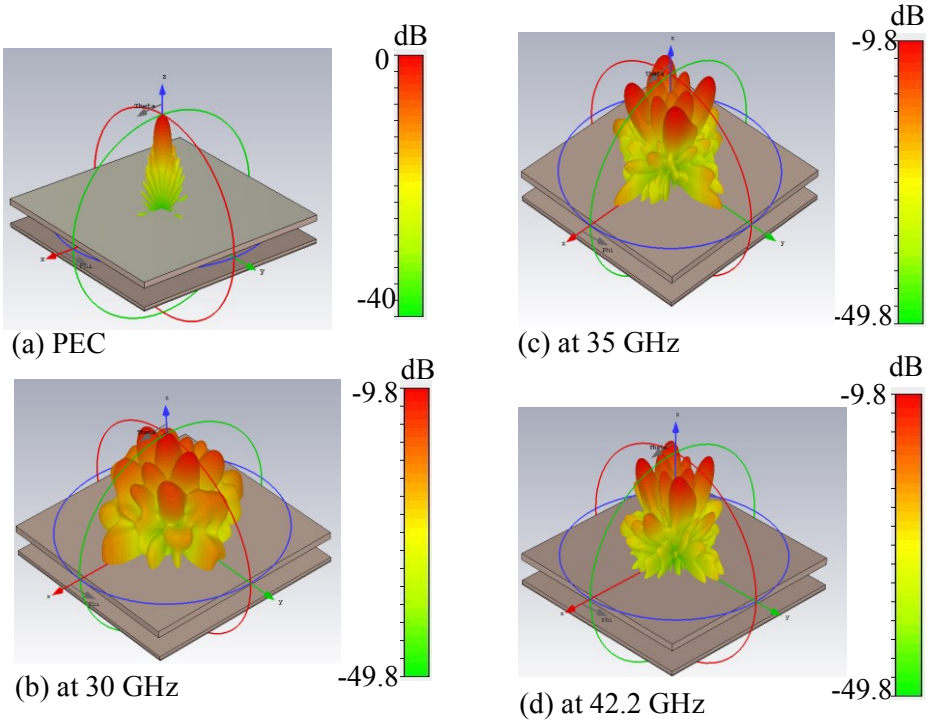

Figure 6-37: The 3-D RCS pattern of the FPC antenna terminated with the matching load under normal incidence for (a) particular case of the mettalic plate, the proposed metasurface at (b) 30 GHz, (c) 35 GHz, and (d) 42.2 GHz. (the plots are normalized with a metallic plate)

It can be observed that considerable RCS reduction is obtained from 28 to 48 GHz with a relative bandwidth of 52 %, covering the in- and out-band. The 3-D RCS pattern of the FPC antenna at different frequencies of 30 GHz, 35GHz, and 42.2 GHz are shown in Figure 6-37. In comparison with 3-D RCS pattern of the metallic metasurface with the same size (see Figure 6-37 (a)), it can be found out that the grating lobes are chiefly diminished by the proposed metasurface and scattered fields are distributed further uniformly around.

Table 6-5: Comparison between the proposed structure with the similar designs in reference

Year/ Reference	**Impedance B.W. (GHz) and (%)**	**CP property/ Relative 3-dB AR B.W. (%)**	**Relative 3-dB Gain B.W. (GHz)**	**Peak Gain (dB)**	**RCS Reduction B.W. (GHz)**
2014/ [158]	11.2-12.0 (6.9%)	LP/ -	3.7	13.5	80
2015/ [159]	9.0-9.9 (9.5%)	LP/ -	17.3	13	54.5
2015/ [160]	9.9-10.9 (9.6%)	LP/ -	N/A	10.8	85.7
2016/ [161]	5.4-5.8 (7.1%)	LP/ -	7.5	9.5	66.7
2016/ [162]	9.5-10.9 (13.7%)	LP/ -	7.0	11.0	133.3
2018/ [163]	9.4-11.3 (18.3%)	LP/ -	16.6	10.5	76.9
Proposed	26.7-34.2 (24.6%)	CP/ 21	19.7	20	52

6.1.11 Conclusion

As the first design of this chapter, a new binary coding matrix with an optimal arrangement of the FSS cells on the metasurface to reduce the RCS on a wide frequency range has been proposed. The coding matrix has been attained using group search optimization (GSO) algorithm. Also, a theoretical analysis has been carried out on the ratio of the “0” and “1” elements using Least Square Error (LSE) method to achieve the best ratio value so that the optimum value of the ratio as a new constraint is considered in GSO algorithm. The simulations and measurements are in acceptable agreement with a considerable reduction of the RCS over a wide frequency range from 5.1 GHz to 22.1 GHz (125%) at the normal incidence for both polarizations. As the second design of this chapter, a broadband low-RCS, high directivity (gain), and CP antenna by employing the FSS metasurface at the Ka-band has been presented. The RCS reduction has been attained because of phase cancellation of two types of FSS structures which are formed by 4×4 FSS unit cells. The structure of FSS unit cell is new so that it consists of three layers terminated by the metallic plate of the source antenna. This approach prevents any deterioration in both radiation performance and scattering property of the FPC antenna at the identical frequency. In addition, the proposed structure has been based on FPC and resonance. Also, a microstrip slot array excited by a sequentially rotated feeding

network has been applied as the source antenna to illuminate the FSS metasurface. The experimental results indicate that by the employment of the FSS metasurface the structure gain has been enhanced at least 7 dB as compared with it for the source antenna without the metasurface while the gain peak reaches nearly 20 dB at 28.5 GHz. Furthermore, bandwidths of 3-dB gain, impedance ($|S11| \leq -10$ dB), axial ratio (AR) ≤ 3 dB, and monostatic RCS reduction are 19.7%, 24.6%, 21%, and 52%, respectively. It is worth mentioning that approach introduced provides a new strategy to give an alternative to solve the confliction between radiation and scattering performance of a source antenna. This type of antenna can be used to the set of conditions in which RCS suppression and gain enhancement are both necessary, such as stealth platforms.

Chapter 7. Conclusion and Future Work

Conclusion

At millimetre-wave (MMW) frequencies, losses associated with wireless link and system are main issues of concerns and need to be overcome in designing high-performance wireless systems. In order to compensate the overall loss in a MMW wireless communication system, a high-gain antenna is demanded. In addition, circularly polarized (CP) antennas are among desired options because they offer many benefits such as great resistance to polarization mismatch, mitigation of multipath effects, and some phasing issues and immunity to Faraday's rotation. On the other hand, frequency selective surface (FSS) technology is recently employed to enhance the performance of radiation and scattering properties of antennas utilized in various sectors such as aerospace, medical, and microwave industry. In this thesis, we propose the use of FSS technology to design practical and efficient CP antennas. Consequently, CP Fabry-Perot cavity (FPC) antennas based on FSS are investigated in this thesis to fulfil the growing demand for broadband high-gain antennas with low radar cross section (RCS). In light of this, the thesis studied performance enhancement of radiation and scattering features of CP antennas employing FSS structures. The thesis' main contribution is to develop CP antennas with high directive level on wide bandwidth, whilst conserving low RCS.

A comprehensive literature review and basic principles governing the operation and analysis of FSS are presented in Chapter 2. Chapter 2 also presented a short history and background along with diverse practical applications. In addition, the various types of element shapes were given.

In chapter 3, a high gain CP dielectric resonator (DR) antenna was suggested. Applying an FSS superstrate layer, a gain improvement of 8.5 dB is attained. A detailed theoretical analysis along with various models were proposed and utilized to optimize the superstrate size and the air gap height between the antenna and superstrate layer.

In Chapter 4, two reduction techniques of spatially coupling are investigated. An effective approach for reducing the near-field coupling between 2×2 CP-MIMO antennas around 30 GHz was first presented. Due to the concentration of the power density using the FSS superstrate, an enhancement in the structure gain and improvement in isolation are achieved. Also, a short investigation on the reflected power density by the FSS superstrate in the near-field area is performed. It was found out that by adjusting few design parameters, the reflections can be redirected far from the antenna's main beam to prevent any interference. The study also compared the mutual coupling between CP-MIMO antennas when the patches are radiating in air and in the presence of FSS layers. In the second design of spatially coupling reduction, an FSS polarization-rotator wall for reducing the spatially coupling between two DR antennas in a MIMO system

is designed and proposed. Using this FSS wall, the TE modes of the antennas become orthogonal, which reduces the spatially coupling between the two DRAs. The guidelines for designing the DRA and FSS unit cell are discussed in details. The investigation depicted that the proposed FSS wall has the capability to enhance the isolation between the radiating elements without disturbing the performances of the DRAs with respect to both radiation pattern and input impedance.

In Chapter 5, a new LP-to-CP-polarizer based on multilayer FSS slab in Ka-band is presented. Results indicated that the polarizer is able to transform an LP wave to a pure CP wave over a broad frequency band with a trivial insertion loss. The transmitted CP wave by the polarizer was approximately robust under oblique illuminations. The polarizer is fabricated and measured by a wideband horn antenna verifying the simulated results. To have a high-gain CP antenna, an 8-element LP array antenna with Chebyshev tapered distribution was designed and integrated with the polarizer. It is observed that this polarizer with the antenna array was an acceptable candidate for several applications including satellite communications, orthogonal polarization transformers, sub-reflectors, and CP lenses.

In chapter 6, initially, as the first structure, to suppress the RCS on a broad frequency band, a new binary coding matrix with an optimal arrangement of the FSS cells on the metasurface band proposed. The coding matrix acquired using group search optimization (GSO) algorithm. Also, a theoretical analysis carried out on the ratio of the “0” and “1” elements using Least Square Error (LSE) method to achieve the best ratio value. This optimum value of the ratio utilized as a new constraint in GSO algorithm. As the second design of this chapter, a broadband low-RCS, high gain, and CP antenna by employing the FSS metasurface at the Ka-band presented. The RCS reduction obtained due to phase cancellation of two types of FSS structures. This approach prevented any deterioration in radiation performance and scattering property of the FPC antenna. It is worth mentioning that the introduced approach provides a new strategy to address the conflict requirements between radiation and scattering performance of a source antenna. This type of antenna can be used to provide both RCS suppression and gain enhancement requirements for different systems such as stealth platforms. This work can be considered as a step toward the standardization of the frequency selective surface technology.

Future Work

This work can be extended by exploring other transmission-type or reflection-type surfaces based on the frequency selective surface (FSS) technology such as coding diffuse surfaces, LP conversion metasurface based on grounded vias, and reflective anisotropic surfaces for cross polarization rotation.

New polarizers based on FSS with different properties can have the extensive potential for research subjects. These surfaces enable the deployment of the FSS technology in future communication systems in the commercial and industrial sectors. In addition, the active components can be a very useful extension of this work.

Bibliography

[1] M. Sun, Z. Ning Chen, and X. Qing, "Gain enhancement of 60-GHz antipodal tapered slot antenna using zero-index metamaterial," IEEE Trans. Antennas Propag., vol. 61, no. 4, pp. 1741-1746, 2013.

[2] B. Glushko, D. Kin, and A. Shar, "Gigabit optical wireless communication system for personal area networking," Opt. Memory Neural Netw., vol. 22, no. 2, pp. 73–80, 2013.

[3] FCC, "First report and order, revision of part 15 of the commission's rules regarding ultra-wideband transmission systems", FCC02- 48, 2002.

[4] M. Akbari, S. Gupta, M. Farahani, A. R. Sebak, and T. Denidni, "Analytic study on CP enhancement of millimetre wave DR and patch subarray antennas," International Journal of RF and Microwave Computer-Aided Engineering, vol. 27, pp. 2−11, 2017.

[5] M. Kalhor, J. Nourinia, Ch. Ghobadi, M. Akbari, and N. Felegari, "Circularly polarized antenna for WLAN and WiMAX applications. ," International Journal of RF and Microwave Computer-Aided Engineering, vol. 22, pp. 329−335, 2012.

[6] A. Perron, T. Denidni, and A. Sebak, "A Low-cost and high-gain dual polarized wideband millimetre-wave antenna", Antennas and Propagation, EuCAP European Conference. pp. 3558–3561, 2009.

[7] C.-Y. Huang, J.-Y. Wu, and K.-L. Wong, "Cross-slot-coupled microstrip antenna and dielectric resonator antenna for circular polarization," IEEE Trans. Antennas Propag., vol. 47, no. 4, pp. 605–609, 1999.

[8] C. A. Balanis, Antenna Theory: Analysis and Design, 3rd ed. Wiley, 2012.

[9] K. Davies and E. K. Smith, "Ionospheric effects on satellite land mobile systems," IEEE Antennas Propag. Mag., vol. 44, no. 6, pp. 24–31, 2002.

[10] T. Manabe, Y. Miura, and T. Ihara, "Effects of antenna directivity and polarization on indoor multipath propagation characteristics at 60 GHz," IEEE J. Sel. Areas Commun., vol. 14, no. 3, pp. 441–448, 1996.

[11] K. W. Leung, W. C. Wong, K. M. Luk, and E. K. N. Yung, "Circular-polarized dielectric resonator antenna excited by dual conformal strips," Electron. Lett., vol. 36, no. 6, pp. 484–486, 2000.

[12] N. Ghassemi, W. Ke, S. Claude, Z. Xiupu, and J. Bornemann, "Low-cost and high-efficient w-band substrate integrated waveguide antenna array made of printed circuit board process," IEEE Trans. Antennas Propag, vol. 60, pp. 1648-1653, 2012.

[13] B.A. Munk, "Frequency-selective surfaces: theory and design," Wiley, New York, 2000.

[14] T. K. Wu, "Frequency-selective surface and grid array," Wiley, New York, 1995.

[15] J. C. Vardaxoglou, "Frequency-selective surfaces: Analysis and design," Research Studies Press, Ltd., Taunton, UK, 1997.

[16] G. Marconi and C.S. Franklin, "Reflector for use in wireless telegraphy and telephony," U.S. Patent, 1,301,473 1919.

[17] B. Cahill and E. Parker, "Field switching in an enclosure with active FSS screen," Electron. Lett., vol. 37, pp. 244-245, 2002.

[18] J. C. Batchelor, E. A. Parker, B. Sanz-Izquierdo, J.-B. Robertson, I.T. Ekpo and A.G. Williamson, "Designing FSS for wireless propagation control within buildings," Antennas & Propagation Conference, Loughborough, 2009.

[19] A. Newblold, "Designing buildings for the wireless-age [FSS]," Communications Engineer, vol. 2, pp. 18-21, 2004.
[20] E. Parker, S. Massey, M. Shelley and R. Pearson, "Application of FSS Structures to Selectively Control the Propagation of signals into and out of buildings Annex 5: Survey of Active FSS," Tech. Rep. Ofcom AY4464A Project, 2004.
[21] E. Parker and S. Savia, "Fields in an FSS screened enclosure," in Microwaves, Antennas Propag., IEE Proceedings, pp. 77-80, 2006.
[22] Q. Nidal, "Enhancing wireless communication system performance through modified indoor environments," PhD diss., © Nidal Qasem, 2014.
[23] M. Gustafsson, A. Karlsson, A. P. Rebelo, and B. Widenberg, "Design of Frequency Selective Windows for Improved Indoor Outdoor Communication," IEEE Trans. Antennas Propag., vol. 54, no. 6, pp. 1897-1900, 2006.
[24] E. L. Pelton and B. A. Munk, "Scattering from periodic arrays of crossed dipoles," IEEE Trans. Antennas Propag., no. 3, pp. 323–330, 1979.
[25] S. M. A. Hamdy and E. A. Parker, "Current distribution on the elements of a square loop frequency selective surface," Electron. Lett., vol. 18, no. 14, pp. 624–626, 1982.
[26] E. A. Parker and S. M. A. Hamdy, "Rings as elements for frequency selective surfaces," Electron. Lett., vol. 17, no. 17, pp. 612–614, 1981.
[27] E. A. Parker, S. M. A. Hamdy, and R. J. Langley, "Arrays of concentric rings as frequency selective surfaces," Electron. Lett., vol. 17, no. 23, pp. 0–1, 1981.
[28] S. W. Lee, G. Zarrillo, and C. L. Law, "Simple formulas for transmission through periodic metal grids or plates," IEEE Trans. Antennas Propag., vol. 30, no. 5, pp. 904–909, 1982.
[29] E. A. Parker, "The Gentleman's guide to frequency selective surfaces," 17th Q.M.W Antenna Symposium, April, pp. 1–18, 1991.
[30] N. Marcuvitz, Waveguide Handbook. IET, 1951.
[31] G. Trentini, "Partially reflecting sheet arrays," IRE Trans. Antennas Propag., vol. 4, pp. 666-671, 1956.
[32] D. R. Jackson and N. G. Alexopoulos, "Gain enhancement methods for printed circuit antennas," IEEE Trans. Antennas Propag., vol. 33, pp. 976-987, 1985.
[33] D. R. Jackson and A. A. Oliner, "A leaky-wave analysis of the high-gain printed antenna configuration," IEEE Trans. Antennas Propag., vol. 36, pp. 905-910, 1988.
[34] M. Thevenot, M. S. Denis, A. Reineix, and B. Jecko, "Design of a new photonic cover to increase antenna directivity," Microwv. Opt. Technol. Lett., vol. 22, no. 2, pp. 136-139, 1999.
[35] A. Ip and D. R. Jackson, "Radiation from cylindrical leaky waves," IEEE Trans. Antennas Propag., vol. 38, no. 4, pp. 482-488, 1990.
[36] Y. J. Lee, J. Yeo, and R. Mittra, "Design of a high-directivity electromagnetic bandgap (EBG) resonator antenna using a frequency-selective surface (FSS) superstrate," Microw. Opt. Technol. Lett., vol. 43, pp. 462–467, 2004.
[37] A. P. Feresidis and J. C. Vardaxoglou, "High gain planar antenna using optimised partially reflective surfaces," Proc. Inst. Elect. Eng. Microw. Antennas Propag., vol. 148, pp. 345–350, 2001.
[38] D. R. Jackson, P. Burghignoli, G. Lovat, F. Capolino, C. Ji, D. R. Wilton, and A. A. Oliner, "The fundamental physics of directive beaming at microwave and optical frequencies and the role of leaky waves," Proceedings of the IEEE, vol. 99, pp. 1780-1805, 2011.

[39] Z. G. Liu, "Fabry-Perot Resonator Antenna," Journal of infrared millimetre and terahertz waves, vol. 31, pp. 391-403, 2010.
[40] T. X. Zhao, D. R. Jackson, J. T. Williams, and A. A. Oliner, "General formulas for 2-D leaky wave antennas," IEEE Trans. Antennas Propag., vol. 53, , no. 11, pp. 3525-3533, 2005.
[41] T. Zhao, D. R. Jackson, J. T. Williams, H. Y. D. Yang, and A. A. Oliner, "2-D periodic leaky wave antennas-part I: metal patch design," IEEE Trans. Antennas Propag., vol. 53, no. 11, pp. 3505- 3514, 2005.
[42] T. Zhao, D. R. Jackson, and J. T. Williams, "2-D periodic leaky-wave antennas-part II: slot design," IEEE Trans. Antennas Propag., vol. 53, no.11 , pp. 3515-3524, 2005.
[43] D. R. Jackson, A. A. Oliner, and A. Ip, "Leaky-wave propagation and radiation for a narrow beam multiple-layer structure," IEEE Trans. Antennas Propag., vol. 41, no. 3, pp. 344-348, 1993.
[44] R. Gardelli, M. Albani, and F. Capolino, "Array thinning by using antennas in a Fabry-Perot cavity for gain enhancement," IEEE Trans. Antennas Propag., vol. 54, no. 7, pp. 1979-1990, 2006.
[45] G. Lovat, P. Burghignoli, and D. R. Jackson, "Fundamental properties and optimization of broadside radiation from uniform leaky-wave antennas," IEEE Trans. Antennas Propag., vol. 54, no. 5, pp. 1442-1452, 2006.
[46] G. Lovat, P. Burghignoli, F. Capolino, and D. R. Jackson, "Highly-directive planar leaky-wave antennas: a comparison between metamaterial-based and conventional designs," in Proc. Europ. Microw. Assoc., pp. 12-21, 2006.
[47] T. Tamir, "Leaky-wave antennas," in Antenna Theory, R. E. Colin and F. J. Zucker, Eds., ed New York: McGraw Hill, 1969.
[48] A. A. Oliner, "Leaky-wave antennas," in Antenna Engineering Handbook, R. C.Johnson, Ed., ed New York: McGraw Hill, 1993.
[49] R. K. Mongia and A. Ittipiboon, "Theoretical and experimental investigations on rectangular dielectric resonator antennas," IEEE Trans. Antennas Propagat., vol. 45, no. 9, pp. 1348-1356, 1997.
[50] K.M. luk and k.w. Leung, "Dielectric resonator antennas," Research Studies Press Ltd. Baldock, Hertfordshire, England, 2003.
[51] A. Pirhadi, H. Bahrami, and J. Nasri, "Wideband high directive aperture coupled microstrip antenna design by using a FSS superstrate layer," IEEE Trans. Antennas Propagat. vol. 60, no. 4, pp. 2101-2106, 2012.
[52] D. M. Pozar, Microwave Engineering, Fourth Edition, Wiley, 2012.
[53] A. Foroozesh and L. Shafai, "investigation into the effects of the patch-type FSS Superstrate on the high-gain cavity resonance antenna design," IEEE Trans. Antennas Propag., vol. 58, no. 2, pp. 258-270, 2010.
[54] B. Han, X. Yang, and H. Xue, "A millimeter-wave fabry-perot antenna with high-gain and circular polarization operation," Antennas and Propagation, 3rd Asia-Pacific Conference, pp. 40-43, 2014.
[55] S. l. S. Yang, R. Chair, A. Kishk, K. F. Lee, and K. M. Luk. "Study on sequential feeding networks for subarrays of circularly polarized elliptical dielectric resonator antenna," IEEE Trans. Antennas Propag., vol. 55, no. 2, pp. 321–333, 2007.
[56] D. R. Smith, D. C. Vier, Th. Koschny, and C. M. Soukoulis, "Electromagnetic parameter retrieval from inhomogeneous metamaterials," Physical Rev. E, vol. 71, 036617, 2005.

[57] A. P. Feresidis and J. C. Vardaxoglou, “High gain planar antenna using optimised partially reflective surfaces,” IEE Proc Microw Antennas Propag., vol. 148, no. 6, pp. 345–50, 2001.
[58] A. R. Weily, K. P. Esselle, T. S. Bird, and B. C. Sanders, “Dual resonator 1-D EBG antenna with slot array feed for improved radiation bandwidth”. IET Microw. Antennas Propag., vol. 1, no. 1, pp. 198–203, 2007.
[59] R. Alkhatib and M. Drissi, “Improvement of bandwidth and efficiency for directive superstrate EBG antenna,” Electron. Lett., vol. 43, no. 13, pp. 702–703, 2007.
[60] C. Mateo-Segura, A. P. Feresidis, and G. Goussetie “Bandwidth enhancement of 2-D leaky-wave antennas with double layer periodic surfaces,” IEEE Trans. Antennas Propag., vol. 62, no. 2, pp. 586–593, 2014.
[61] R. Gardelli, M. Albani, and F. Capolino, “Array thinning by using antennas in a Fabry-Perot cavity for gain enhancement,” IEEE Trans. Antennas Propag., vol. 54, no. 7, pp. 1979–1990, 2006.
[62] R. M. Hashmi, B. A. Zeb and K. P. Esselle, “Wideband high-gain EBG resonator antennas with small footprints and all-dielectric superstructures,” IEEE Trans. Antennas Propag., vol. 62, no. 6, pp. 2970–2977, 2014.
[63] R. M. Hashmi and K. P. Esselle, “A class of extremely wideband resonant cavity antennas with large directivity-bandwidth products,” IEEE Trans. Antennas Propag., vol. 64, no. 2, pp. 830–835, 2016.
[64] M. Akbari, S. Gupta, M. Farahani, A. R. Sebak, and T. Denidni, “Analytic study on CP enhancement of millimetre wave DR and patch subarray antennas,” International Journal of RF and Microwave Computer-Aided Engineering. vol. 27, pp. 2−11, 2017.
[65] H. Attia, M. L. Abdelghani, and T. A. Denidni, “Wideband and high-gain millimetre-wave antenna based on FSS fabry–perot cavity,” IEEE Trans. Antennas Propag., vol. 65, no. 10, pp. 5589–5594, 2017.
[66] M. Akbari, S. Gupta, M. Farahani, A. R. Sebak, and T.A. Denidni,., “Gain enhancement of circularly-polarized dielectric resonator antenna based on FSS superstrate for MMW applications,” ieee trans. antennas propag., vol. 64, no. 12, December 2016.
[67] B. P. Chacko, G. Augustin, and T. A. Denidni, “FPC antennas: C-band point-to-point communication systems,” IEEE Antennas Wireless Propag. Mag., vol. 58, no. 1, pp. 56–64, 2016.
[68] A. Hosseini, F. Capolino, and F. De Flaviis, “Gain enhancement of a v-band antenna using a Fabry–Pérot cavity with a self-sustained all-metal cap with FSS,” IEEE Trans. Antennas Propag., vol. 63, no. 3, pp. 909–921, 2015.
[69] K. Konstantinidis, A. P. Feresidis, and P. S. Hall, “Broadband sub-wavelength profile high-gain antennas based on multi-layer metasurfaces,” IEEE Trans. Antennas Propag., vol. 63, no. 1, pp. 423–427, 2015.
[70] H. Farahani, M. Veysi, M. Kamyab, and A. Tadjalli, “Mutual coupling reduction in patch antenna arrays using a UC-EBG superstrate,” IEEE Antennas Wireless Propag. Lett., vol. 9, pp. 57–59, 2010.
[71] G. Dubost, “Influence of surface wave upon efficiency and mutual coupling between rectangular microstrip antennas,” in Antennas Propag. Soc. Int. Symp. Dig., Dallas, TX, USA, vol. 2, pp. 660–663, 1990.
[72] P. R. Haddad and D. M. Pozar, “Anomalous mutual coupling between microstrip antennas,” IEEE Trans. Antennas Propag., vol. 42, no. 11, pp. 1545–1549, 1994.

[73] M. A. Khayat, J. T. Williams, D. R. Jackson, and S. A. Long, "Mutual coupling between reduced surface-wave microstrip antennas," IEEE Trans. Antennas Propag., vol. 48, no. 10, pp. 1581–1593, 2000.
[74] R. Xia, S. Qu, P. Li, Q. Jiang, and Z. Nie, "An efficient decoupling feeding network for microstrip antenna array," IEEE Antennas and Wireless Propagation Letters., vol. 14, pp. 871 - 874, 2015.
[75] B. C. Pan, et al., "Reduction of the spatially mutual coupling between dual-polarized patch antennas using coupled metamaterial slabs," Nat. Scientific reports, pp. 1–8, 2016.
[76] T. S. Rappaport et al., "Millimeter wave mobile communications for 5G cellular: It will work!" IEEE Access, vol. 1, pp. 335–349, 2013.
[77] J. R. Costa, E. B. Lima, C. R. Medeiros, and C. A. Fernandes, "Evaluation of a new wideband slot array for MIMO performance enhancement in indoor WLANs," IEEE Trans. Antennas Propagation, vol. 59, no. 4, pp. 1200–1206, 2011.
[78] M. J. Al-Hasan, T. A. Denidni, and A. R. Sebak, "Millimetre-wave compact EBG structure for mutual coupling reduction applications," IEEE Trans. Antennas Propag., vol. 63, no. 2, pp. 823-828, 2015.
[79] H. M. Bernety and A. B. Yakovlev, "Reduction of mutual coupling between neighbouring strip dipole antennas using confocal elliptical metasurface cloaks," IEEE Trans. Antennas Propag., vol. 63, no. 4, pp. 1554-1563, 2015.
[80] C. H. Wu, C. L. Chiu, and T. G. Ma, "Very compact fully lumped decoupling network for a coupled two-element array," IEEE Antennas and Wireless Propagation Letters,, vol. 15, pp. 158-161, 2016.
[81] S. C. Chen, Y. S. Wang, and S. J. A Chung, "Decoupling technique for increasing the port isolation between two strongly coupled antennas," IEEE Trans. Antennas Propag., vol. 56, no. 12, pp. 3650-3658, 2008.
[82] R. Gonzalo, P. de Maagt, and M. Sorolla, "Enhanced patch-antenna performance by suppressing surface waves using photonic-bandgap substrates," IEEE Transactions on Microwave Theory and Techniques, vol. 47, no. 11, pp. 2131– 2138, 1999.
[83] I. Ederra, L. Azcona, B. E. J. Alderman, et al., "A 250 GHz subharmonic mixer design using EBG technology," IEEE Trans. Antennas Propag., vol. 55, no. 11, pp. 2974–2982, 2007.
[84] D. Guha, S. Biswas, M. Biswas, J. Y. Siddiqui, and Y. M. M. Antar, "Concentric ring-shaped defected ground structures for microstrip applications," IEEE Antennas and Wireless Propagation Letters,, vol. 5, pp. 402-405, 2006.
[85] F. G. Zhu, J. D. Xu, and Q. Xu, "Reduction of mutual coupling between closely packed antenna elements using defected ground structure," Electron. Lett., vol. 45, no. 12, pp. 601–602, 2009.
[86] S. Zuo, Y. Z. Yin, Z. Y. Zhang, W. J. Wu, and J. J. Xie, "Eigenmode decoupling for MIMO loop-antenna based on 180 coupler," Progress in Electromagnetics Research Letters, vol. 26, pp. 11–20, 2011.
[87] L. Zhao, L. K. Yeung, and K. L. A. Wu, "Coupled resonator decoupling network for two-element compact antenna arrays in mobile terminals," IEEE Antennas and Wireless Propagation Letters,, vol. 62, no. 5, pp. 2767–2776 (2014).
[88] C. Oikonomopoulos-Zachos, "Double layer compact four-port antenna using a symmetrical feeding technique for future MIMO antenna systems at 5.6GHz," 2010 IEEE Antennas and Propagation Society International Symposium, Toronto, ON, pp. 1-4, 2010.

[89] H. Qi, L. Liu, X. Yin, H. Zhao and W. J. Kulesza, "Mutual coupling suppression between two closely spaced microstrip antennas with an asymmetrical coplanar strip wall," IEEE Antennas and Wireless Propagation Letters, vol. 15, pp. 191-194, 2016.
[90] T. Negishi, D. Erricolo, and P. L. E. Uslenghi, "Metamaterial spheroidal cavity to enhance dipole radiation," IEEE Trans. Antennas Propag., vol. 63, no. 6, pp. 2802–2807, 2015.
[91] A. Mehdipour, T. A. Denidni, and A. R. Sebak, "Multi-band miniaturized antenna loaded by ZOR and CSRR metamaterial structures with monopolar radiation pattern," IEEE Trans. Antennas Propag., vol. 62, pp. 555-562, 2014.
[92] E. Saenz, I. Ederra, R. Gonzalo, S. Pivnenko, O. Breinbjerg, and P. de Maagt, "Coupling reduction between dipole antenna elements by using a planar meta-surface," IEEE Trans. Antennas Propag., vol. 57, no. 2, pp. 383–394, 2009.
[93] E. Saenz, K. Guven, E. Ozbay, I. Ederra, and R. Gonzalo, "Decoupling of multi frequency dipole antenna arrays for microwave imaging applications," Int. J. Antennas Propag., vol. 2010, p. 8, 2010.
[94] M. Ghaderi and N. C. Karmakar, "Frequency selective surface for reducing mutual coupling in antenna arrays," Microwave Conference Proceedings (APMC), 2011 Asia-Pacific, Melbourne, VIC, pp. 1877-1880, 2011.
[95] D. Singh, A. Kumar, S. Meena, and V. Agrawal, "Analysis of frequency selective surfaces for radar absorbing materials," Progress In Electromagnetics Research B, vol. 38, 297-314, 2012.
[96] L. Hermann, "MIMO OFDM space time coding – spatial multiplexing, increasing performance and spectral efficiency in wireless systems," Part I Technical Basis, technical report, Institute fürRundfunktechnik, 2007.
[97] R. Lech, M. Mazur, and J. Mazur, "Analysis and design of a polarizer rotator system," IEEE Trans. Antennas Propag., vol. 56, no. 3, pp. 844-847, 2008.
[98] Z. Li, R. Zhao, T. Koschny, M. Kafesaki, K.B. Alici, E. Colak, H. Caglayan, E. Ozbay, C. M. Soukoulis, "Chiral metamaterials with negative refractive index based on four "U" split ring resonators," Applied Physical Letters, vol. 97, 081901, 2010.
[99] A. Dadgarpour, B. Zarghooni, B. S. Virdee, T. A. Denidni, A. A. Kishk, "Mutual Coupling Reduction in Dielectric Resonator Antennas Using metasurface shield for 60 GHz MIMO systems," IEEE Antennas Wireless Propag. Lett., vol. 16, pp. 477-480, 2016.
[100] R. Karimian, A. Kesavan, M. Nedil, T. A. Denidni, "Low Mutual Coupling 60-GHz MIMO Antenna System with Frequency Selective Surface Wall," IEEE Antennas Wireless Propag. Lett., vol. 16, pp. 373-376, 2017.
[101] M. Akbari, et al. "Spatially Decoupling of CP Antennas Based on FSS for 30-GHz MIMO Systems." IEEE Access, vol. 5, pp. 6527-6537, 2017.
[102] L. Li, Y. Li, Z. Wu, F. Huo, Y. Zhang, C. Zhao, "Novel Polarization-Reconfigurable Converter Based on Multilayer Frequency-Selective Surfaces," Proceedings of the IEEE, vol. 103, no. 7, pp. 1057-1070, 2015.
[103] S. M. A. M. H. Abadi and Nader Behdad, "Wideband Linear-to-Circular Polarization Converters Based on Miniaturized-Element Frequency Selective Surfaces," IEEE Trans. Veh. Technol., vol. 64, no. 2, pp. 525–534, 2016.
[104] R. Orr, G. Goussetis, and V. Fusco, "Design method for circularly polarized Fabry-Perot cavity antennas," IEEE Trans. Antennas Propag., vol. 62, no. 1, pp. 19–26, 2014.
[105] L. Martinez-Lopez, J. Rodriguez-Cuevas, J. I. Martinez-Lopez, and A. E. Martynyuk, "A multilayer circular polarizer based on bisected split ring frequency selective surfaces," IEEE Antennas Wireless Propag. Lett. vol. 13, pp. 153–156, 2014.

[106] M. Joyal and J. Laurin, ‘‘Analysis and design of thin circular polarizers based on meander lines,’’ IEEE Trans. Antennas Propag., vol. 60, no. 6, pp. 3007–3011, 2012.
[107] Fei, Peng, et al. “A single-layer circular polarizer based on hybrid meander line and loop configuration,’’ IEEE Trans. Antennas Propag., vol. 63, no. 10, pp. 4609-4614, 2015.
[108] J. M. I. Alonso, G. A. Calderón, and M. S. Pérez, “SIW Antenna with Polarizer at ku-Band,” IEEE Trans. Antennas Propag., vol. 63, no: 6, pp. 2782–2786, 2015.
[109] X. C. Zhu et al., ‘‘Design of a bandwidth-enhanced polarization rotating frequency selective surface,’’ IEEE Trans. Antennas Propag., vol. 62, no. 2, pp. 940–944, 2014.
[110] H. L. Zhu, S. W. Cheung, K. L. Chung, and T. I. Yuk, “Linear to-circular polarization conversion using metasurface,” IEEE Trans. Antennas Propag., vol. 61, no. 9, pp. 4615–4623, 2013.
[111] Cheng, Y., C. Wu, Z. Z. Cheng, and R. Z. Gong, “Ultra-compact multi-band chiral metamaterial circular polarizer based on triple twisted split-ring resonator,” Progress In Electromagnetics Research, vol. 155, pp. 105-113, 2016.
[112] M. Mutlu, A.E. Akosman, E. Ozbay, “Broadband circular polarizer based on high-contrast gratings,” Opt. Lett., vol. 37, no. 11, pp. 2094-2096, 2012.
[113] Jackson, J. D., Classical Electrodynamics, 3rd Edition, 205–207, Wiley, 1999.
[114] C. A. Balanis, Antenna Theory Analysis and Design, Second Edition, Wiley, 1997.
[115] Li, Bo, and Z. Shen, “Three-dimensional bandpass frequency-selective structures with multiple transmission zeros,’’ IEEE Trans. Microw. Theory Techn., vol. 61, no. 10, pp. 3578-3589, 2013.
[116] A. K. Rashid, B. Li, and Z. Shen. “An overview of three-dimensional frequency-selective structures.” IEEE Antennas and Propagation Magazine. vol. 56, no. 3, pp. 43-67, 2014.
[117] J. D. Shumpert, “Modelling of Periodic Dielectric Structures (electromagnetic Crystals),” Diss. University of Michigan, 2001.
[118] R. E. Collin, Foundations for Microwave Engineering, McGraw–Hill, Inc., New York, NY, 1992.
[119] Z. Li, W. Liu, H. Cheng, S. Chen, and J. Tian, “Realizing Broadband and Invertible Linear-to-circular Polarization Converter with Ultrathin Single layer Metasurface”, Sci. rep., vol. 5, pp. 1-9, 2015.
[120] M. Euler, V. Fusco, R. Dickie, R. Cahill, and J. Verheggen, “Sub-mm wet etched linear to circular polarization FSS based polarization converters,” IEEE Trans. Antennas Propag., vol. 59, no. 8, pp. 3103–3106, 2011.
[121] S.-C. Gao, L-W Li, M.-S. Leong, and T.-S. Yeo, “Wide-band microstrip antenna with an H-shaped coupling aperture,” IEEE Trans. Veh. Technol., vol. 51, no. 1, pp. 17–27, 2002.
[122] R. Bayderkhani and H. Reza Hassani, “Wideband and low sidelobe slot antenna fed by series-fed printed array,” IEEE Trans. Antennas Propag., vol. 58, no. 12, pp. 3898–3904, 2010.
[123] M. Farahani, et al. “Mutual Coupling Reduction in Millimeter-Wave MIMO Antenna Array Using a Metamaterial Polarization-Rotator Wall.” IEEE Antennas Wireless Propag. Lett. vol. 16, pp. 2324–2327, 2017.
[124] S. Vakilinia, B. Heidarpour, M. Cheriet, “Energy Efficient Resource Allocation in Cloud Computing environments,” IEEE Access, vol. 4, pp. 8544 - 8557, 2016.
[125] S. Yan and G. A. E. Vandenbosch, “Compact circular polarizer based on chiral twisted double split-ring resonator,” Appl. Phys. Lett., vol. 102, no. 10, p. 103503, 2013.
[126] T. Hussain et al., “Miniaturization of Frequency Selective Surfaces Using 2.5-D Knitted Structures: Design and Synthesis,” IEEE Trans. Antennas Propag. vol. 65, no. 5, 2017.

[127] B. A. Munk, "Frequency Selective Surfaces: Theory and Design," Hoboken, NJ, USA: Wiley, 2005.
[128] F. Bayatpur and K. Sarabandi, "Single-layer high-order miniaturized element frequency-selective surfaces," IEEE Trans. Microw. Theory Techn., vol. 56, no. 4, pp. 774–781, 2008.
[129] I. S. Syed, Y. Ranga, L. Matekovits, K. P. Esselle, and S. G. Hay, "A single-layer frequency-selective surface for ultrawideband electromagnetic shielding," IEEE Trans. Electromagn. Compat., vol. 56, no. 6, pp. 1404–1411, 2014.
[130] M. Akbari, H. A. Ghalyon, M. Farahani, A. R. Sebak, and T.A. Denidni., "Spatially Decoupling of CP Antennas Based on FSS for 30GHz MIMO Systems," IEEE Access., vol. 5, pp. 6527–6537, April. 2017.
[131] M. Akbari, M. Farahani, A. R. Sebak, and T.A. Denidni., "Ka-Band Linear to Circular Polarization Converter Based on Multilayer Slab with Broadband Performance," IEEE Access., vol. 5, pp. 17927–17937, 2017.
[132] J. Lee, M. Yoo, and S. Lim, "A study of ultra-thin single layer frequency selective surface microwave absorbers with three different bandwidths using double resonance," IEEE Trans. Antennas Propag., vol. 63, no. 1, pp. 221–230, 2015.
[133] S. Genovesi, F. Costa, and A. Monorchio, "Low-profile array with reduced radar cross section by using hybrid frequency selective surfaces," IEEE Trans. Antennas Propag., vol. 60, no. 5, pp. 2327–2335, 2012.
[134] W. Chen, C. A. Balanis, and C. R. Birtcher, "Checkerboard EBG Surfaces for Wideband Radar Cross Section Reduction," IEEE Trans. Antennas Propag., vol. 63, no. 6, pp. 2636–2645, 2015.
[135] J. C. I. Galarregui, A. T. Pereda, J. L. Falcón, I. Ederra, R. Gonzalo, and P. Maagt, "Broadband Radar Cross-Section Reduction Using AMC Technology," IEEE Trans. Antennas Propag., vol. 61, no. 12, pp. 6136–6143, 2013.
[136] W. W. Salisbury, "Absorbent body for electromagnetic waves," U.S. Patent 2599944, 1952.
[137] A. Edalati and K. Sarabandi, "Wideband, Wide Angle, Polarization Independent RCS Reduction Using Nonabsorptive Miniaturized-Element Frequency Selective Surfaces," IEEE Trans. Antennas Propag., vol. 62, no. 2, pp. 747–754, 2014.
[138] E. F. Knott, M. T. Tuley, and J. F. Shaeffer, Radar Cross Section, 2nd ed. Norwood, MA, USA: Artech House, 1993.
[139] M. Paquay, J. C. Iriarte, I. Ederra, R. Gonzalo, and P. de Maagt, "Thin AMC structure for radar cross-section reduction," IEEE Trans. Antennas Propag., vol. 55, no. 12, 2007.
[140] Y. Zhang, R. Mittra, B. Z. Wang, and N.-T. Huang, "AMCs for ultra-thin and broadband RAM design," Electron. Lett., vol. 45, no. 10, pp. 484–485, 2009.
[141] A. Y. Modi, C. A. Balanis, C. R. Birtcher, and H. Shaman, "Novel Design of Ultra-Broadband Radar Cross Section Reduction Surfaces using Artificial Magnetic Conductors," IEEE Trans. on Antennas and Propag., vol. 65, no. 10, pp. 5406–5417, 2017.
[142] [142] Liu, Y., K. Li, Y.-T. Jia, Y.-W. Hao, S. X. Gong, and Y. J. Guo, "Wideband RCS reduction of a slot array antenna using polarization conversion metasurface," IEEE Trans. on Antennas and Propag., vol. 64, no. 1, pp. 326–331, 2016.
[143] Y. T. Jia, Y. Liu, Y. J. Guo, K. Li, and S. X. Gong, "Broadband polarization rotation reflective surfaces and their applications to RCS reduction," IEEE Trans. on Antennas and Propag., vol. 64, no. 1, pp. 179–188, 2016.
[144] M. D. Feng, J. F. Wang, H. Ma, W. D. Mo, H. J. Ye, and S. B. Qu, "Broadband polarization rotator based on multi-order plasmon resonances and high impedance surfaces," J. Appl. Phys. vol. 114, 074508, 2013.
[145] Y. Nanfang, et al. "Light propagation with phase discontinuities: generalized laws of reflection and refraction." Science, 334.6054, pp. 333-337, 2011.

[146] C. Hongya, et al. “Ultra-wideband polarization conversion metasurfaces based on multiple Plasmon resonances.” Journal of Applied Physics 115.15 (2014): 154504.
[147] L. Bao-Qin, et al. “Ultra-Wideband and High-Efficiency Cross Polarization Converter Based on Anisotropic Metasurface.” Microwave and Optical Technology Letters 58.10, 2402-2405, 2016.
[148] A. Ghayekhloo, M. Afsahi, and A. A. Orouji., “Checkerboard plasma electromagnetic surface for wideband and wide-angle bistatic radar cross section reduction,” IEEE Trans. on Plasma Science, vol. 45, no. 4, pp. 179–188, 2017.
[149] S. H. Esmaeli and S. H. Sedighy, “Wideband radar cross-section reduction by AMC,” Electron. Lett., vol. 52, no. 1, pp. 70–71, 2015.
[150] K. C. Hwang, “A novel meander-grooved polarization twist reflector,” IEEE Microw. Wireless Compon. Lett., vol. 20, no. 4, pp. 217–219, 2010.
[151] H. Chen et al., “Ultra-wideband polarization conversion metasurfaces,”in Proc. IEEE APCAP, pp. 1009–1011, 2014.
[152] X. Gao, et al., “Ultra-wideband and high-efficiency linear polarization converter based on double v-shaped metasurface,” IEEE Trans. Antennas Propag., vol. 63, no. 8, pp. 3522–3530, 2015.
[153] J. Zhao and Y. Cheng, “A high-efficiency and broadband reflective 90° linear polarization rotator based on anisotropic metamaterial,” Appl. Phys. B, vol. 122, p. 255, 2016.
[154] X. X. Zheng, Z. Y. Xiao, and X. Y. Ling, “Broadband and efficient reflective polarization converter based on a three-dimensional metamaterial,” Opt. Quantum Electron., vol. 48, p. 461, 2016.
[155] B. Q. Lin, X. Y. Da, J. L. Wu, W. Li, Y. W. Fang, and Z. H. Zhu, “Ultra-wideband and high-efficiency cross polarization converter based on anisotropic metasurface,” Miceow. Opt. Tech. Lett., vol. 58, no. 10, pp. 2402–2405, 2016.
[156] Y. Jia, Y. Liu, Y. J. Guo, K. Li, and S. Gong, “A dual-patch polarization rotation reflective surface and its application to ultra-wideband RCS reduction,” IEEE Trans. Antennas Propag., vol. 65, no. 6, pp. 3291–3295, 2017.
[157] S. J. Li, X. Y. Cao, J. Gao, T. Liu, Y. J. Zheng, and Z. Zhang, “Analysis and design of three-layer perfect metamaterial-inspired absorber based on double split-serration-rings structure,” IEEE Trans. Antennas Propag., vol. 63, no. 11, pp. 5155–5160, 2015.
[158] W. Pan, C. Huang, P. Chen, X. Ma, C. Hu, and X. Luo, “A low-RCS and high-gain partially reflecting surface antenna,” IEEE Trans. Antennas Propag., vol. 62, no. 2, pp. 945–949, 2014.
[159] Y.-J. Zheng, J. Gao, X.-Y. Cao, S.-J. Li, and W.-Q. Li, “Wideband RCS reduction and gain enhancement microstrip antenna using chessboard configuration superstrate,” Microw. Opt. Technol. Lett., vol. 57, no. 7, pp. 1738–1741, 2015.
[160] Y. J. Zheng, J. Gao, X. Y. Cao, Z. D. Yuan and H. H. Yang, “Wideband RCS reduction of a microstrip antenna using artificial magnetic conductor structures,” IEEE Antennas Wireless Propag. Lett., vol. 14, pp. 1582−1585, 2015.
[161] Y. Zhao, X. Y. Cao, J. Gao, X. Yao, T. Liu, W. Q. Li and S. J. Li, “Broadband low-RCS metasurface and its application on antenna,” IEEE Trans. Antennas Propag., vol. 64, no. 7, pp. 2954−2962, 2016.
[162] W. Q. Li, X. Y. Cao, J. Gao, Z. Zhang, L. L. Cong, “Broadband RCS reduction and gain enhancement microstrip antenna using shared aperture artificial composite material based

on quasi-fractal tree," IET Microwaves, Antennas Propag., vol. 10, no. 4, pp. 370−377, 2016.
[163] Y. Zheng, J. Gao, Y. Zhou, et al., "Wideband gain enhancement and RCS reduction of Fabry-Perot resonator antenna with chessboard arranged metamaterial superstrate," IEEE Trans. Antennas Propag., ., vol. 66, no. 2, pp. 590−599, 2018.
[164] S. He, Q. H. Wu, and J. Saunders, "Group search optimizer: an optimization algorithm inspired by animal searching behavior," IEEE Trans. Evol. Comput., vol. 13, no. 5, pp. 973-990, 2009.
[165] D. Mustard, "Numerical integration over the n-dimensional spherical shell," Math. Comput., vol. 18, no. 88, pp. 578-589, 1964.

Appendix. Bi-Level Group Search Optimization (GSO) Algorithm

In this section, initially, a short overview on basics of group search optimization algorithm is given. Then, the proposed bi-level-GSO algorithm is discussed in detail. The proposed bi-level GSO algorithm is efficient for handling minimax mixed-integer problems which contain continuous and binary.

A. Basics of GSO

The principal idea of the GSO is inspired by animal group-living theory. The searching behaviour of animals combined with the producer-scrounger (PS) model, which uses either "producing" as the finding process or "scrounging" as the joining strategy, are the prime bases of GSO. The GSO is a population-based heuristic algorithm and the population is called the group [164]. In this theory, the group members are categorized as follows:

- Producer: A member which possesses the best position in comparison to other members and equipped to vision ability.
- Scroungers: Scroungers are joiners which follows the producer member.
- Rangers: Random walkers.
-

The producer scans the vicinity of its existing position to obtain better states. The scanning ability is named vision ability and mentions to a process of testing some particular point in the vicinity of the producer member. Scroungers define their searching path in terms of the producer member. Ultimately, scrounger members try to be in the closest location relative to the producer member. In addition, in order to avoid getting stuck in local minima, rangers are committed as random walkers to carry out the random search. The continuous and binary searching spaces have various properties. Hence, the mathematical formulation for modelling the behaviour of GSO group members must be different in each space. In the following sections, the appropriate mathematical formulation for modelling GSO group members in each searching space, are given.

B. Continuous search space

Basically, GSO has been presented in [164] as a continuous searching tool. It continues searching space, each member of GSO group is identified utilizing two vectors, i.e. position vectors and head angle vectors. The position and head angle of ith member at the kth iteration are $X_i^k \in R^n$ and $\varphi_i^k = (\varphi_{i1}^k, ..., \varphi_{i(n-1)}^k) \in R^{n-1}$, respectively. Where, R is a series of real numbers and n is the dimension of search space. Moreover, φ_{in} is the polar angle of ith member relative to the nth dimension. As before mentioned, the producer member should use its vision ability to obtain better solutions. Vision ability is defined as the ability of testing some points in the vicinity of producer location [165]. In GSO, three points should be selected [164]. These points are labelled zero, right and left. At kth iteration, for the producer member which is located in X_p^k, zero, right and left points could be defined using equations (A-1) to (A-3), respectively.

$$X_z = X_p^k + r_1 l_{\max} D_p^k(\varphi^k) \tag{A-1}$$

$$X_r = X_p^k + r_1 l_{\max} D_p^k(\varphi^k + r_2 \theta_{\max} / 2) \tag{A-2}$$

$$X_l = X_p^k + r_1 l_{\max} D_p^k(\varphi^k - r_2 \theta_{\max} / 2) \tag{A-3}$$

$D_i^k(\varphi_i^k)$ is the search direction vector of ith member at the kth iteration. Each member of the search direction vector, d_{ij}^k, could be computed as below [A-6]:

$$d_{ij}^k = \begin{cases} \prod_{q=1}^{n-1} \cos(\varphi_{iq}^k) & j = 1 \\ \sin(\varphi_{i(j-1)}^k) \prod_{q=j}^{n-1} \cos(\varphi_{iq}^k) & j = 2, ..., n-1 \\ \sin(\varphi_{i(n-1)}^k) & j = n \end{cases} \tag{A-4}$$

The group members who are assigned as scroungers will keep searching for opportunities by tracking the producer member. At the kth iteration, the ith scrounger members are modelled as

random trackers of the producer. Scroungers compare their position with the position of producer and try a random path to reach it. Therefore, the mathematical model of their behaviour is as follows:

$$X_i^{k+1} = X_i^k + r_3 \circ \quad) \tag{A-5}$$

As the third type of GSO members, rangers play an outstanding role in GSO searching and finding the procedure. Rangers could be modelled as random position and head angle vector. During k^{th} iteration, the random length is defined utilizing (A-6):

$$l_i = a\ r_1\ l_{\max} \tag{A-6}$$

Then, in order to calculate the random position vector, the random length is inserted to equation (A-7):

$$X_i^{k+1} = X_i^k + l_i D_i^k\ (\varphi^{k+1}) \tag{A-7}$$

C. Binary search space

The binary GSO (BGSO) is proposed to investigate the performance of GSO in binary searching space. In the following different sections of BGSO is discussed.

C-1. Producer

In binary searching space, all the members of GSO group are either 0 or 1. According to (A-1) to (A-3), the zero, right and left points are defined using the term $r_1 l_{\max}$ as a random length. Therefore, in order to simulate the producer searching ability, a random part of producer member

array should be chosen. In Figure A-1 (a), the random length selection for the producer member is illustrated. According to Figure A-1(a), for $(1\times n)$ array, r_3 is a random pointer in the range of (1, n) and r_4 is also a random pointer in the range (r_3, n). After simulating the random length, similar to (A-1) to (A-3), zero, right and left points should be discriminated. For the selected sub array, each two sequential columns could be defined as one step of head angle revising steps. Since there are 2 binary variables in each step, four states are possible. Therefore, equations (A-1) to (A-3) are simulated by generating three new arrays. Once the arrays are evaluated, if the new one has better fitness value in comparison with that of the older producer, the new array is chosen as a producer member. On the other hand, if a better solution is not achieved, the producer should change its head angle and performs producing. The scanning process for a sample sub-array along with producing action at the second step of head angle is depicted in Figure A-1(b) and Figure A-1(c), respectively.

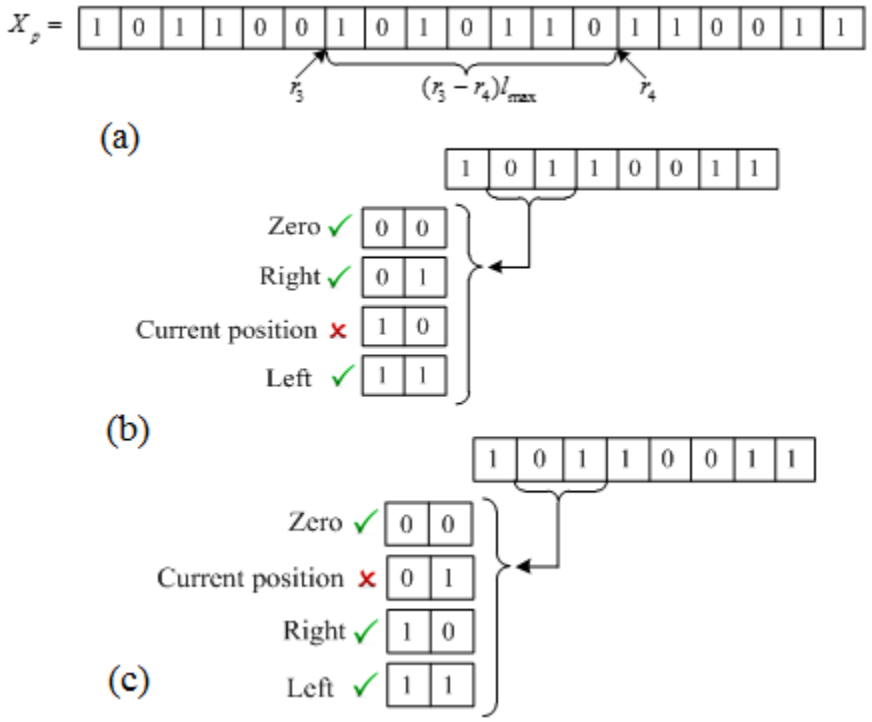

Figure A-1: (a) Random length selection for the producer member, (b) Defining zero, right and left points, and (c) Producing procedure at the second step of head angle

C-2. Scrounger

As mentioned in this Section, scroungers try to follow the producer member. According to (A-5), a random length should be multiplied to term $X_p^k - X_i^k$. As previously mentioned, in binary space, random length selection is performed using two random pointers. The term $X_p^k - X_i^k$ could be simulated as:

$$X_p^k - X_i^k = XOR(X_p^k, X_i^k) \tag{A-8}$$

Where, X_p^k is producer member position at k[th] iteration and X_i^k is i[th] scrounger member at k[th] iteration. After computing the term $X_p^k - X_i^k$, a random length using pointers r_5 and r_6 should be selected. Figure A-2 depicts the simulation of term $r \circ$ $^{k}_{i}$).

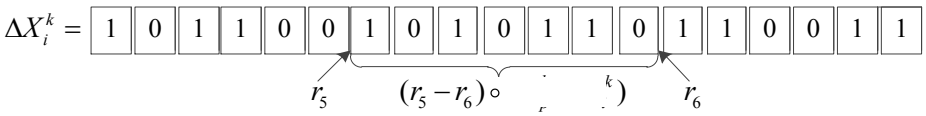

Figure A-2: Scrounging process

Components of the sub-array which are equal to 1, represent the difference. Hence, the state of their relevant components in the X_i^k should be varied. Finally, a new scrounger member is produced and equation (A-8) is simulated.

C-3. Ranger

With respect to (A-5), ranging process is performed using a random length and head angle. Similar to the producer and scroungers, random length is accomplished by using two random pointers, (r_7 and r_8). In this process, the random direction could be generated using (A-9):

$$\Delta X_i = rand\,\mathrm{int}(1, l) \tag{A-9}$$

Where, ΔX_i is the selected sub-array using r_7 and r_8. $rand\,\mathrm{int}(1, x)$ is an operator which generates a random binary array with length of x, and l is a randomly generated length.

D. Outline of the proposed model

The general framework of the proposed methodology is exhibited in Figure A-3. Referring to Figure A-1, the problem is decomposed into a binary (master) level and continuous (slave) level. The object associated with binary space is to minimize maximum of array factor (A-10). Meanwhile, continuous space operates optimization to reach the maximum of array factor (A-10), considering

$0^{\circ} < \theta < 180^{\circ}$ and $-180^{\circ} < \varphi < 180^{\circ}$. Moreover, technical constraints are embedded in binary space as follows:

$$f(\theta,\varphi) = \sum_{m=1}^{M} e^{j(m-1)(kD\sin\theta\cos\varphi)} \times \sum_{m=1}^{M} e^{j(m-1)(kD\sin\theta\sin\varphi)} \times e^{jn\pi} \quad \text{(A-10)}$$

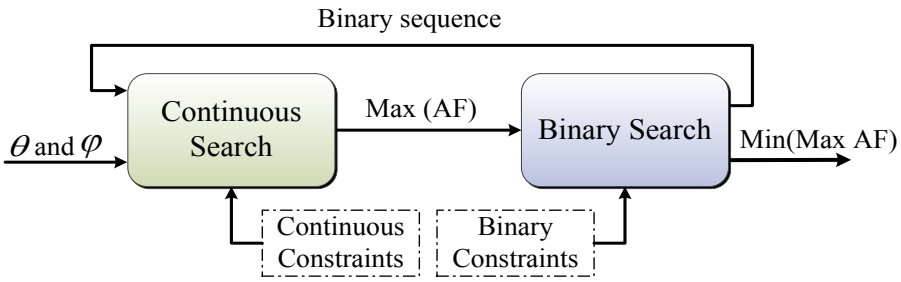

Figure A-3: Defined bi-level model of algorithm

D-1. Binary search space

Here, some preliminary assumptions are made to restrict the search space and in turn, steer the optimization process toward the optimal solution. To do so, the following patterns should be avoided:

1) A metasurface with all lattices equal to either zero or one;
2) The coding sequences of 010101…/010101…; and,
3) The coding sequence of 010101…/ 101010…..

The key reason for discarding these sequences is that by inserting them in (A-10) and using geometric series concept, equations (A-11), (A-12), and (A-13) are yielded, respectively. Here, the coefficients C_1, C_2, C_3 are constant values. The radiation patterns associated with (A-11) to (A-13) possess one, two, and four main beams, respectively. Such a number of scattered main beams are too small to provide impressive RCS reduction. In order to implement the mentioned constraints to the optimization algorithm, two 1×N index vectors are defined as x_0 and x_1 (see Figure A-4). Based on the initial digit of each column or row, the proper index matrix should be chosen. Then, the constraint handling process should be performed as depicted in Figure A-5. If the outcome of constraint handling process, i.e. x_{output}, is zero, the constraint is violated and new random data should be generated.

$$|f_1(\theta,\varphi)| = C_1 |\cos\psi_1 + \cos\psi_2| = 2C_1 \left|\cos\frac{\psi_1+\psi_2}{2}\cos\frac{\psi_1-\psi_2}{2}\right|, \tag{A-11}$$

$$|f_2(\theta,\varphi)| = C_2 |\sin\psi_1 + \sin\psi_2| = 2C_2 \left|\sin\frac{\psi_1+\psi_2}{2}\cos\frac{\psi_1-\psi_2}{2}\right|, \tag{A-12}$$

$$|f_3(\theta,\varphi)| = C_3 |\cos\psi_1 - \cos\psi_2| = 2C_3 \left|\sin\frac{\psi_1+\psi_2}{2}\sin\frac{\psi_1-\psi_2}{2}\right|, \tag{A-13}$$

$$\psi_1 = \frac{1}{2}kD\left(\sin\theta\cos\varphi + \sin\theta\sin\varphi\right), \quad \psi_2 = \frac{1}{2}kD\left(-\sin\theta\cos\varphi + \sin\theta\sin\varphi\right) \tag{A-14}$$

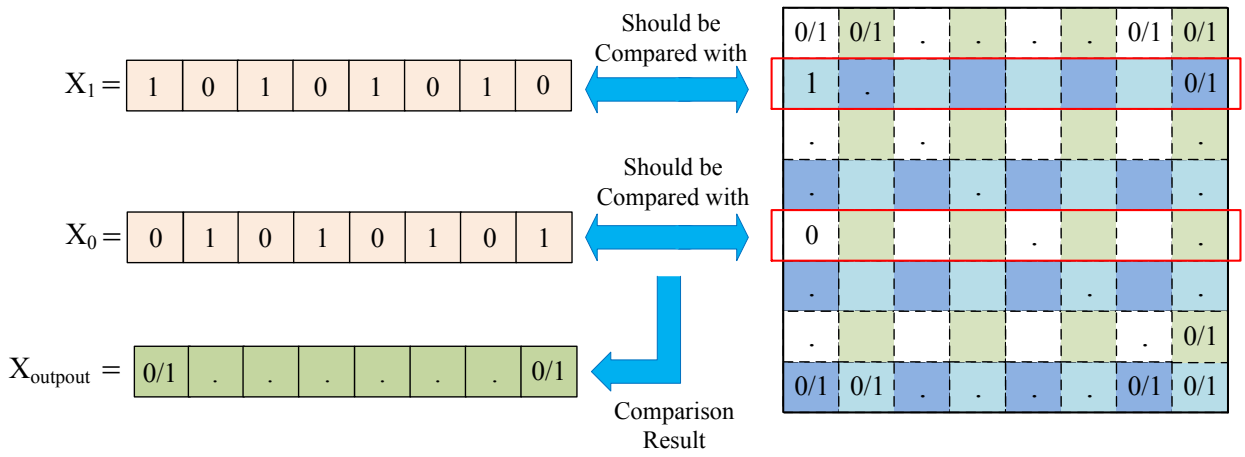

Figure A-4: (a) 1×8, x_0 and x_1 vectors, (b) 8×8, random matrix, and (c) 1×8, x_{output}.

Considering aforementioned constraints and minima x feature of our problem, bi-level GSO is devised. Figure A-6 shows the flowchart of this algorithm in details. It can be obviously clarified that the binary space optimizes its objective by anticipating the optimal response of the continuous part.

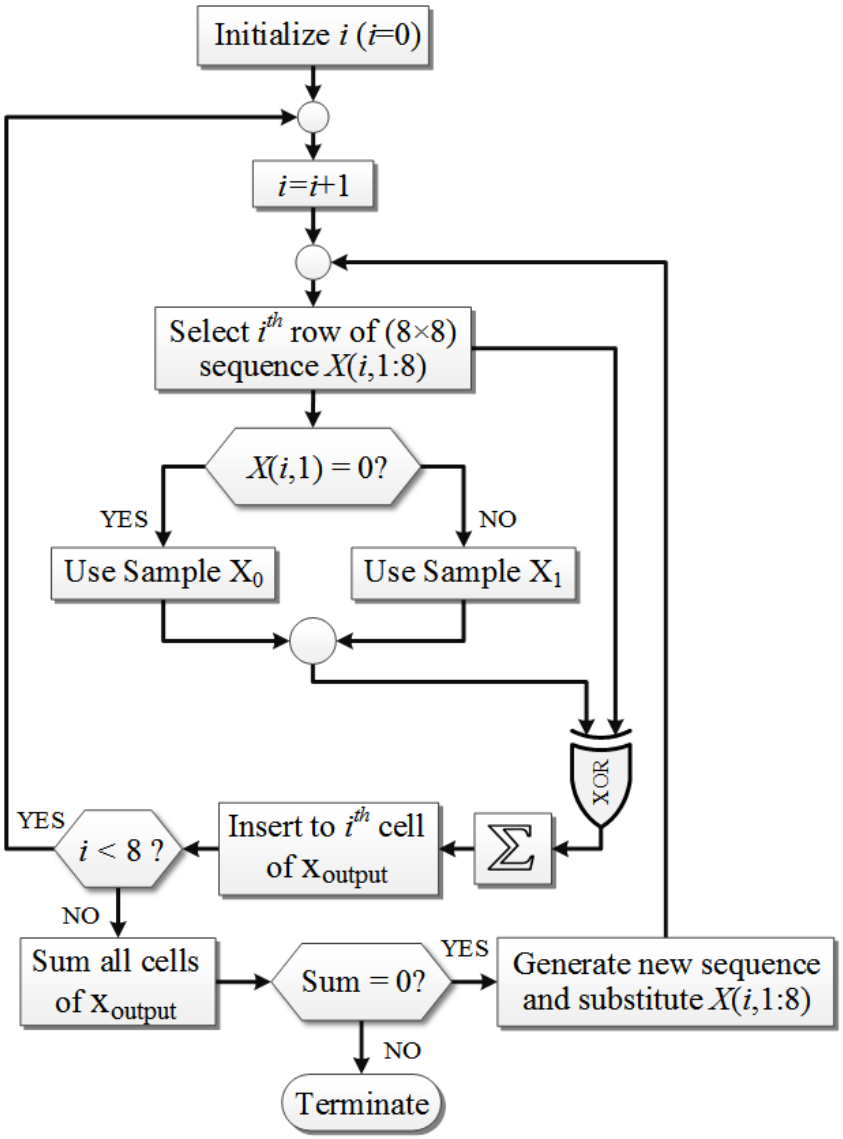

Fig. 5. Constraint handling process in binary space.

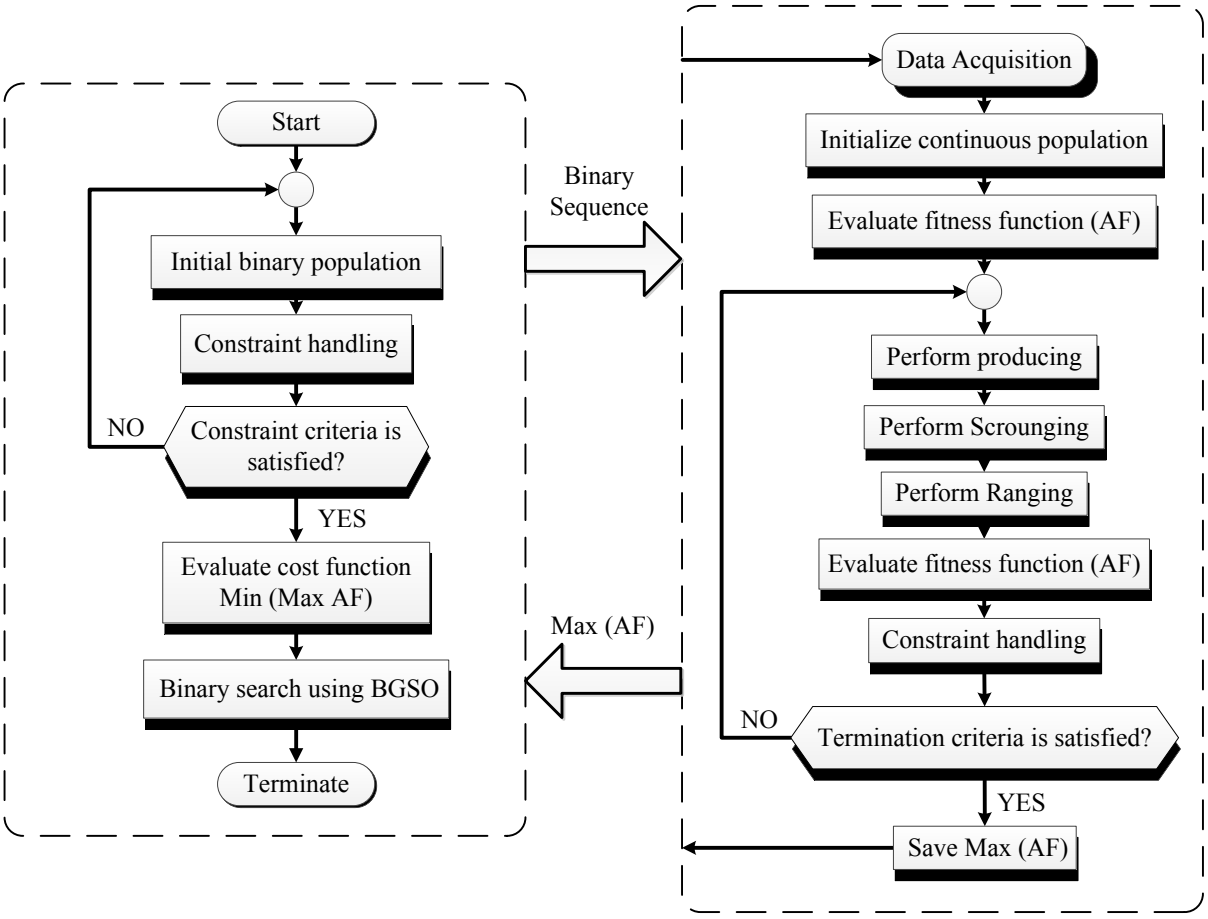

Figure A-6: Flowchart of bi-level GSO algorithm.